



MONASH University

Forward and Inverse Modeling of Geological Folds

Lachlan James Grose
BSc (Honours) Monash University

A thesis submitted for the degree of *Doctor of Philosophy* at
Monash University in 2017
School of Earth, Atmosphere and Environment

Copyright notice

©Lachlan Grose 2017

I certify that I have made all reasonable efforts to secure copyright permissions for third-party content included in this thesis and have not knowingly added copyright content to my work without the owner's permission.

Abstract

One of the challenges for geological research and minerals exploration is to predict and represent geology at depth and in 3D. The geometry of folded surfaces are difficult to characterise because they are defined by localised patterns of curvature. This conflicts with how surfaces are created for 3D modeling, where a surface of minimal curvature is fitted to observations. To address this problem more structural geology needs to be incorporated into the description of folded surfaces for 3D modeling.

The process of building 3D models can be considered as an inverse problem where the aim is to predict the parameters for a forward model representing geological observations. An appropriate forward model will give a single unique solution for a set of parameter values. The solution to the inverse problem is non unique and as there are an infinite number of parameter combinations that can give the same observations throughout the model.

This study first defines a forward model for modeling folds allowing for multiple fold events to be characterised. The overprinting relationships between observed foliations associated with folding are used to determine the relative timing of the folds. Each folding event is modeled backwards in time starting with the most recent. For each folding event starting with the most recent a fold frame is built to capture the geometry of the structural elements of the fold: the fold axis, axial surface, and structural vergence. The geometry of the folds are extracted from geological observations in two parts one describes the geometry of the fold axis in the axial surface. Another Fourier describes the fold shape looking down plunge. A sample semi-variogram of the fold axis and fold shape using the fold frame coordinates is used to automatically identify the wavelength of the folding. The fold geometry can then be represented by finding the best fit Fourier series to represent the fold axis and another represents the folds shape looking down plunge within the fold frame.

The forward model forms the basis of the geological inversion scheme. The geological observations are used within a Bayesian framework to falsify the possible fold geometries that are built from prior knowledge of the parameter values. Both the fold axis and fold shape are inverted simultaneously and the misfit between the model and data can be incorporated using an uninformative prior distribution. We demonstrate that this approach can be used to target locations where additional structural data can reduce model uncertainty. The inversion was performed using Bayesian inference and could be easily extended to incorporate various types of geological observation including geological knowledge into the inversion. Incorporating geological knowledge directly into the inversion scheme rather than using the geologist's interpretation is preferable because the interpretation is subjective and usually not unique.

The forward and inverse geological modeling is demonstrated on synthetic and natural examples typical of folded terranes: doubly plunging, interference patterns and parasitic folding. The combined inversion of geological data and knowledge could be used by geologists while mapping to propagate information about uncertainties throughout the mapping/model building process allowing for different structural interpretations to be rapidly tested for targeted data collection. This inversion scheme not only provides a more rigorous way of sampling the geologically possible models but will also allow for a true joint geological and geophysical inversion.

Declaration

This thesis contains no material which has been accepted for the award of any other degree or diploma at any university or equivalent institution and that, to the best of my knowledge and belief, this thesis contains no material previously published or written by another person, except where due reference is made in the text of the thesis.

Signature:



Print Name: Lachlan James Grose

Date: 5-12-2017

Publications during enrolment

- **Implicit modeling of folds and overprinting deformation**

Dec 2016 *Earth and Planetary Science*

Gautier Laurent, Laurent Ailleres, Lachlan Grose, Guillaume Caumon, Mark Jessell and Robin Armit

- **Spatial analysis of an intra-plate basaltic volcanic field in a compressional tectonic setting: South-eastern Australia**

Feb 2017 *Journal of Volcanology and Geothermal Research*

Jackson Cornelius van den Hove, Lachlan Grose, Peter G. Betts, Laurent Ailleres, Jozua Van Otterloo and Ray A.F Cas

- **Structural data constraints for implicit modeling of folds**

Nov 2017 *Journal of Structural Geology*

Lachlan Grose, Gautier Laurent, Laurent Ailleres, Robin Armit, Mark Jessell and Guillaume Caumon

- **Rapid, semi-automatic fracture and contact mapping for point clouds, images and geophysical data**

Aug 2017 *Solid Earth Discussions*

Samuel Thiele, Lachlan Grose, Anindita Samsu, Steven Micklethwaite, Stefan A. Vollgger and Alexander. R. Cruden

Thesis including published works declaration

I hereby declare that this thesis contains no material which has been accepted for the award of any other degree or diploma at any university or equivalent institution and that, to the best of my knowledge and belief, this thesis contains no material previously published or written by another person, except where due reference is made in the text of the thesis.

This thesis includes 2 original papers published in peer reviewed journals, 1 submitted publication and 1 unsubmitted manuscript. The core theme of the thesis is structural geological modeling. The ideas, development and writing up of chapters 3, 4 and 5 in the thesis were the principal responsibility of myself, the student, working within the *School of Earth, Atmosphere and Environment* under the supervision of Dr. Laurent Ailleres, Dr. Gautier Laurent and Prof. Peter Betts.

The inclusion of co-authors reflects the fact that the work came from active collaboration between researchers and acknowledges input into team-based research.

In the case of chapters 2, 3, 4 and 5 my contribution to the work involved the following:

Thesis Chapter	Publication Title	Status	Nature and % of student contribution	Co-author names	Monash student
2	Implicit modeling of folds and overprinting deformation	Published	15% Developed concepts for fold axis, some development of software, input into manuscript	GL 60%	No
				LA 15%	No
				GC 5%	No
				MJ 2.5%	No
				RA 2.5%	No
3	Structural data constraints for implicit modeling of folds	Published	85% Concept, development of software, manuscript writing	GL 5%	No
				LA 4%	No
				RA 2%	No
				MJ 2%	No
				GC 2%	No
4	Inversion of structural geology data for fold geometry	Accepted	90% Concept, development of software, manuscript writing	GL 3%	No
				LA 2%	No
				RA 2%	No
				MJ 2%	No
				TCD 1%	No
5	Inversion of geological data and knowledge	Not Submitted	90% Concept, development of software, manuscript writing	LA 5%	No
				GL 4%	No
				RA 1%	No

I have not renumbered sections of submitted or published papers in order to generate a consistent presentation within the thesis.

Student signature:  **Date:** 5/12/2017

The undersigned hereby certify that the above declaration correctly reflects the nature and extent of the student's and co-authors' contributions to this work. In instances where I am not the responsible author I have consulted with the responsible author to agree on the respective contributions of the authors.

Main Supervisor signature:  **Date:** 5/12/2017

Acknowledgements

This project has greatly benefited from the support and opportunities that I have been given over the past four years. My supervisors Laurent Ailleres, Gautier Laurent and Peter Betts have been very supportive throughout my whole candidature. I want to thank Gautier for his continued support even after relocating back to work with the RING team in Nancy. Gautier's guidance in the technical aspect of structural modeling have been invaluable and I don't think I could have achieved half of what I have done in this Ph.D. without his mentorship. Laurent has always been extremely supportive of my work and the direction I have taken the project. Thanks for giving me the freedom to shape this project and to follow different ideas. I am extremely thankful for the support that I have had to present my research at a number of national and international conferences. This research was supported by an Australian Government Research Training Program (RTP) Scholarship.

I would also like to thank my review panel: Roberto Weinberg, Chris Wilson and Sandy Cruden your feedback has been very helpful and had a positive impact on this project. Another thankyou to Chris Wilson for guiding myself and Vitaly around Cape Conran and the surrounding geology highlights. While only a small amount of that work ended up fitting the direction of my thesis I learnt a lot from your discussions and guidance. Thanks to Mark Lindsay for his lecture in 3rd year that provoked my interest in geological uncertainty which eventually lead me down the path of doing this Ph.D.

I would also like to also thank the various people I have collaborated with both on work associated with my thesis or other side projects. I have been part of the Monash Structural Geophysics Group for the past 5 years during both my honours and Ph.D. and our meetings have always been enjoyable. Thanks to all of my office mates over the past few years in different rooms and buildings. Thanks to Guillaume Caumon and the rest of the RING team for the interesting discussions and hosting me during my short visits in 2014 and 2016.

I also want to thank all of my climbing friends for the numerous weekend trips to the Grampians and Arapiles. Outside of my office and my house I have probably spent too many hours bouldering at the Lactic Factory. But climbing and the friends there mean that even a bad day in the office can become a good day!

I didn't get the opportunity to do the original fieldwork planned for my Ph.D. but thanks to the opportunities I have been given from other people I have been able to spend plenty of time in the field. Thanks to Pete, Laurent and Geez for giving me the opportunity to teach at Broken Hill and Bermagui. Thanks again to Geez again for giving me the opportunity to help run and design the Spatial Analyst Course, it was a great challenge and I hope the course continues to be successful in the future!

I also want to thank my family for being extremely supporting for the last few years. Thanks to my granddad Les for the car park on his lawn and its been great being able to have a chat after uni. Thanks to mum and dad for their support and encouragement, I really do appreciate it. Last but not least, my brother Cam for always being up for an adventure whether it was a crazy bike ride or a climbing trip. Thanks for encouraging me to try harder and to push my limits.

Table of Contents

Abstract	iii
Acknowledgements	xi
Chapter 1 Introduction	1
1.1 Background and motivation	3
1.2 Structural modeling	4
1.2.1 Explicit surface representation	4
1.2.2 Implicit surface representation	5
1.3 Geological uncertainty	7
1.4 Forward and inverse modeling	9
1.5 Thesis outline	10
Chapter 2 Implicit Modeling of Folds and Overprinting Deformation	13
2.1 Introduction	15
2.2 Structural description of folded structures	17
2.2.1 Structural data and notations	17
2.2.2 Fold geometry, structural elements and finite strain	18
2.2.3 Defining a curvilinear fold frame	18
2.2.4 Fold frame and structural elements	20
2.2.5 Defining vergence and fold rotation angles	20
2.3 Modeling successive folding events	21
2.3.1 A fold interpolator based on structural elements	21
2.3.2 Backward modeling of successive fold events	22
2.3.3 Simplified fold interpolator for similar folds	22
2.4 Structural fold constraints for discrete implicit scheme	24
2.4.1 Discrete implicit approach	24
2.4.2 Structural fold constraints	25
2.5 Synthetic examples of fold interpolation	26
2.5.1 Modeling fold interference	26
2.5.2 Structurally-controlled fold series interpolation	26
2.5.3 Complex synthetic case study	27
2.6 Discussion and perspectives	33
2.7 Conclusion	34

Chapter 3	Structural Data Constraints for Implicit Modeling of Folds	37
3.1	Introduction	39
3.2	Related work	40
3.2.1	Structural geology of folds	40
3.2.2	Implicit fold modeling	41
3.3	Fold geostatistics	42
3.3.1	Fold axis rotation angle	42
3.3.2	Fold limb rotation angle	43
3.3.3	S-Plot for analysing fold profiles	43
3.3.4	S-Variogram for analysing spatial correlation	44
3.3.5	Synthetic examples	46
3.4	Automatic fold modeling	47
3.4.1	Interpolating fold geometries using Radial Basis Functions	48
3.4.2	Extrapolating fold geometries using Fourier series approximation	49
3.5	Case studies	50
3.5.1	Proof of concept: synthetic fold	50
3.5.2	Implicit modeling of Cape Conran, Victoria	53
3.6	Discussion	56
3.7	Conclusion	57
Chapter 4	Inversion of structural geology data for fold geometry	59
4.1	Introduction	61
4.2	Description and modeling of complex fold geometries	62
4.3	A probabilistic framework for modeling fold geometries	63
4.3.1	Fourier series representation of fold geometry	64
4.3.2	Bayesian inference	64
4.4	Case studies	67
4.4.1	Proof of Concept	67
4.4.2	Parasitic non-cylindrical folding	69
4.5	Discussion	74
4.6	Conclusion	76
Chapter 5	Inversion of geological data and knowledge	77
5.1	Introduction	79
5.2	Geological knowledge and interpretation	80
5.3	Structural modeling of folds as an inverse problem	81
5.4	Adding geological knowledge to the geological inversion	82
5.4.1	Fold tightness	83
5.4.2	Fold vergence	83
5.4.3	Fold symmetry/asymmetry	84
5.4.4	Fold wavelength	85
5.4.5	Interpretations: form lines and axial traces	85
5.4.6	Data polarity and younging	86

5.5	Results	86
5.5.1	1D proof of concept examples	86
5.5.2	Case study: Davenport Province	90
5.6	Discussion	93
5.7	Conclusion	96
Chapter 6 Discussion and conclusion		99
6.1	Introduction and thesis summary	101
6.2	Research implications and future research recommendations	102
6.2.1	Irregular fold wavelength in the geological inversion	102
6.2.2	Fold class	103
6.2.3	Building the fold frame	104
6.2.4	Towards joint geological and geophysical inversions	105
6.2.5	Incorporating faults	106
6.2.6	Inversion of polydeformed terranes	107
6.3	Conclusion	109
Bibliography		121
Appendix A Discrete linear tetrahedral support		123
Appendix B Digital Appendix		125
B.1	3D model supplementary data	125
B.2	1D synthetic examples	125
B.3	StructuralFactory gocad plugin	125
B.4	PyFactory python interface to StructuralFactory	125

List of Figures

1.1	Explicit model of folded surface	4
1.2	Implicit surface representation	6
1.3	Standard implicit modeling of fold train	6
2.1	Outcrop showing interference between multiple fold events	16
2.2	Schematic diagram showing fold frame and fold rotation angles	19
2.3	Fold limb rotation angle and vergence shown for schematic diagram of folded surfaces	20
2.4	Iterative fold modeling process for type-3 interference pattern	23
2.5	Examples showing fold hinge shape parameter	24
2.6	Comparison between classical interpolation and fold interpolation	27
2.7	Map showing input data set for case study	28
2.8	Successive stages of the proposed modeling process	29
2.9	Complex synthetic case study results	31
2.10	Complex case study: comparison of interpolation methods	32
3.1	Outcrop showing structural interpretation	41
3.2	Schematic fold sketch showing fold rotation angles	42
3.3	3D fold diagram showing fold shape and S-Plot	43
3.4	S-Variogram for regular and irregular wavelength folds	45
3.5	Fold geostatistics for 1D fold shape	46
3.6	Fold geostatistics for asymmetrical folds	47
3.7	Problems with standard interpolation methods	48
3.8	Synthetic case study: doubly plunging fold	50
3.9	Synthetic case study: fold frame and fold geostatistics	51
3.10	Synthetic case study: resulting models	53
3.11	Cape Conran aerial imagery and structural map	54
3.12	Cape Conran: fold frame, fold geostatistics and resulting models	55
4.1	Schematic fold showing the fold axis rotation angle	63
4.2	Proof of concept 1-D fold inversion for a sinusoidal fold geometry	67
4.3	Proof of concept 1-D fold inversion for parasitic fold geometry	68
4.4	Case study: map sampled from synthetic doubly plunging parasitic fold train	70
4.5	Case study: fold geostatistics and Bayesian inference results for synthetic example	71
4.6	Case study: sample of 6 models	71

4.7	Case study: model variability for simulation of 200 models	72
4.8	Case study: prior and posterior probability density function for fold wavelength	72
4.9	Case study: variability reduction after adding additional structural data	73
5.1	Geological knowledge likelihood functions	82
5.2	Fold asymmetry likelihood function shown for asymmetrical and symmetrical folds	84
5.3	1D parasitic fold shape using geological knowledge prior for main fold wavelength	87
5.4	Synthetic 1D examples demonstrating different geological knowledge likelihood functions.	88
5.5	1D fold shape with inconsistent surface polarity corrected using geological inversion	89
5.6	Location and geological map of Davenport Province	91
5.7	Davenport Province: fold frame scalar fields	92
5.8	Davenport Province: fold geostatistics and geological inversion	92
5.9	Davenport Province: variability between geological inversion results	93
5.10	Davenport Province: probabilistic representation of form lines from geological inversion	94
6.1	Fold classes defined by dip isogons	103
6.2	Difficulties interpolating fold frame y coordinate	104

List of Tables

5.1	Fold tightness descriptive terms and interlimb angle	83
-----	--	----

Chapter 1

Introduction

1.1 Background and motivation

One of the greatest challenges for geological research and minerals exploration is to predict and represent geology at depth and in three dimensions (3D). Typical geological datasets collection is limited by the availability of outcrops and is usually limited to maps sampled in plan view. In all but the most simple geological settings, the geometry of rock units will vary significantly in three dimensions, particularly when considering the geometry at depth. Predicting the distribution and geometry of rock units at depth is usually achieved by combining observations of the surface geology, geological knowledge and an understanding of the geological history associated with an area. This process can be very subjective and is difficult to do objectively. In principal, a geological model created from data provides an objective method for visualising and predicting the geology at depth.

A geological model is an extension of the geological map into 3D and communicates the geologist's interpretation of the distribution and structural relationships between rocks units (Jessell et al., 2014). Geological models provide a means of testing the internal consistency of geological interpretations and ideas. The process of building a geological model can be very informative about geological processes (Putz et al., 2006). Geological models are increasingly being used as a foundation for additional studies (Caumon et al., 2009). For example 3D geological models have been used for process simulations in petroleum exploration and hydrogeology (e.g. Oliver and Chen, 2011; Refsgaard et al., 2006; Zimmerman et al., 1998), for resource management in the minerals industry (e.g. Vollgger et al., 2015) or to constrain the distribution of rock units for geophysical inversions (e.g. Armit et al., 2014; Blaikie et al., 2014). Regardless of the intended purpose of the geological model the fundamental procedures for building 3D models remain the same. The creation of geological models is an inverse problem where the aim is to be able to sample the possible geological models given direct observations of the geometry of geological features and geological knowledge.

Building 3D models is a highly specialised and costly task (both in time and computing resources). Commercial modeling packages are generally adapted to "simpler" basin geometries or for mine scale modeling where there is a significantly higher density in geological observations. One of the challenges facing 3D modeling is the tendency for current modeling packages to be focused on data fitting instead of incorporating geological concepts to constrain the interpolation algorithms and test the consistency of geological models (Caumon, 2010; Jessell et al., 2010). The current practice is for geological surfaces to be estimated from data that locally defines the location and geometry of the surface (Hillier et al., 2014). Most current modeling algorithms only use the local direct observations of the surfaces being modeled and require subjective user input in the generation of satisfactory surfaces. Generally, different types of geological surfaces (e.g. fault surfaces, sedimentary contacts, intrusives, unconformities) are generated using the same approaches regardless of the varying physical phenomenon they represent (Jessell et al., 2014). In all geological settings, there are additional observations and constraints that can help to further constrain geological interpretations. Current modeling approaches do not easily allow for these observations to be incorporated in an objective way.

Folds are one of the most common features found in deformed rocks that can occur across a range of scales (Ramsay and Huber, 1987). Geometrically folds are defined by localised variations in curvature and can often form regular patterns of curvature (e.g. a fold train). The current practice for modeling surfaces fit surfaces of minimal curvature to the observations. This means that for the geometry of a folded surface to be captured in the model there need to be extensive observations defining the geometry. The ability

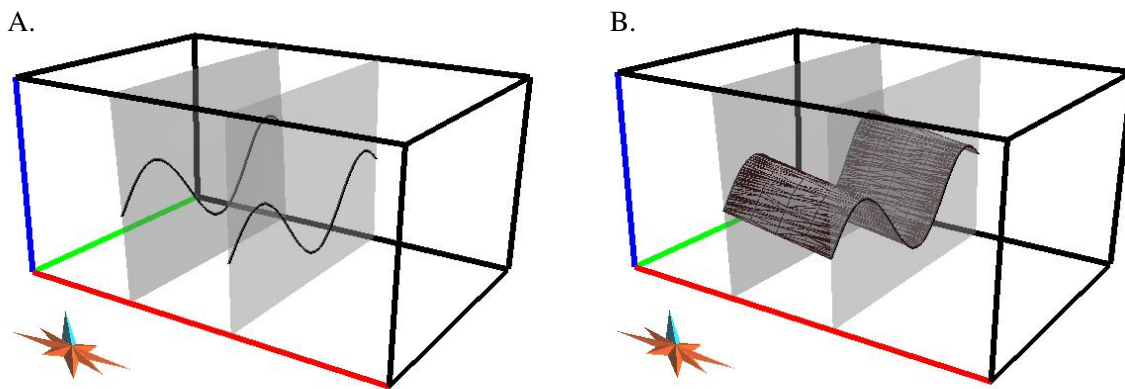


Figure 1.1: A: Two cross sections showing the geometry of a folded surface. B: Surface generated by triangulating the cross section lines from (A)

to characterise and model the geometry of folded surfaces is one of the biggest limitation in current 3D modeling workflows.

1.2 Structural modeling

Geological models are built using a selection of available input data such as field measurements (stratigraphic horizon locations and orientation measurements), drill hole logs and in some cases interpretations of seismic and potential field data. The quality and coverage of the datasets can vary depending on the scale of the model being constructed. Typically, mine scale models will have an abundance of drill hole data reducing the interpolation required between data points. Whereas regional scale models may be limited to more ambiguous datasets such as the interpretation of potential field datasets and require more user input and validation during the modeling process (Jessell et al., 2014).

There are a number of commercial software packages for 3D modeling that employ a wide range of methods and techniques to construct 3D models. There are two main approaches used for representing geological surfaces (*e.g.* stratigraphic horizons and fault surfaces), the *explicit* surface representation and the *implicit* surface representation.

1.2.1 Explicit surface representation

Using explicit surface representation, the geometry of surfaces are contained using a support that is collocated with the surface geometry. The surfaces are represented using discrete objects such as triangulated surfaces, two-dimensional grids or parametric surfaces. The surface geometry is usually built by either directly triangulating data points or using interpolation algorithms to create a smooth surface fitting the data (Chilès and Delfiner, 1999; de Kemp, 1999; Mallet, 1992). The use of interpolation algorithms can allow for data constraining the orientation of the surface to be used (de Kemp, 1999). These tools have been developed to produce geologically reasonable surfaces that can be locally controlled by the modeler's interpretation.

Surfaces that are represented using explicit methods can be easily modified by expert editing where most implementations provide interactive tools to help the geologist modify surface geometries. During

the creation of surfaces, editing can be performed allowing for a model which honours both the input data and the geologist's interpretation of the 3D geometry of an area (Caumon et al., 2009). However, this advantage also comes with a significant disadvantage where the generation of a model can be particularly time consuming with a lot of subjective user input. This means that the model is often not reproducible and as a result can suffer from significant bias.

Explicit modeling provides the geologist with significant control over the resulting model. Each surface in the model has to be represented by a separate support even if the surfaces are conformable. Once fault structures have been defined and horizons within fault blocks are modeled, it can be difficult to edit the fault structure without having to re-interpret the horizon geometry within fault blocks. It also means that any changes in the geometry of conformable surfaces need to be incorporated in all of the surfaces, which can be time consuming and very subjective. Topological relationships between surfaces are not directly incorporated in the modeling framework and are related to the surface supports. Changing and exploring different topological relationships requires modifying the representation of the surfaces and in some cases, may require rebuilding the surfaces or in some cases, the entire model. The ability to easily incorporate the geological knowledge and experience of the geologist into the model building process may sound appealing, it would be more effective if the geologists expertise was directed towards assessing the model's validity based on geological observations and knowledge (Jessell et al., 2010; Wijns et al., 2003).

1.2.2 Implicit surface representation

Using implicit schemes, geological surfaces (*e.g.* stratigraphic horizons and faults) are defined by tracing an isovalue of one or several scalar fields in 3D space (Calcagno et al., 2008; Caumon et al., 2013; Chilès et al., 2004; Cowan et al., 2003; Frank et al., 2007; Hillier et al., 2014; Lajaunie et al., 1997; Mallet, 2002, 2014; Maxelon et al., 2009; Moyen et al., 2004). The value of the scalar field represents the distance away from a reference horizon. For example, some approaches represent each geological surface with an independent scalar field and the scalar field value is the distance to each horizon. Alternatively, if the geological interfaces are conformable the surfaces can be represented by isovalues of the scalar field representing the relative thicknesses between the interfaces. The gradient of the scalar field is a representation of the orientation of the surface being modeled (Maxelon et al., 2009). These scalar fields can be constructed using a variety of different interpolation methods: co-kriging (Calcagno et al., 2008), radial basis functions (Cowan et al., 2003; Hillier et al., 2014) or using Discrete Smooth Interpolation (DSI) on a tetrahedral mesh (Caumon et al., 2013; Frank et al., 2007). Most modeling approaches use the same interpolation algorithms for all types of geological surfaces. Jessell et al. (2014) suggest that as different geological surfaces are related to different physical process then different interpolation schemes may be necessary.

The strength of implicit surface representation for geological modeling is that models can be defined by the implicit function(s) representing the surfaces in the model (Hillier et al., 2014; Lindsay et al., 2012; Wellmann and Regenauer-Lieb, 2012; Wellmann et al., 2010). The implicit functions are constrained by the observations of location or orientation of the surface(s) being modeled, *e.g.* in Fig. 1.2A the arrows represent the normal to the surface being modeled and the lines represent a contact geometry and the line nodes constrain the value of the scalar field at that location. The interpolated scalar field can be sampled throughout the model, in Fig. 1.2B the scalar field has been interpolated using DSI (Caumon et al., 2013; Frank et al., 2007; Mallet, 1992) on the regular triangular mesh in Fig. 1.2A. These interpolation methods mean models can be created with less bias and more reproducibility, and generally the time taken to produce

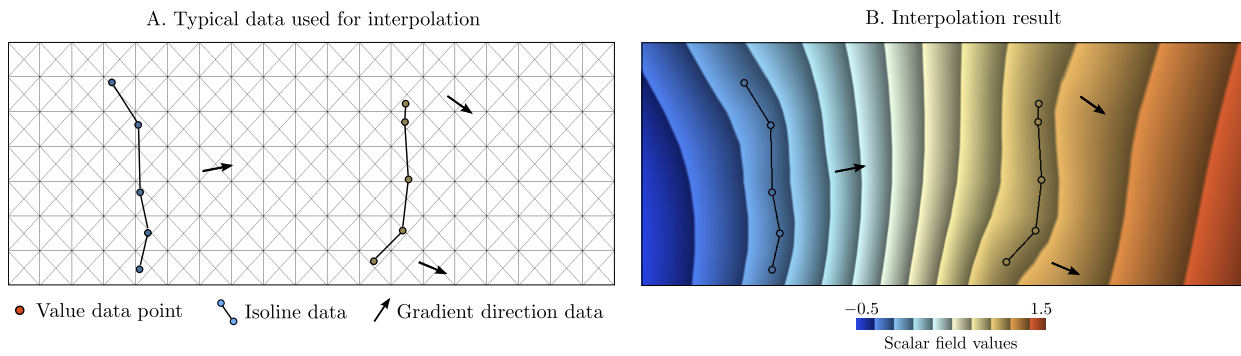


Figure 1.2: 2-D example of Discrete Smooth Interpolation from (Laurent, 2016) A: Triangular mesh and data used to define the interpolation. B: Interpolated scalar field on triangular mesh using the constraints from (A)

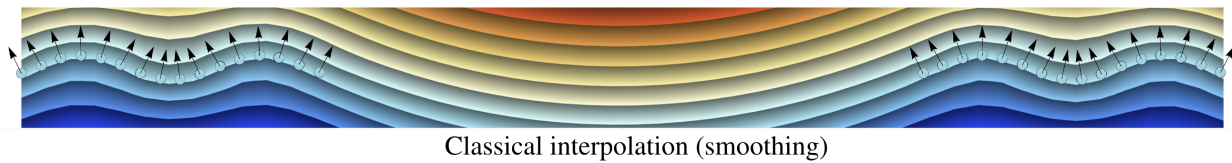


Figure 1.3: Implicit modeling algorithms applied to fold train showing unrealistic result between outcrop locations represented by structural measurements (the arrow represents the normal to the measurements).

a single model or a series of models (*e.g.* from a perturbed data set) will be comparable (Lindsay et al., 2012). These methods typically consider the final state of deformation and attempt to produce final 3D surface geometry from spatial measurements such as form lines and surface orientation measurements. It is generally difficult to incorporate geological knowledge directly into the interpolation scheme. This can present challenges for modeling particular geological structures, where the expected surface geometry is determined by combining both geological knowledge and observations. The modeling of faults using the implicit approach is relatively well developed with methods allowing for topology (Calcagno et al., 2008), kinematics (Laurent et al., 2013) and uncertainty (Cherpeau and Caumon, 2015; Cherpeau et al., 2012) to be incorporated into the modeling.

The interpolation algorithms used to build these scalar fields generally use variants of isotropic Laplacian minimization. This is only appropriate when spatial observations are densely sampled relative to the scale of the structure trying to be modeled (*e.g.* outcrop locations in Fig. 1.3). In sparse data settings, this isotropic assumption tends to generate structural geometries that are incompatible with the strong curvature anisotropy classically observed in folded terrains (Lisle and Toimil, 2007; Mynatt et al., 2007) and are highly non-developable (Thibert et al., 2005) (*e.g.* between outcrops in Fig. 1.3).

To constrain the geometry of folds, the geologist is generally required to draw fold profiles on cross sections or level maps, using bedding orientations (Jessell et al., 2014, 2010; Maxelon et al., 2009). Additional foliations and lineations are generally overlooked and not directly used. In particular, the structural information recorded during field studies such as fold axial traces and their structural elements (fold axes, fold vergence and fold overprinting) cannot be used directly as input into the implicit scheme (Jessell et al., 2014).

There have been a few different approaches for incorporating geological assumptions and rules to improve the modeling of folds with implicit surface representation. Maxelon et al. (2009) use the assumption that the fold geometry will be consistent along the axial surface of the fold. The axial surfaces of the fold are first interpolated using standard techniques where the observations of the foliation associated with

folding or the axial surface of the fold are used to constrain the geometry of the axial surface scalar fields. The fold axis geometry is defined by the user manually drawing the fold hinge line onto the isosurfaces representing the axial surfaces of the fold. The geometry of the fold is then defined by drawing a profile of the fold shape while looking down plunge and using the axial surface geometry and the interpretive hinge line (fold axis) geometry to constrain the folded surface everywhere in the model. This approach is still quite subjective as the geometry of the fold has to be defined by user input and the fold axis geometry is constrained by manually drawing the hinge line onto the fold axial surface. Each fold axial surface needs to be identified and modeled using a separate scalar field. This requires all of the fold hinges to be identified prior to building the geological model and provides limited ability to investigate the structural uncertainties. However, this approach does allow for the geometry of the fold to be constrained looking down plunge and the fold axis to be drawn to be consistent with the structural interpretation. This is consistent with how structural geologists produce interpretations.

Another geometrical feature of folds that has been utilized is the orthogonality of the folded foliation and the fold axis. Massiot and Caumon (2010) use this as an additional constraint for DSI interpolation. This approach requires a global definition of the fold axis field, either as a vector field or an assumption of cylindrical folding. There is no additional constraints for the attitude of the folding or the fold shape meaning that this approach will still require the fold geometry to be well sampled. Another caveat with this method is that the fold axis observations may be less constrained than the folded surface orientations meaning that many assumptions are required. An additional constraint enforces a similar fold geometry for conformable folded layers. Interpolating vector fields representing the fold axis is difficult because the fold axis can also be folded and sufficient observations would be required to constrain its geometry.

The strong anisotropy associated with folded surfaces is aligned with the structural elements of the fold. Gumiaux et al. (2003) show that a semi-variogram parallel to the fold axis has a consistently high correlation in comparison to a semi-variogram aligned perpendicular to the axial surface where the correlation decreases and increases with the wavelength of the fold. Hillier et al. (2014) use locally varying anisotropy based on the local orientation of the fold axis to incorporate this anisotropy into the interpolation scheme. The orientation of the fold axis can be defined by local Eigen analysis of the orientation data (Hillier et al., 2013). This approach means that there is no additional complications introduced in trying to interpolate the fold axis geometry. However, a similar issue as Massiot and Caumon (2010) exists where the fold needs to be well defined by data because the fold shape and attitude is still only locally defined by data. The attitude of the fold is not constrained which may be problematic in areas where the topographical relief or drill holes do not constrain the geometry of overturned or inclined folds.

1.3 Geological uncertainty

Geological uncertainty exists both for the collection of the data (measurement error) (Mann, 1993) and also how representative the data is of the geological feature. One approach for dealing with geological uncertainties has been to classify the source of uncertainty into different categories, for example, three types are defined for geological uncertainty (Bárdossy and Fodor, 2001; Cox, 1982; Mann, 1993; Wellmann et al., 2010):

Type 1: data imprecision, error, and bias, *e.g.* the location of a contact or the orientation of the surface,

Type 2: uncertainty related to the unpredictability and randomness in the interpolation, and

Type 3: lack of knowledge about the structure being modeled, *e.g.* how representative are the observations of the geometry of the surface being modeled.

These categories provide a good theoretical starting point for understanding geological uncertainty. However, discretely classifying uncertainty into these categories can be somewhat misleading as there is significant overlap and interconnectivity between the categories. For example, it is unusual that observation recorded from an outcrop will be devoid of all interpretation (Frodeman, 1995). In reality, uncertainties associated with geological observations are cumulative and propagate throughout the study area. For this reason, it is difficult and often impossible to quantify the contributions of these different sources of geological uncertainty. In a lot of cases trying to quantify the uncertainty associated with geological observations simply adds another source of uncertainty to the system.

There has been a recent focus on simulating and quantifying geological uncertainty in 3D geological models (*e.g.* Cherpeau et al., 2010a, 2012; de la Varga and Wellmann, 2016; Jessell et al., 2010; Lindsay et al., 2012, 2013b; Suzuki et al., 2008; Thiele et al., 2016b; Wellmann and Regenauer-Lieb, 2012; Wellmann et al., 2010). In these studies, multiple realisations of the geological model are generated by perturbing the original structural data set or existing model geometry. These approaches have been sampling only Type 1 and Type 2 uncertainties (Wellmann et al., 2010) because the interpolation between outcrops has remained constant. In most of these cases, the associated uncertainty for the geological observations was arbitrarily chosen and is not determined for the particular dataset. While this approach has been effective in producing geologically different models it does not provide any additional value to the modeling workflow. This is because uncertainty is only introduced where there are constraints within the model and the interpolation methods do not consider the type of structure being modeled, *e.g.* folded surfaces are modeled in the same way as unconformable surfaces or fault surfaces (Jessell et al., 2014). It also means that while more data could be incorporated into the model targeting areas of high uncertainty, these areas are not necessarily associated with the geology.

There have been two main approaches to quantifying the uncertainty in geological models. (1) local methods, where the aim is to quantify the uncertainty within a model at all locations (Lindsay et al., 2012; Wellmann and Regenauer-Lieb, 2012), or (2) a global approach where the model space is classified using multivariate statistics (Li et al., 2014; Lindsay et al., 2013b; Suzuki et al., 2008). These studies have been limited by the interpolation methods and the need to incorporate subjective interpretive constraints into the model (Caumon et al., 2009; Jessell et al., 2014). Interpretive constraints can be subjective and can introduce additional human bias (Bond et al., 2007a). Another issue is that the simulated uncertainties are effectively assessing the sensitivity of the interpolation algorithms and there has been limited assessment of the uncertainty associated with the interpolation algorithm or the description of the geological surfaces (Aug et al., 2005).

In previous methods, most of the simulated structural uncertainty has been associated with fault geometries (*e.g.* de la Varga and Wellmann, 2016; Lindsay et al., 2012; Wellmann and Regenauer-Lieb, 2012; Wellmann et al., 2010). Folds have typically been difficult to model using implicit approaches because the interpolation algorithms generally fit the smoothest surface to the resulting model and folds generally create regular patterns of localised curvature variation. For this reason, when the structural observations are perturbed (de la Varga and Wellmann, 2016; Lindsay et al., 2012; Wellmann and Regenauer-Lieb, 2012; Wellmann et al., 2010) the interpolation algorithm are likely to smooth the introduced perturbations and the resulting model variability will not reflect the uncertainty in the geological structures.

1.4 Forward and inverse modeling

There are two types of problems involving physical systems: the forward problem and the inverse problem (Tarantola, 2005). The forward problem is the matter of predicting the results of measurements given observations of the physical system. In a geological modeling context, this would be equivalent to having a set of parameters that describe the geometry of geological surfaces within the model volume and then being able to predict where a geological contact is and what the orientation of the surface is. For any given combination of parameters, there should only be one possible unique solution. The inverse problem involves using observations to infer the parameter values. There are an infinite number of solutions to the inverse problem as there can be any number of combinations of parameter values that can give the same observations throughout the model. There are two main challenges for solving inverse problems: 1. finding a single model that represents the observations and; 2. characterising the associated uncertainty with the model (Tarantola, 2006).

Both of these challenges effectively stem from the usually nonlinear relationship between the model linking the observations and parameters (Mosegaard and Tarantola, 1995). A simple way to visualise the problem of finding parameter values given observations is to consider a simple two dimensional system. This is similar to finding the highest point in a hilly area. If there are two hills and one has very steep slopes but has the highest peak then this location best fits the observations, however simply describing this combination of parameters does not capture the complexity of the system. In a more complicated system of multi-dimensions, it can be difficult to simply find this ‘peak’ let alone actually describing the associated parameter distributions.

There are fundamentally two different approaches that are used to infer model parameters from observations: the Frequentist approach and the Bayesian approach. Frequentism and Bayesianism differ their definition of probabilities. The frequentist defines a probability as fundamentally related to the frequency of events (VanderPlas, 2014). Uncertainties in the parameter estimates are confined to noise in the data. Bayesianism defines probability as degrees of knowledge (Malinverno and Parker, 2006; VanderPlas, 2014). For inferring the parameter values of a model this would mean that the Bayesian approach would consider the possible values that the model variables could have perhaps defined by knowledge of the particular system or physical limitations and then use the observations to falsify models generated from this parameter space (Tarantola, 2006).

Both Bayesian and Frequentist approaches provide a means of sampling the non-uniqueness of the solution to the inverse problem. Within a Bayesian framework, the joint posterior distribution of the parameter values can be sampled using sampling techniques such as the Markov Chain Monte Carlo approach. Frequentists can perform resampling approaches such as *bootstrap* (Efron and Tibshirani, 1993) or *jackknife* (Rock and Rock, 1988) where the observations are subsampled and the inference is performed on the subsampled populations (Bárdossy and Fodor, 2001). The resulting uncertainty in the parameter values can be assessed by looking at either the joint posterior distribution or using statistical analysis on the resampled results.

1.5 Thesis outline

The primary aim of this thesis is to address the problem of characterising the geometry and uncertainty of folded surfaces in the subsurface and in three dimensions using sparse field observations and geological knowledge. This can be divided into three sub-aims: a method for incorporating geological observations and knowledge of fold geometries into implicit modeling schemes, a method for determining the geometry of folds from observations and incorporating uncertainty of the fold geometry into the modeling scheme. The thesis is structured with six chapters: Chapter 1 contains a literature review and summary of the relevant techniques and methods used in this thesis, chapters 2 to 5 are independent research articles addressing the sub-aims of the thesis and chapter 6 summarises the contributions of this thesis. Monash University allows students to submit Ph.D. theses where research chapters are stand alone research articles. This results in some repetition in the motivation and methods for each chapter.

Chapter 2: *Implicit modeling of folds and overprinting deformation*, (Laurent, G., Ailleres, L., Grose, L., Caumon, G., Jessell, M., Armit, R., 2016. *Implicit modeling of folds and overprinting deformation. Earth and Planetary Science*). This chapter introduces a framework for incorporating folds into implicit modeling schemes. The fold frame is introduced which is a new coordinate system based on the structural geology of folds. The coordinate system is built so that the coordinates represent the geometry of the axial foliation and average fold axis direction. The orientation of the folded surfaces can be defined throughout the model volume by rotating the fold frame by two rotation angles, one defining the geometry of the fold axis within the axial surface of the fold and a second defining the geometry of the fold shape viewed looking down plunge. The folded foliations are modeled backwards in time starting with the most recent (smoothest). In this chapter only, the fold shape is controlled and a cylindrical fold axis is used. The fold shape is defined using an analytical function based on a modified sinusoidal geometry. The parameters controlling the fold geometry (wavelength, amplitude, and asymmetry) are determined in a trial and error based approach. Dr. Gautier Laurent is the first author of this chapter and it has been included in this thesis as a research chapter instead of an appendix because the methods introduced here form the starting point of the following chapters. This candidate contributed to the conceptual development and testing of the modeling method, implementation of the associated Gocad plugin (StructuralFactory) and drafting of the manuscript.

Chapter 3: *Structural data constraints for implicit modeling of folds*, (Grose, L., Laurent, G., Ailleres, L., Armit, R., Jessell, M., Caumon, G., 2017. *Structural data constraints for implicit modeling of folds. Journal of Structural Geology*). This chapter addresses the problem of using structural data to characterise the geometry of the fold. The fold frame coordinates as a reference system for geostatistical analysis of the fold geometry. Within this system, the geometry of folded surfaces can be extracted, even from sparse data, as the fold frame is interpolated to capture the structural elements of the fold (fold axis direction and the fold axial surface). The fold geometry can be interpolated within this framework, the fold axis and fold shape can be represented by two separate 1D curves. Two interpolation methods are proposed for characterising the geometry of the fold: the first method using radial basis interpolation is applicable when the fold geometry is well described by the data and the second using a Fourier series is suitable when there are significant gaps in the data. The fold geostatistics are used to test which method is applicable.

Chapter 4: *Inversion of structural geology data for fold geometries*, has been submitted to Journal of Geophysical Research: Solid Earth. In this chapter, structural modeling of folds is framed as an inverse problem and Bayesian inference is used to determine fold geometry from structural observations. This

allows for the uncertainty in the structural model to be incorporated directly into the interpolation process. This approach means that high regions of variability between the resulting geological models are associated with the structural complexity and can be used for targeting additional data collection to reduce geological uncertainty.

Chapter 5: *Inversion of geological data and knowledge*, is in-preparation for submission to Earth and Planetary Science Letters. This chapter uses the inversion framework presented in chapter 4 and introduces a method for incorporating geological knowledge and indirect structural observations into the geological inversion. These developments allow for models to be created from poor quality and sparse data sets. They also provide the potential for real time geological modeling during mapping where uncertainties could be propagated and assessed while collecting data.

Chapter 6: *Discussion and conclusion*. Summarises and presents further discussion on the findings of the research chapters and presents scope for further research where appropriate.

Chapter 2

Implicit Modeling of Folds and Overprinting Deformation

G. LAURENT^{1 2}, L. AILLERES¹, L. GROSE¹, G. CAUMON², M. JESSELL³, R. ARMIT¹

¹School of Earth, Atmosphere and Environment, Monash University PO Box 28E, Victoria, Australia

²GeoRessources (UMR 7359), Université de Lorraine-ENSG, CNRS,CREGU
Campus Brabois, TSA 70605, 54518 Vandoeuvre-lès-Nancy Cedex, France

³The University of Western Australia, Centre for Exploration Targeting,
School of Earth and Environment, Perth, Western Australia, Australia

Earth and Planetary Science Letters, 456 (2016), 26-38; doi:10.1016/j.epsl.2016.09.040

Abstract

Three-dimensional structural modeling is gaining importance for a broad range of quantitative geoscientific applications. However, existing approaches are still limited by the type of structural data they are able to use and by their lack of structural meaning. Most techniques heavily rely on spatial data for modeling folded layers, but are unable to completely use cleavage and lineation information for constraining the shape of modeled folds. This lack of structural control is generally compensated by expert knowledge introduced in the form of additional interpretive data such as cross-sections and maps. With this approach, folds are explicitly designed by the user instead of being derived from data. This makes the resulting structures subjective and deterministic.

This paper introduces a numerical framework for modeling folds and associated foliations from typical field data. In this framework, a parametric description of fold geometry is incorporated into the interpolation algorithm. This way the folded geometry is implicitly derived from observed data, while being controlled through structural parameters such as fold wavelength, amplitude and tightness. A fold coordinate system is used to support the numerical description of fold geometry and to modify the behavior of classical structural interpolators. This fold frame is constructed from fold-related structural elements such as axial foliations, intersection lineations, and vergence. Poly-deformed terranes are progressively modeled by successively modeling each folding event going backward through time.

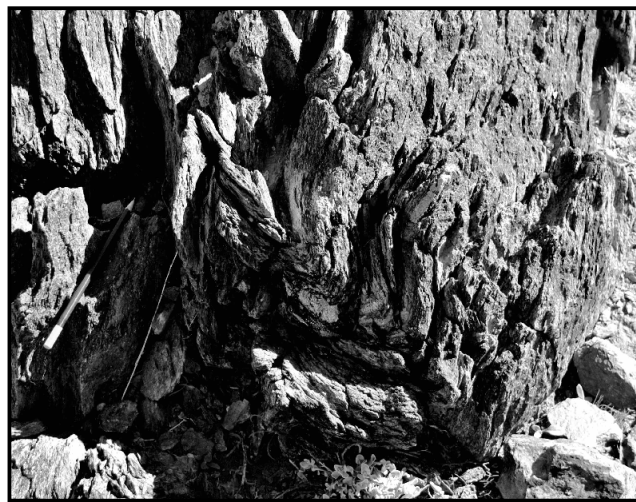
The proposed framework introduces a new modeling paradigm, which enables the building of three-dimensional geological models of complex poly-deformed terranes. It follows a process based on the structural geologist approach and is able to produce geomodels that honor both structural data and geological knowledge.

2.1 Introduction

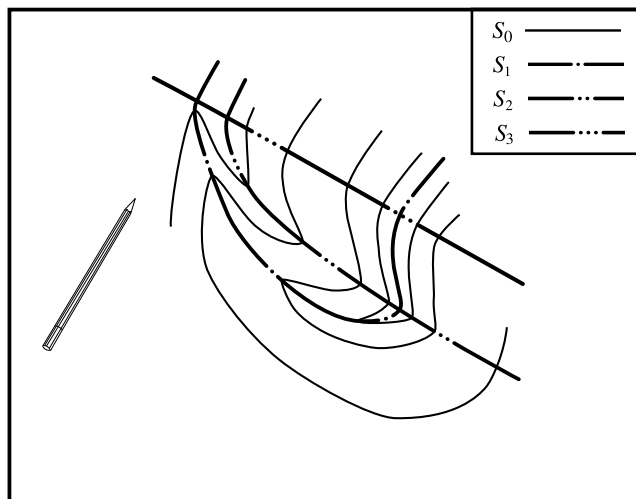
Three-dimensional modeling of geological structures is becoming an essential component of quantitative geoscientific research. For example, it helps to address challenges in sediment budget assessment (Guillocheau et al., 2012), seismic mechanism and seismic hazard studies (Li et al., 2014; Shaw et al., 2015), and natural resources characterization (Cox et al., 1991; Mueller et al., 1988; Vollgger et al., 2015). However, the construction of a three-dimensional structural model from available observations remains a challenging task. 3D structural modeling techniques are essentially data-driven processes honoring spatial observations (Jessell et al., 2014). In most cases, these techniques rely on expert knowledge for overcoming the sparsity and uncertainty of available observations (Maxelon et al., 2009). Structural geology concepts are generally incorporated in the process through interpretive elements in the form of maps, cross-sections or control points (Caumon et al., 2009). Because these elements cannot be easily changed and represent the interpretation of the modeler, they also make this process slow, deterministic, and difficult to reproduce. Any expert editing is subjective and may introduce human bias (Bond et al., 2007a). This limits the understanding of uncertainties, which have to be assessed for a structural model to fulfill its role (Bond, 2015; Caumon, 2010; Lindsay et al., 2012; Wellmann and Regenauer-Lieb, 2012). One way to study uncertainties consist in producing a suite of possible models instead of a single deterministic one, but this approach is limited by the necessary expert editing of classical structural modeling approaches. Moreover, structural modeling techniques are generally limited to stratigraphic contact location and bedding orientation (Calcagno et al., 2008; Caumon et al., 2013). Some types of structural data are often ignored (Jessell et al., 2014, 2010;

Maxelon et al., 2009), and part of the knowledge collected in the field is actually lost in the process of creating a geological model. A significant challenge is to formalize conceptual information and combine these with all observations.

While the modeling of faults using implicit approach is relatively developed (Calcagno et al., 2008; Cherpeau and Caumon, 2015; Cherpeau et al., 2010a,b, 2012; Laurent et al., 2013), folds have received little attention. Only few contributions provide solutions to locally control fold-related geometries in interpolation methods (Caumon et al., 2013; Hjelle et al., 2013; Mallet, 2004; Maxelon et al., 2009). This is particularly difficult for hard rock terranes, where the continuity of stratigraphic layers and foliations are difficult to establish because of overprinting deformation events (Forbes et al., 2004; Ramsay, 1962a) (Fig. 2.1).



A. Outcrop near Eldee Creek, Australia



B. Structural interpretation

Figure 2.1: Interference between multiple fold events. A: photograph of an outcrop in Eldee Creek, Broken Hill block, Australia, showing complex bedding/cleavage geometry and overprinting relationships. B: structural analysis reveals at least three successive folding events with associated foliations. Note that the complexity of the geometry increases with the age of each deformation event.

A variety of structural modeling approaches exists, which combine numerical methods of interpolation (Calcagno et al., 2008; Chilès et al., 2004; Cowan et al., 2003; Frank et al., 2007; Hillier et al., 2014; Lajaunie et al., 1997; Mallet, 1992, 2014). Interpolation techniques proceed by geometric smoothing between

data points. They perform well for dense data, but generate minimal surfaces when data are sparse, thus minimizing the curvature of the produced surfaces. However, folds are precisely characterized by specific, non-minimal curvature patterns (Lisle and Toimil, 2007; Mynatt et al., 2007).

We propose a method of interpolation which is designed to bridge the gap between data-driven and knowledge-driven methods, and addresses: (1) A better use of available data, in particular structural information related to folds. (2) The development of a time-aware data-driven method that takes into account the whole folding history. This is achieved by modifying the behavior of interpolation algorithms and incorporating a fold description in the interpolation process.

Our description of folding is based on a fold frame (Section 2.2), whose construction relies on observable structural elements (e.g. axial foliation). Deformation events are modeled successively by locally characterizing the relative orientation of their structural elements (Section 2.3). This modeling strategy is implemented in the framework of discrete implicit interpolation techniques (Caumon et al., 2013; Collon et al., 2015; Frank et al., 2007; Mallet, 2014) through a set of specific numerical constraints (Section 2.4). The principles of this modeling strategy are illustrated on various examples of increasing complexity (Section 2.5).

For simplicity, we focus on the deformation of a conformable stratigraphic sequence, excluding faults, intrusions or unconformities. These geological features may be handled as proposed by Calcagno et al. (2008); Caumon et al. (2013); Laurent et al. (2013) or Røe et al. (2014).

2.2 Structural description of folded structures

This section presents some basic structural concepts and structural elements associated with folds. From there, we define a coordinate system used for parameterizing fold geometry and guiding fold interpolation.

2.2.1 Structural data and notations

Various structural observations related to folding may be used as data for building a geological model:

- **Stratigraphic observations:** They comprise the locations where a given stratigraphic contact is observed, and the orientation of bedding. These two observations are not necessarily recorded at the same locations. For example, bedding orientation may also be observed inside a given layer.
- **Direct structural element observations:** Some of the fold features can be directly observed, e.g. hinge locations, fold axis directions or axial surface orientations. These features can be observed along fold axial surfaces.
- **Indirect structural element observations:** Observations of axial surface cleavages, intersection lineations and vergence carry indirect information about fold parameters (e.g. fold amplitude, tightness, wavelength and location of the fold hinges).

The following symbols are used to refer to different stratigraphic and fold features that are considered in this study: D: deformation event, F: folding event, S: foliation field (generally a cleavage associated with a fold axial surface), L: intersection lineation (generally associated with a fold axis).

Each of these features may be indexed by a number that represents the associated relative deformation event (e.g. S_1 for the axial foliation of D_1). Bedding is referred to as S_0 . When dealing with the relationship between successive folding events, the current event is denoted F_i , and any previous or later fold are respectively referred to as F_{i-1} and F_{i+1} .

In our framework, foliations are mathematically represented by scalar fields. Each foliation surface corresponds to an iso-surface of the corresponding field. Lineations are represented by unit vector fields where the vectors are locally parallel to the lineation direction.

The symbol \dagger is used to denote user defined parameters or to distinguish local observations of a given feature from the result of its interpolation. For example, observations of bedding are denoted S_0^\dagger . The orientations of foliations are represented by the gradient of the corresponding scalar field, denoted ∇S . For example, observations of the orientation of a foliation S_1 are denoted ∇S_1^\dagger .

2.2.2 Fold geometry, structural elements and finite strain

Folds are continuous geological structures describing a curved geometry of a geological foliation (e.g. bedding, tectonic cleavages). Fold geometry is commonly characterized by: (1) a hinge, defined as the location of maximal curvature of the deformed foliation; (2) an axial surface, which separates opposed limbs and contains fold hinges; (3) a fold axis, which is defined by the intersection between the deformed foliation and the axial surface; (4) a fold movement direction, which is defined as the direction within the axial surface in which the deformed foliation is sheared or deviated from its original geometry (Grasemann et al., 2004; Ramsay, 1962a).

The geometry of a fold relates to the local principal finite strain directions in which the corresponding folding event developed. These directions are denoted \vec{X} , \vec{Y} , and \vec{Z} , and respectively correspond to the directions of greatest, intermediate, and least elongation. They are denoted with curved arrow as they represent curvilinear axes. Folds develop with their axial surfaces orthogonal to the greatest shortening direction \vec{Z} . Fold movement direction is generally parallel to the greatest elongation direction \vec{X} . For cylindrical folds, the fold axis would generally align with the intermediate direction \vec{Y} . When folds are non-cylindrical, the actual fold axis direction may vary and locally deviates from \vec{Y} . This deviation can become very intense in the case of sheath folds.

Different structural elements may also form as a result of the finite strain associated with a folding event F_i : (1) an axial foliation S_i , orthogonal to \vec{Z} and parallel to \vec{X} , \vec{Y} and the axial surfaces of a fold series; (2) an intersection lineation L_i , which results from the intersection between S_i and S_{i-1} , and is parallel to the fold axis; (3) a stretching lineation T_i , which may develop relatively parallel to S_i in the \vec{X} direction. These structural elements may be observed in the field and should be used for constraining possible fold geometries.

2.2.3 Defining a curvilinear fold frame

The principal finite strain directions are intimately related to folding and provide a consistent framework for describing fold geometry and structural elements. We use this concept to define a coordinate system, referred to as fold frame. It consists in three curvilinear axes, which correspond to each finite strain direction, \vec{X} , \vec{Y} , and \vec{Z} (Fig. 2.2A). The fold frame locates each spatial position with respect to the structure of the fold, and makes it easier to parameterize the fold geometry, especially when several interfering folding events are considered (Fig. 2.1). Each axis bears a coordinate represented by a 3D scalar field, respectively referred to as x , y and z (Fig. 2.2B).

The z coordinate corresponds to a distance measured along \vec{Z} from a reference axial surface of a fold series. This coordinate is convenient for describing the variation of the deformed foliation orientation (Section 2.2.5).

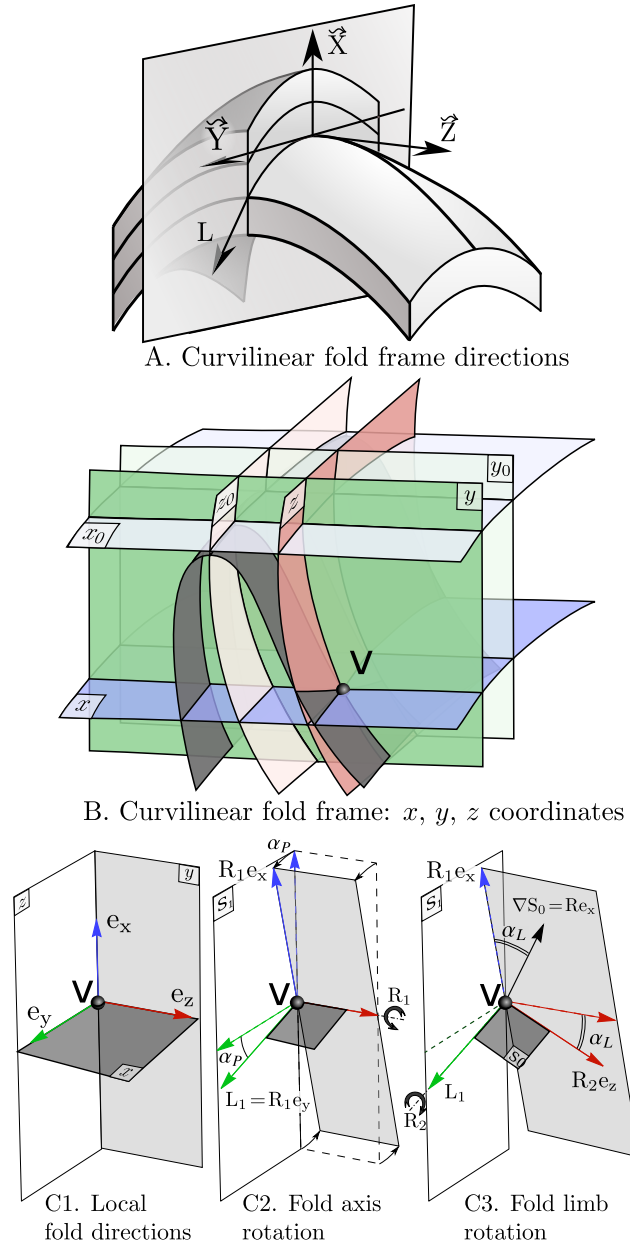


Figure 2.2: Curvilinear fold frame. A: The fold frame axes with respect to fold geometry and fold axis L . B: The curvilinear fold frame coordinates. C: Three local unit direction vectors e_x, e_y, e_z (C1), from which the orientation of the fold axis L_1 (C2) and the deformed feature ∇S_0 (C3) can be derived.

The y coordinate measures a distance along the intermediate axis \hat{Y} from a reference point (e.g. the apex of the fold, if applicable). It could appear more intuitive to define this second axis and coordinate with respect to the fold axis, but the variations of fold axis orientation for non-cylindrical folds would cause the y coordinate to grow at a varying rate depending on the local orientation of the fold axis. The intermediate finite strain direction \hat{Y} defines a more consistent second spatial coordinate, and provides an appropriate framework for describing the variation of fold axis direction in non-cylindrical folds (Section 2.2.5).

Finally, the x coordinate corresponds to a distance measured along \hat{X} from a given reference point. This coordinate is particularly useful for non-similar folds because their geometry varies with respect to x .

Three local direction vectors are implicitly defined by the fold frame for any location v (Fig. 2.2C1) and are used to define the relative orientation of deformed foliations and structural elements (Section 2.2.5).

$$\begin{cases} \mathbf{e}_x = \nabla x / \|\nabla x\| \\ \mathbf{e}_y = \nabla y / \|\nabla y\| \\ \mathbf{e}_z = \nabla z / \|\nabla z\| \end{cases} \quad (2.1)$$

2.2.4 Fold frame and structural elements

As already acknowledged by Maxelon et al. (2009), axial foliations are a key element to effectively parameterize folds. They are relatively consistent and planar over the studied area, at least for the latest events. In this paper we propose to extend this approach by using the full set of available structural observations for building the fold frame and for constraining the fold geometry parameterization. This process exploits the relative orientation of the successive structural elements as detailed in Section 2.3.1.

In practice, various geometrical constraints can be derived from structural observations, for example S_i and S_{i-1} have to be orthogonal at the fold hinge, and L_i has to be parallel to both S_i and S_{i-1} at any location.

Defining a fold frame may also be useful for folds without visible foliations nor lineations as it provides a powerful additional constraint to guide the interpolation of the geometry of the folds.

2.2.5 Defining vergence and fold rotation angles

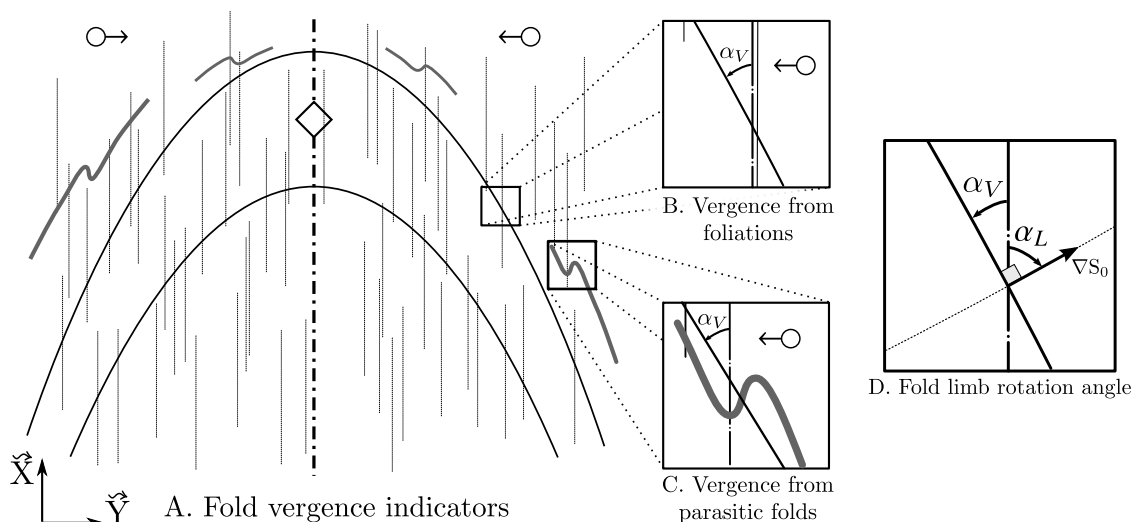


Figure 2.3: Fold limb rotation and vergence. A: Schematic of an antiform in cross-section with axial foliation and parasitic folds. Vergence symbols (O→) represent the direction towards the next antiform in each limb of the fold. Vergence angle is computed either: (B) from an intersection of S_1 and S_0 foliations, or (C) from the asymmetry of parasitic folds. D: Definition of fold limb rotation angle (α_L) with respect to vergence angle (α_V).

The vergence of a given fold is defined anywhere as the relative orientation between the axial foliation S_i and the deformed foliation S_{i-1} . Vergence indicates the direction towards the next fold closure (Fig. 2.3). When quantified as an angle α_V , this measure gives an indication of the relative location of a measurement with respect to the axial surface and the inflexion points of the limbs of a fold. For simplicity, we introduce a fold limb rotation angle α_L , which is defined as the signed complement of the vergence angle (Fig. 2.3D).

$$\alpha_L = \begin{cases} \alpha_V - \pi/2, & \text{if } \alpha_V > 0 \\ \alpha_V + \pi/2, & \text{if } \alpha_V < 0 \end{cases} \quad (2.2)$$

The fold limb rotation angle represents a convenient quantity for parameterizing deformed foliation orientation with respect to the fold frame. It presents the properties of: (1) being 0 at the location of axial surfaces, (2) having an increasing absolute value from the hinges to the limb inflexion points, (3) reaching a local minimum or maximum at the location of the limb inflexion point, and (4) having a sign that corresponds to the orientation of the limb with respect to the axial surface. Vergence and fold limb rotation angles can typically be computed from foliation intersection and parasitic folds (Fig. 2.3BC).

The fold limb rotation angle α_L corresponds to a rotation around the intersection of S_i and S_{i-1} , which is by definition the intersection lineation and fold axis L . With the exception of cylindrical folds, this direction is not parallel to \vec{Y} . In practice, L can also be described by rotating e_y around e_z by an angle α_P , which is referred to as fold axis rotation angle (Fig. 2.2B2).

2.3 Modeling successive folding events

The proposed workflow is similar to how structural geologists construct cross-sections in poly-deformed terranes. The interference patterns that may arise in this situation are typical of the relative orientation of the successive fold events (Grasemann et al., 2004; Perrin et al., 1988; Thiessen and Means, 1980). Figure 2.1 shows that older foliations have a more complex geometry as they are folded by later folding events. In Fig. 2.1, S_3 is relatively straight at the scale of the outcrop, S_2 is openly folded around L_3 fold axis, S_1 is folded around L_2 and L_3 , and S_0 around L_1 , L_2 and L_3 .

When studying this kind of complexly folded structures, it is convenient to analyze the angular relationship between successive structural elements to progressively unravel the structural complexity. We propose to apply a similar sequential approach to structural modeling of complex fold structures.

2.3.1 A fold interpolator based on structural elements

This section defines a fold interpolator \mathcal{F}_i that infers the geometry of a deformed foliation S_{i-1} from a set of observations and fold parameters. \mathcal{F}_i works in four steps: (1) building a fold frame based on observations of structural elements; (2) expressing fold angles α_P and α_L as a function of fold frame; (3) inferring ∇S_{i-1} everywhere in space; (4) interpolating S_{i-1} while taking account of S_{i-1}^\dagger and inferred ∇S_{i-1} .

Building a fold frame

The process for building a fold frame may vary depending on the structural style and available data. Here we describe a general strategy that would cover most cases.

A foliation field S_i is first interpolated including all relevant data (S_i^\dagger , ∇S_i^\dagger , L_i^\dagger). If a folding event that would affect S_i is defined, i.e. F_{i+1} , we use \mathcal{F}_{i+1} as an additional constraint. S_i is taken as the z coordinate of the fold frame. The coordinate y is then interpolated with the constraints for y to be orthogonal to z , and e_y to align at best on L_i^\dagger . The coordinate x is finally interpolated orthogonal to both y and z .

Fold rotation angles interpolation

The fold plunge and limb rotation angles, α_P and α_L , are defined as functions of the local fold coordinates. They can be interpolated from observed foliation and lineation data, and stored as scalar fields. When a

particular fold model is considered, it becomes possible to express α_P and α_L with an analytic function of the fold coordinates (e.g. Section 2.3.3).

Ideally, analytic fold profiles should be fitted to data or used as a basis for data interpolation. Typical parameters for analytic fold profiles would be the fold wavelength λ , a range of fold rotation angle $[\alpha_{Lmin}, \alpha_{Lmax}]$, a hinge shape factor p . This modeling process should also consider that the values of α_P and α_L might be affected by overprinting folding event, for example by superimposing different analytic fold profiles. Combination of profiles is also a way to represent parasitic folds.

Inferring deformed foliation orientation

At any location v , the orientation of the fold axis L_i and deformed foliation ∇S_{i-1} are defined with respect to the local fold frame direction vectors (e_x, e_y, e_z) with the following two rotations (Fig. 2.2C):

- Fold axis rotation R_1 : rotates the whole frame around e_z by a fold axis rotation angle α_P , yielding:

$$L_i = R_1 \cdot e_y \quad (2.3)$$

- Fold limb rotation R_2 : rotates the whole frame around L_i by a fold limb rotation angle α_L (Fig. 2.3D), yielding:

$$\nabla S_{i-1} = R_2 \cdot R_1 \cdot e_z = R \cdot e_z \quad (2.4)$$

For cylindrical folds, L_i is constant in space, and can be represented by a global fold axis vector or rotation angle.

Deformed foliation interpolation

The final stage of the fold interpolator algorithm consists in interpolating S_{i-1} , while taking S_{i-1}^\dagger and inferred ∇S_{i-1} into account. This is achieved by implementing fold related constraints in classical interpolation schemes (Frank et al., 2007; Hillier et al., 2014; Lajaunie et al., 1997). Fold constraints control the orientation of ∇S_{i-1} with respect to fold axis, axial surface and fold limb directions. They also specify how ∇S_{i-1} must vary in space. As an example, Section 2.4 derives these constraints for discrete implicit schemes.

2.3.2 Backward modeling of successive fold events

Understanding the relationship between successive folding events provides a guideline to unravel poly-deformed geometry. The latest deformation event is modeled first, assuming that its associated foliation field S_n should not have been affected by any later deformation and should then be relatively consistent and smooth through the studied area. This assumption makes it relevant to interpolate S_n with classical interpolation tools (Frank et al., 2007; Hillier et al., 2014; Lajaunie et al., 1997). Once the foliation field S_n is built, it is combined with some user-defined fold parameters to build a complete description of the folding event (Section 2.3.3). \mathcal{F}_n is then applied to model S_{n-1} . This process is progressively repeated to model the geometry of older features until the bedding is finally generated (Fig. 2.4).

2.3.3 Simplified fold interpolator for similar folds

Dip isogons (Ramsay and Huber, 1987) correspond to lines of equal α_L . For similar folds, the dip isogons are parallel to the axial surfaces. Therefore, α_L is constant for each iso-surface of z_i and can be expressed

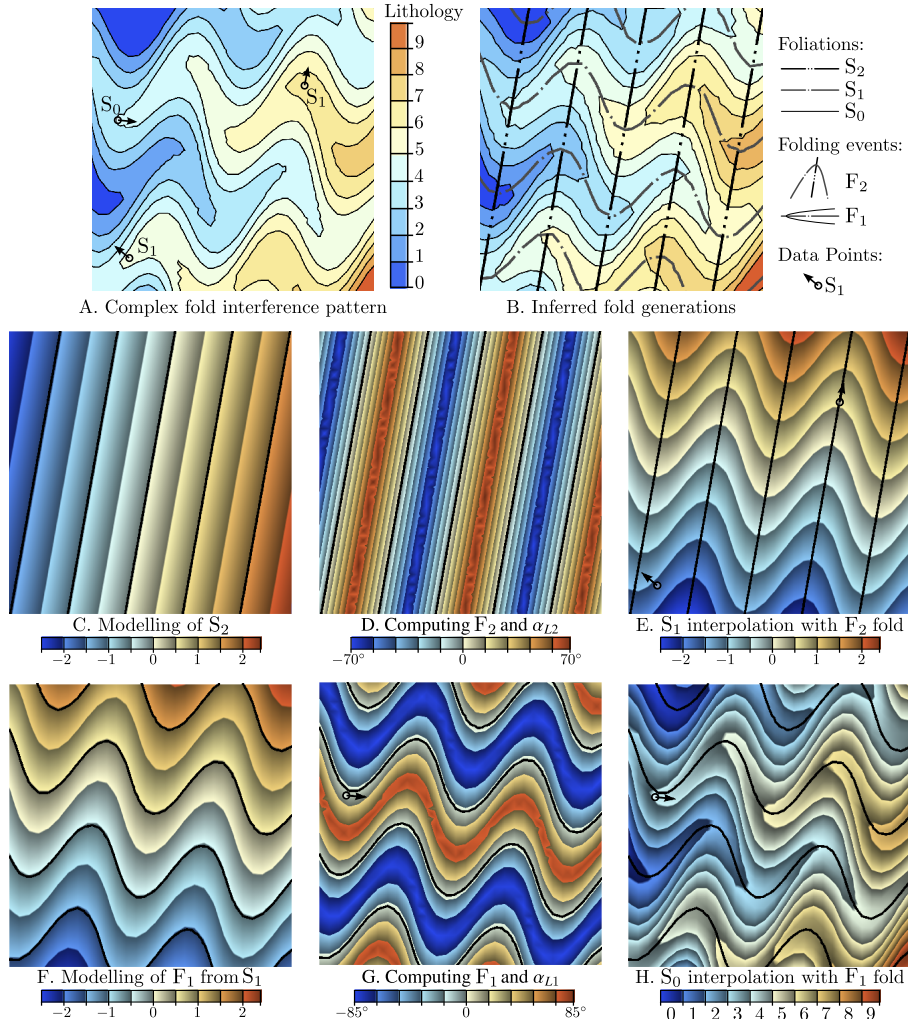


Figure 2.4: Iterative fold modeling process for a type-3 interference pattern (Ramsay and Huber, 1987). A: Complex geometry of S_0 , modeled with a few data points (S_0 and S_1). B: Structural interpretation, basis for the modeling showing the overprinting of two folding events. C: S_2 modeled from a general trend with a classical interpolation process and definition of F_2 axial surfaces (black lines) as isosurfaces of S_2 (imposing a wavelength of 2). D: fold rotation angle α_{L2} modeled as a periodic function of S_2 with α_{L2max} of 70° . E: S_1 interpolation based on S_1^\dagger and \mathcal{F}_2 . F: Definition of F_1 axial surfaces (black lines) from S_1 . G: fold rotation angle α_{L1} modeled as a periodic function of S_1 with α_{L1max} of 85° . H: S_0 interpolation based on S_0^\dagger and \mathcal{F}_1 .

as a function of z only. This allows simplifications of the fold frame. Typically, x does not bring any information and is not explicitly represented. Instead of using Eq.(2.1), e_x is expressed as a cross product of e_y and e_z :

$$e_x = e_z \times e_y \quad (2.5)$$

We propose the following periodic function $\widetilde{\alpha}_L(z)$ as an example of possible parameterization of α_L , λ being the wavelength of the fold with respect to z , $|\cdot|$ the absolute value and $\langle \cdot \rangle$ the fractional part operator:

$$\widetilde{\alpha}_L(z) = 4 \left| \frac{1}{2} - \left\langle \frac{z}{\lambda} - \frac{1}{4} \right\rangle \right| \quad (2.6)$$

The shape of the fold hinge is another important characteristic for describing the geometry of a fold (Jessell et al., 2014). It is represented by the fold hinge shape parameter p (Fig. 2.5). For a same inter-limb angle, the curvature of the fold may be concentrated close to the hinge ($p \gg 1$), evenly distributed between the hinge and the limb ($p = 1$), or spread towards the limbs ($p < 1$). This is implemented with the following equation, where $\alpha_{L\max}$ is the fold limb rotation angle at the inflexion point of the limb:

$$\widehat{\alpha}_L(z) = \alpha_{L\max} \text{Sign}(\widetilde{\alpha}_L(z)) \sqrt[p]{|\widetilde{\alpha}_L(z)|} \quad (2.7)$$

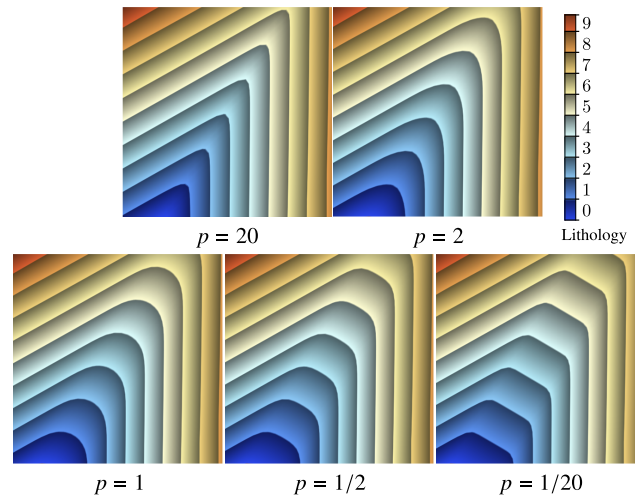


Figure 2.5: Effect of the fold hinge shape parameter p on the shape of the folds. The figure shows an antiform with an $\alpha_{L\max}$ of 60° and an axial surface dipping 30° to the left.

2.4 Structural fold constraints for discrete implicit scheme

In this section, we use our parameterization of fold structures to derive constraints that can be used in the framework of discrete implicit modeling.

2.4.1 Discrete implicit approach

A discrete implicit approach represents geological surfaces as a piecewise linear scalar field φ , which is defined by a discrete volumetric mesh (Caumon et al., 2013; Frank et al., 2007; Mallet, 2002; Moyen et al., 2004). The scalar field is linearly interpolated from the nodal values φ_c of each mesh element. The gradient

of the scalar field $\nabla\varphi$ is constant in each element. Within tetrahedral elements, φ and $\nabla\varphi$ are defined as functions of Cartesian coordinates, \bar{x} , \bar{y} , and \bar{z} , by two matrices \mathbf{M} and \mathbf{T} , which depend on the geometry of the tetrahedron (A):

$$\varphi(\bar{x}, \bar{y}, \bar{z}) = [1, \bar{x}, \bar{y}, \bar{z}] \cdot \mathbf{M} \cdot \varphi_c \quad (2.8)$$

$$\nabla\varphi(\bar{x}, \bar{y}, \bar{z}) = \mathbf{T} \cdot \varphi_c \quad (2.9)$$

The interpolation process finds optimal nodal values with respect to two conditions:

- Data boundary conditions: each observation of either the value of the scalar field or its gradient generates new linear equations by applying Eq.(2.8) and (2.9).
- A regularization term: it enforces the interpolation by smoothing the scalar field between the data boundary conditions. This is implemented by the so-called *constant gradient* constraint or *roughness*, which minimizes the gradient variation between neighbor elements (Frank et al., 2007).

These different constraints generate a system of linear equations, which is solved with a Least Squares approach yielding the corner values φ_c as a solution (Frank et al., 2007).

The *constant gradient* constraint tends to progressively attenuate the orientation variations away from data. This has two consequences on the interpolation:

- Limiting the development of folds: this is because folds are actually introducing orientation variations, which should be used and propagated by the interpolator. In contrast, they tend to be erased by the *constant gradient* constraint.
- Promoting parallel fold shape: they are the type of fold that best spreads the orientation variations, yielding the lowest possible curvature. Therefore parallel folds are promoted by *constant gradient* constraint.

These observations call for the development of another type of regularization term to complement the capabilities of the *constant gradient* constraint.

2.4.2 Structural fold constraints

In addition to the above classical constraints, we propose a series of fold related constraints. Each constraint is defined with respect to the local fold frame direction vectors (e_x, e_y, e_z) and fold rotation angles (α_P, α_L).

Gradient orientation constraints

The orientation of $\nabla\varphi$ has to honor two constraints:

- Fold axis constraint: by definition, $\nabla\varphi$ is orthogonal to the fold axis L_i :

$$L_i^t \cdot \mathbf{T} \cdot \varphi_c = 0 \quad (2.10)$$

- Fold limb rotation constraint: the fold rotation R (Eq. 2.4) constrains the orientation of $\nabla\varphi$ along the axial surface and in the limbs of the fold. This is added to the system in the form of:

$$e_z^t \cdot R^t \cdot \mathbf{T} \cdot \varphi_c = 0 \quad (2.11)$$

Gradient norm and variation constraints

We propose to use the local fold frame direction vectors (e_z, e_x, e_y) for controlling which component of $\nabla\varphi$ may vary. These equations consider two adjacent tetrahedra, whose variables are respectively indexed 0 and 1:

$$e_{x0}^t \cdot R_0^t \cdot \mathbf{T}_0 \cdot \varphi_{c0} - e_{x1}^t \cdot R_1^t \cdot \mathbf{T}_1 \cdot \varphi_{c1} = 0 \quad (\text{parallel}) \quad (2.12)$$

$$e_{x0}^t \cdot \mathbf{T}_0 \cdot \varphi_{c0} - e_{x1}^t \cdot \mathbf{T}_1 \cdot \varphi_{c1} = 0 \quad (\text{similar}) \quad (2.13)$$

When considering parallel folds, the variation of thickness has to be minimized in the direction orthogonal to the folded foliation, i.e. the projection of $\nabla\varphi$ onto $R \cdot e_x$ should be constant (Eq. 2.12). For similar folds, only the apparent thickness in the direction e_x is preserved.

A constraint for controlling the norm of the gradient $\|\nabla\varphi\|$ is also introduced. This may help to improve the quality of interpolated φ when the fold frame is particularly curved, for example when refolding occurs.

$$e_x^t \cdot R^t \cdot \mathbf{T} \cdot \varphi_c = 1/h_p \quad (\text{parallel fold}) \quad (2.14)$$

$$e_x^t \cdot \mathbf{T} \cdot \varphi_c = 1/h_s \quad (\text{similar fold}) \quad (2.15)$$

h_p and h_s denote the local expected thickness of a unit layer for parallel fold and similar fold respectively.

2.5 Synthetic examples of fold interpolation

Three synthetic cases are presented. The first example illustrates the process of modeling successive fold events. The second example demonstrates the possibility to fill a gap of information in a fold series and interpolate structural information. The last example simulates the process of creating a three-dimensional model of refolded layers from field observations.

2.5.1 Modeling fold interference

Figure 2.4 shows a cross-section where an upright fold F_2 overprints a recumbent fold F_1 . This represents a type-3 interference pattern as described by Ramsay and Huber (1987).

This complex structure is obtained by progressively modeling the effect of each fold event, starting with F_2 . S_2 is modeled with a constant orientation through the model. Eq. (2.7) is then applied to compute α_{L2} as a function of s_2 , with λ equals 2 and $\alpha_{L2\max}$ set at 70° , which generates relatively open to tight folds. \mathcal{F}_2 is then used to interpolate S_1 . The process is repeated for modeling S_0 with respect to F_1 , using a $\alpha_{L1\max}$ of 85° and a wavelength of 2.

2.5.2 Structurally-controlled fold series interpolation

Figure 2.6 illustrates the interpolation of an irregularly sampled fold series. This example considers two outcrops with dense data sampling separated by an area lacking observations. Classical interpolation smooths the stratigraphy and fills the gap with a very large synform (Fig. 2.6A), which is inconsistent with the regular wavelength observed in the dataset. With our approach, this dataset may be interpreted as a consistent

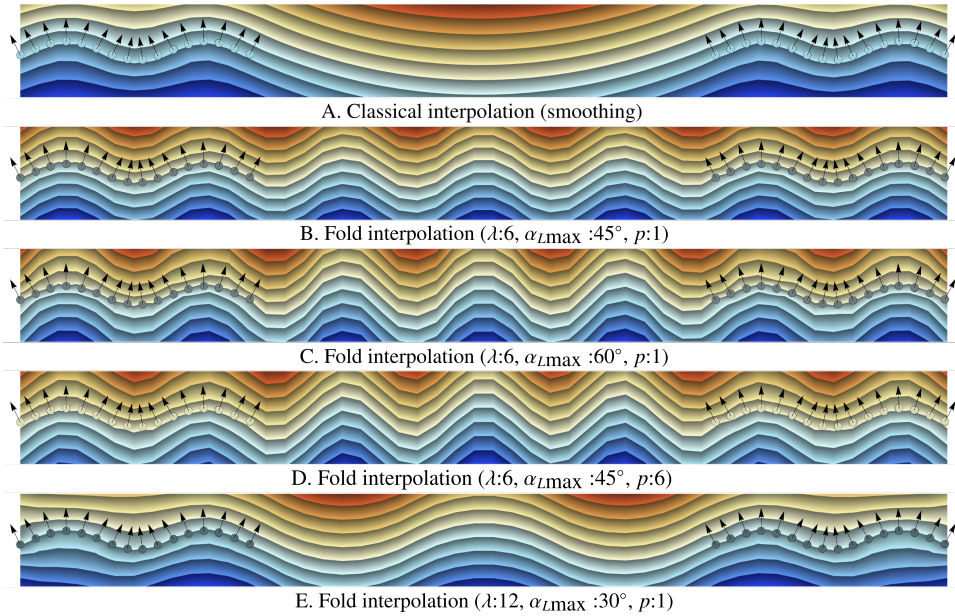


Figure 2.6: Comparison between classical interpolation and fold interpolation. The same data points (circles and arrows) are considered in each interpolation. There is a gap in available data, where the interpolation behavior of each interpolator is observed. A: classical interpolation obtained with a *constant gradient* regularization term. B-E: proposed method of fold interpolation with different fold parameter values.

series of folds. The fold limb rotation angle is computed following Eq.(2.7). Different simulations are produced with varying wavelength λ , inflexion point angle α_{Lmax} and hinge shape parameter p (Fig. 2.6B-E). This illustrates how different fold geometries honoring observation data can be simulated using our parameterization.

2.5.3 Complex synthetic case study

Our last experiment simulates the construction of a complex structural model from field data. We use a synthetic example as it makes it possible to work in a controlled environment and to compare final results with a reference model.

Synthetic reference model and data extraction

The reference model has been created with a history-based approach (Jessell and Valenta, 1996). It represents a series of 11 stratigraphic layers, with varying thickness as shown by the stratigraphic column (Fig. 2.9A). The model is 1 by 1 kilometers large and 500 meters high. A topography representing a valley cutting through a plateau has been simulated, with elevations varying between 20 and 200 meters (Fig. 2.7A). Two folding events are considered:

- F_1 : large scale reclined folds (wavelength: 608m, amplitude: 435m, fold axis: N000E/45°).
- F_2 : upright open folds (wavelength: 400m, amplitude: 30m, fold axis: parallel to L_1).

The two folding events overprint in a type-3 interference pattern (Ramsay and Huber, 1987).

Three outcropping regions have been delineated covering 30% of the modeled area. Data have been extracted from this reference model by picking the orientation of corresponding surfaces or by intersecting them with the topographic surface (Fig. 2.7). Four kinds of data are generated:

- Contacts lines between stratigraphic layers.

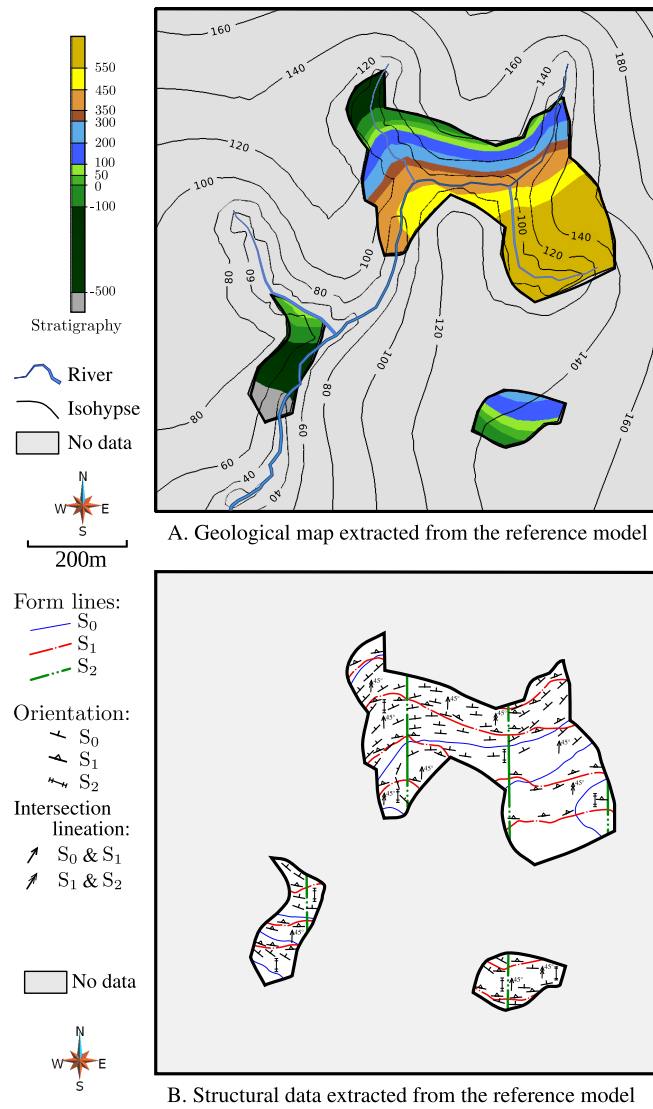


Figure 2.7: Synthetic data generated from the reference model used in this study (Fig. 2.9A). A: Stratigraphic column, topography and stratigraphic outcrop map. B: Structural data gathering foliation orientation measurements, form lines and intersection lineations.

- Form lines of S_0 , S_1 and S_2 .
- Orientation of S_0 , S_1 and S_2 .
- Intersection lineations for F_1 and F_2 .

The chosen sampling of orientation data produces values that are representative of a certain radius around the picked point and has inherent inaccuracy in the way it locates the measurements. This emulates the way orientation data are collected in the field, with location uncertainty and orientation upscaling. This process ensures that generated data carry the same kind of uncertainty as those collected in the field.

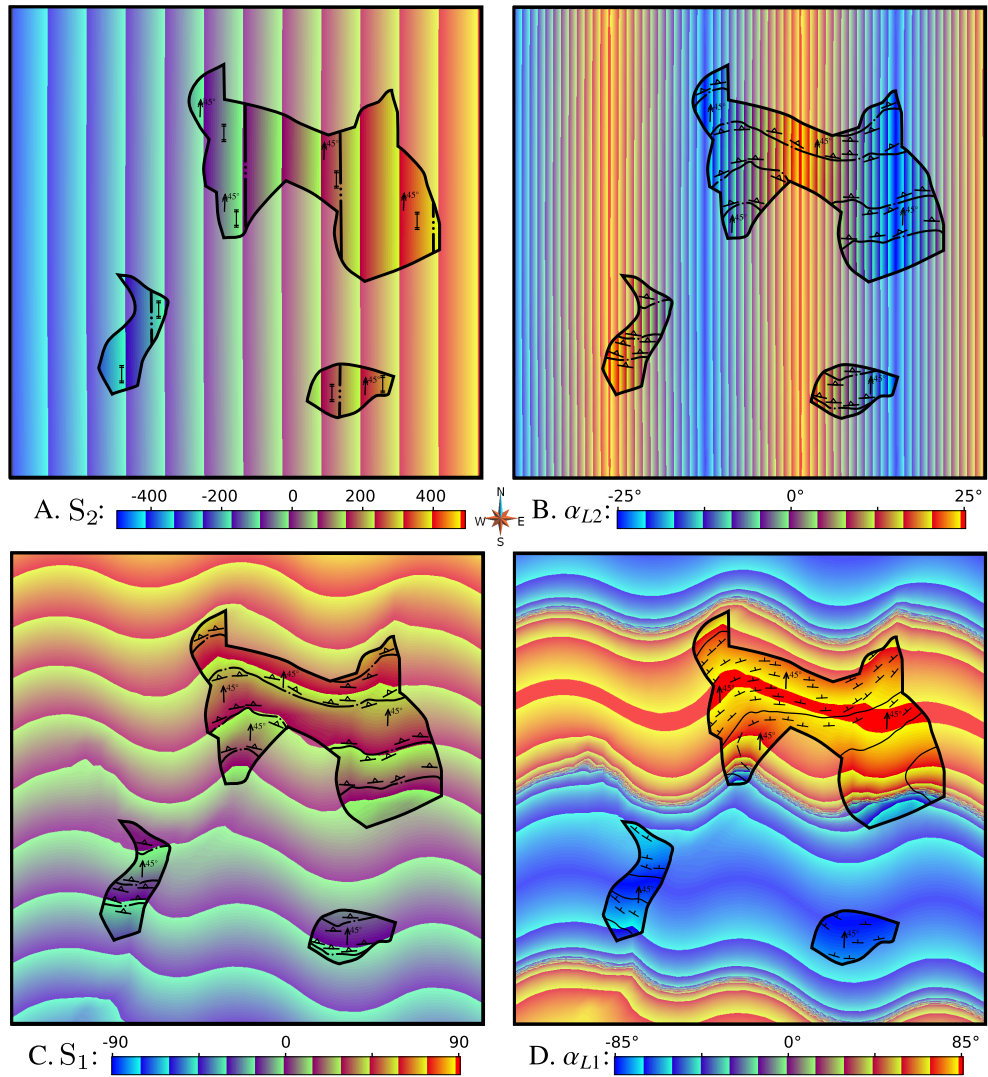


Figure 2.8: Successive stages of the proposed modeling process. Interpolated foliation fields and fold rotation angle are painted on the topographic surface, within and between the outcrop areas (thick lines): S_2 (A), α_{L2} (B), S_1 (C), α_{L1} (D). Visible sharp features of interpolated S_1 and α_{L1} are the effect of the topography. Relevant symbols from Fig. 2.7B are shown to represent the data used for each stage.

Sequential fold modeling process

We apply the modeling process presented in Section 2.3. The following features are successively modeled:

- S_2 (Fig. 2.8A): interpolated from S_2 orientation measurements and form lines. One of the orientation control points is attributed a value of 0 and a gradient norm of 1 to make the interpolation solution unique.

- α_{L2} (Fig. 2.8B): modeled from the geometrical characteristics of F_2 with respect to S_2 with the following parameters: $[\alpha_{Lmin}, \alpha_{Lmax}] = [-25, +25]$, $\lambda = 390$, $p = 1$.
- S_1 (Fig. 2.8C): interpolated from S_1 orientation measurements and form lines with constraints derived from F_2 . Fold constraints that are used correspond to a fold axis constraint Eq.(2.10), a fold limb rotation constraint Eq.(2.11) and similar fold regularization Eq.(2.13). Two additional value data points are introduced in the northern and southern borders of the model to help the interpolated values to stretch in the whole model and limit problems of gradient norm diffusion due to the limited number of value constraints (Laurent et al., 2016). In addition, a similar fold gradient norm constraint Eq.(2.15) appears to be necessary to obtain good results.
- α_{L1} (Fig. 2.8D): derived from S_0 measurement and interpolated S_1 , similarly as in stage 2, with the following parameters: $[\alpha_{Lmin}, \alpha_{Lmax}] = [-80, +80]$, $\lambda = 100$, $p = 5$.
- S_0 (Fig. 2.9C): finally interpolated from S_0 measurements and form lines, with constraints derived from F_1 .

Structural analysis of resulting models

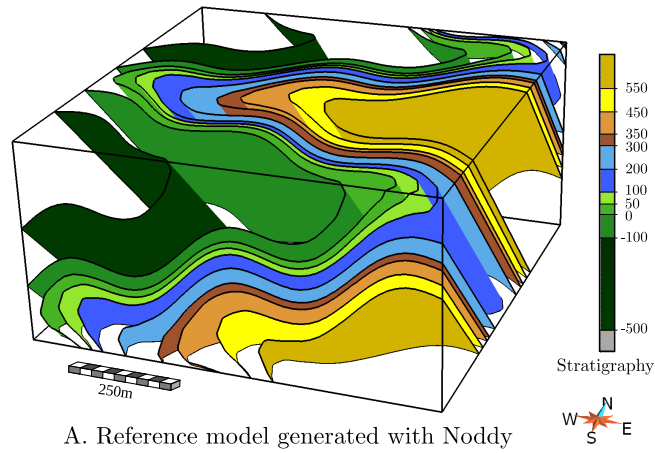
The quality of the result is qualitatively evaluated by comparing with the reference model and the result obtained with constraints used in classical interpolator (bedding contours and orientations, and a fold axis direction) (Fig. 2.9). With this example, classical interpolation honors bedding information and roughly captures the central F_1 fold. But several aspects appear to be very different from the reference model:

- The style of the modeled fold is not correct: the fold obtained corresponds to a parallel fold, and shows no hinge thickening apart from where it is directly constrained by the data, whereas F_1 are similar folds with thickened hinges and attenuated limbs in the reference model.
- F_2 are not visible which causes the limbs of the F_1 fold to be much smoother than in the reference model.
- The style of F_1 hinges is very different from the reference model. They are wide and open in the interpolated model, whereas they are narrow and acute in the reference one.
- There is only one axial surface of F_1 causing the limbs to continue straight without folding again. This results in very different stratigraphy in the South-West and North-West part of the model, where the stratigraphy is not repeated as in the reference model.

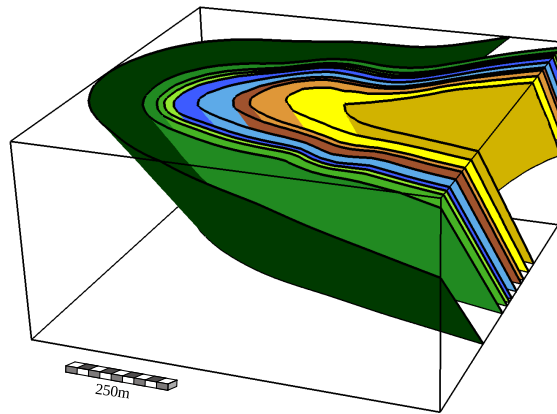
The model obtained with the proposed method (Fig. 2.9C) appears to be much closer to the reference model. Overall, the obtained geometries are more satisfactory when comparing the structural elements of the folds. They honor the principal characteristics of the reference model:

- Several F_1 folds are visible, which makes the resulting stratigraphy much closer from the reference model in the South-West and North-West parts.
- F_1 are close to similar folds, showing hinge thickening, limb attenuation and tight hinges.
- F_2 refolding F_1 are visible, with undulating stratigraphy in F_1 limbs.

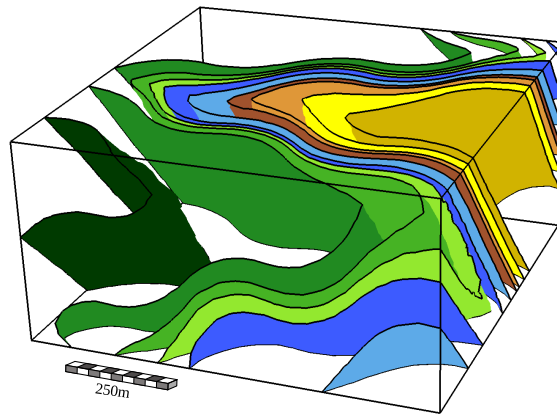
Some differences can still be observed. Mainly, the southern and northern F_1 hinges are slightly shifted as compared to the reference model, which causes the stratigraphy to be different in this regions. This is interpreted as an effect of small variations of S_1 gradient norm on the southern and northern borders of the model, which are related to difficulties in interpolating S_1 . However, these disparities are located in areas that are not controlled by any data, and thus seem very acceptable.



A. Reference model generated with Noddy



B. Model obtained with classical interpolation



C. Model obtained with the proposed interpolation process

Figure 2.9: Complex synthetic case study. A: Reference model generated with a history-based approach (Jessell and Valenta, 1996). B: Result of modeling with classical interpolation constraints (stratigraphy, bedding orientation and F_1 fold axis). C: Result obtained with the proposed approach.

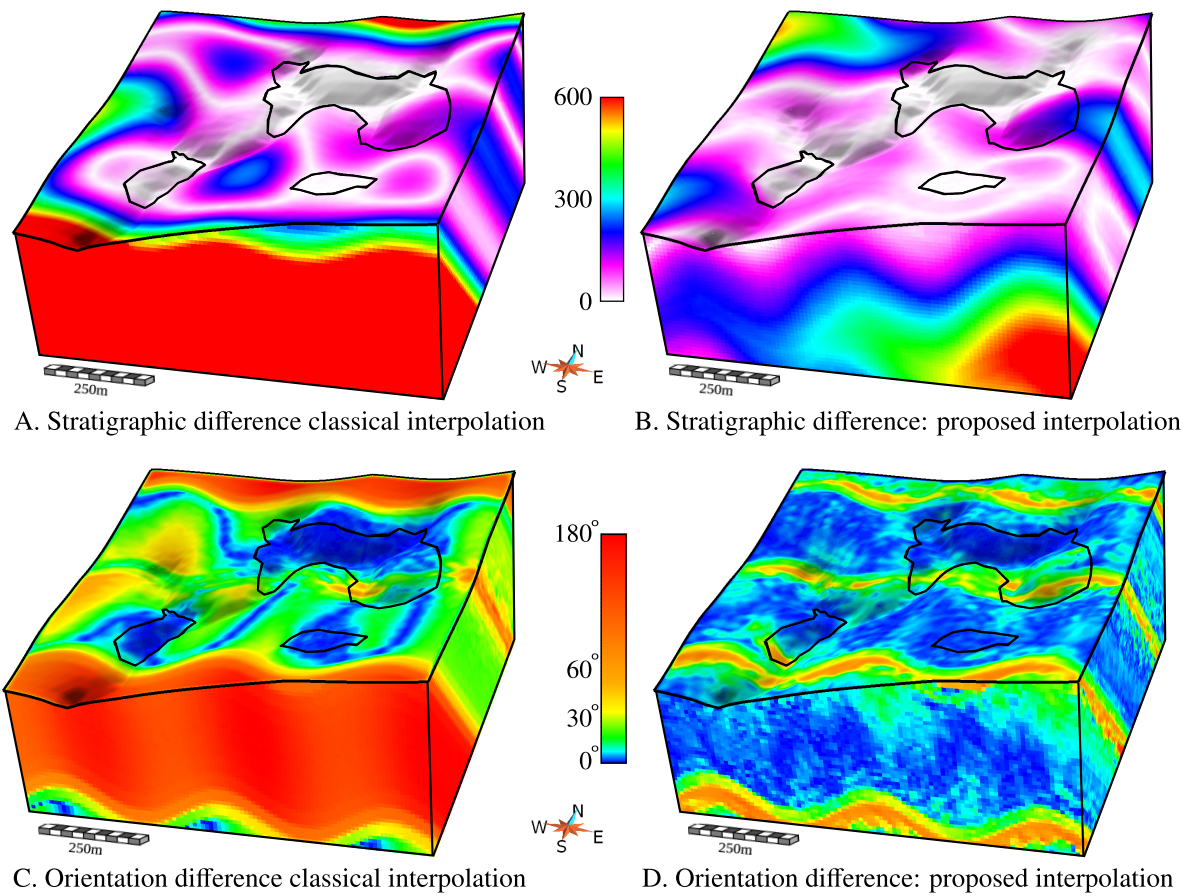


Figure 2.10: Comparison of the results with the reference model: Absolute difference of stratigraphic value obtained with classical interpolation (A) and the proposed fold interpolation process (B) with respect to the reference model; Angle (degrees) between reference model stratigraphy orientation and orientation obtained with classical interpolation (C) and the proposed method (D). The top of the block model corresponds to the topographic surface, with a view of the outcrops (black contour).

Quantitative analysis of resulting models

The quality of the result obtained with a classical interpolation and the proposed fold interpolation method are quantified by measuring the difference in stratigraphic value and orientation with respect to the reference model (Fig. 2.10).

Both interpolation methods generate relatively low errors of stratigraphic value and orientation in the regions with high data density (i.e. outcrops). For the model interpolated with the classical method, the error rapidly increases when going away from the well constrained areas (Fig. 2.10AC).

The proposed method interpolates stratigraphic values that are closer to the reference model (Fig. 2.10B). Important variations are still observed, in particular in the NW and SE corners of the model, which is mainly due to (1) a limited conditioning of this stratigraphic areas, and (2) problems of diffusion when interpolating S_1 (Section 2.5.3). The differences of orientation are concentrated in the F_1 hinges. The location and the shape of the hinges are not correctly accounted for (Fig. 2.10D).

2.6 Discussion and perspectives

Case studies presented in this paper demonstrate how our approach improves the capability of structural interpolator to generate realistic and structurally-controlled stratigraphy, that honors all available structural constraints. Jessell et al. (2014) highlight two limitations of current implicit modeling schemes: (1) they are incapable of interpolating or extrapolating a fold series with a continuous structural style (Fig. 2.6A); (2) the shape of fold hinges they produce is not controlled and may yield inconsistent geometries. These two caveats are addressed by our approach. We are able to interpolate and extrapolate while honoring assumptions about the continuity of the structural style (Fig. 2.6B-E), and about the shape of the fold hinges (Fig. 2.5).

This process needs a practical way to infer fold parameters from field observations. Here, they have been manually determined by comparing the inferred orientation of interpolated foliations to the dataset. This trial and error process was sufficient for proving the concept of our approach, but would be a limitation for complex applications. Early attempts have shown encouraging results in using statistical approaches to derive parameters such as wavelength and fold directions. Unfortunately, the difficulty of this task increases with the complexity of the folds and the number of folding events. We think the fold frame introduced in Section 2.2.3 provides an appropriate structure to carry out such statistical analysis, but this needs to be further developed in future work. Such a tool would have to consider the uncertainties that are related to the determination of fold parameters, for example by using a probabilistic approach. In this contribution, only the parameterization of fold rotation angle for similar folds has been presented. A general method to compute it for any type of fold also needs to be investigated.

There is still a gap between the requirements of the fold modeling process (Section 2.3) and the proposed fold constraints (Section 2.4.2). Here, we focused on the way a fold event would deform the axial surface of an earlier fold. The effect of \mathcal{F} on fold axis and rotation angles also need to be better characterized.

The interpolation schemes that are used represent another point of discussion. The discrete implicit method is able to balance the contribution of each constraint when assembling its linear system. The result may be very sensitive to the relative weight of the different constraints. This is beneficial because it allows

for the relative weights to be adapted to different structural styles and data confidence. Ideal relative weights may be difficult to find and would depend on the quantity and quality of available data.

In the discrete implicit approach, the mesh plays an important role in terms of feature resolution and of computation time. Larger wavelength folds could probably be modeled using a coarser mesh than tighter folds. It would be interesting to adapt the mesh with respect to the modeled fold event. The modeled features are also more likely to present a high curvature close to the fold hinges than in the limb. The mesh could then be adapted to the position in the axial surface field of the current fold. Unfortunately, discrete linear approaches also suffer from limitations related to the underlying mesh as illustrated in Laurent et al. (2016).

In this contribution, the fold axis direction is represented by an angle α_P of rotation of \vec{Y} axis. Alternatively, a 3D vector field interpolated from the fold axis orientation data could be used. This is not the approach we are promoting here as the process of interpolating a direction field needs to be further developed. The description we are using is however compatible with this representation of the fold axis field. The fold axis could also be represented as the gradient of a scalar field, but we advocate that this option would introduce undesired limitations because the curl of such a vector field would be 0, which is not the case of typical fold axis direction field we would like to model.

2.7 Conclusion

Two principal contributions to geological modeling and structural geology are presented in this paper:

- A theoretical and numerical framework for modeling superimposed folding events.
- A series of constraints for discrete implicit modeling schemes dedicated to fold geometry modeling.

Further developments remain necessary to make this technique fully applicable in the context of a real case study. However, this paper represents a step towards a better integration of geological knowledge and structural parameters into the interpolation schemes. The complex synthetic case study presented in Section 2.5.3 proves this approach useful for building structural models from field data, but would now have to be tested on a real case study.

The main development perspectives of this method are the extension of the fold parameterization to other types of folds and the implementation of a robust and efficient method for deriving fold parameters from observation data. This would give the opportunity to develop new kinds of uncertainty studies. Existing literature focuses on the geological uncertainty related to measurement data (Lindsay et al., 2012; Wellmann and Regenauer-Lieb, 2012), which is investigated by perturbing the measurements within uncertainty ranges. Others studies have defined parametric objects to produce stochastic model of faults (Cherpeau and Caumon, 2015; Cherpeau et al., 2010a,b, 2012; Laurent et al., 2013). With our approach, it also becomes possible to produce stochastic fold models by altering or randomly drawing the structural parameters of folds, which would give interesting insights into the contribution of geological structures to the global uncertainty. It would also give better guarantees that models generated during coupled geological and geophysical inversion are actually geologically likely, especially in the context of hard rock terranes.

Acknowledgments

This research was developed at Monash University and funded by Australian Research Council Discovery grant DP110102531 and UWA linkage grant LP140100267. Part of this work was performed in the framework of the “Investissements d’avenir” Labex RESSOURCES21 (ANR-10-LABX-21) and of the RING project at Université de Lorraine. The authors are grateful to the Gocad Research Consortium managed by ASGA (Association Scientifique pour la Géologie et ses Applications, <http://ring.georessources.univ-lorraine.fr/>). We thank Paradigm for providing the GOCAD-SKUA software and API. The presented tools have been implemented in the StructuralFactory plugin for Gocad-Skua, developed by Dr. Gautier Laurent and Lachlan Grose, based on StructuralLab from the Gocad Research Consortium. Data and tools used in this this paper are available upon request to the corresponding author. We would like to thank Gabriel Courrioux and an anonymous reviewer for their very positive comments that helped improve this paper.

Chapter 3

Structural Data Constraints for Implicit Modeling of Folds

L. GROSE¹, G. LAURENT^{1 2}, L. AILLERES¹, R. ARMIT¹, M. JESSELL³, G. CAUMON²

¹School of Earth, Atmosphere and Environment, Monash University PO Box 28E, Victoria, Australia

²GeoRessources (UMR 7359), Université de Lorraine-ENSG, CNRS,CREGU
Campus Brabois, TSA 70605, 54518 Vandoeuvre-lès-Nancy Cedex, France

³The University of Western Australia, Centre for Exploration Targeting,
School of Earth and Environment, Perth, Western Australia, Australia

Journal of Structural Geology, 104 (2017), 80-92; doi:10.1016/j.jsg.2017.09.013

Abstract

A recent method for modeling folds uses a fold frame with coordinates based on the structural geology of folds: fold axis direction, fold axial surface and extension direction. The fold geometry can be characterised by rotating the fold frame by the pitch of the fold axis in the axial surface and the angle between the folded foliation and the axial surface. These rotation angles can be expressed as 1D functions of the fold frame coordinates. In this contribution we present methods for extracting and automatically modeling the fold geometries from structural data. The fold rotation angles used for characterising the fold geometry can be calculated locally from structural observations. The fold rotation angles incorporate the structural geology of the fold and allow for individual structural measurements to be viewed in the context of the folded structure. To filter out the effects of later folding the fold rotation angles are plotted against the coordinates of the fold frame. Using these plots the geometry of the folds can be interpolated directly from structural data where we use a combination of radial basis function and harmonic analysis to interpolate and extrapolate the fold geometry. This contribution addresses a major limitation in existing methods where the fold geometry was not constrained from structural data. We present two case studies: a proof of concept synthetic model of a non-cylindrical fold and an outcrop of an asymmetrical fold within the Lachlan Fold belt at Cape Conran, Victoria, Australia.

3.1 Introduction

Folds are one of the most common features found in deformed rocks (Ramsay and Huber, 1987) but still present a challenge for three-dimensional structural modeling because the geometry of folded surfaces cannot be characterised from individual structural observations. Folds produce localised variations in curvature (Lisle and Toimil, 2007; Mynatt et al., 2007), however interpolation algorithms at the base of structural modeling generally fit a surface of minimal curvature (Jessell et al., 2014; Laurent et al., 2016). To model folded surfaces, the geologist is often required to use additional cross sections, level maps or other interpretive constraints such as synthetic bore holes to produce the expected geometry (Caumon et al., 2003; Jessell et al., 2014, 2010). This approach has proven operative in practice, but it is often cumbersome and reduces the objectivity and reproducibility of the modeling process. Most interpolation algorithms only consider local orientation of the surface and cannot incorporate any additional structural information or geological knowledge. These methods do not incorporate all available structural information collected by field geologists such as: lineations, foliations, overprinting relationships, fold axis, fold axial surface and vergence. This additional structural information can provide excellent constraints on complicated geometries found in hard rock terranes (Laurent et al., 2016).

In implicit modeling systems, geological surfaces such as lithological contacts, fold axial surfaces or fault surfaces are represented by isovalues of a global scalar field (Calcagno et al., 2008; Cowan et al., 2003; Frank et al., 2007; Hillier et al., 2014). The scalar field is interpolated using some of the available geological observations (*e.g.* orientation, lithology type, structural trend). A number of different interpolation methods exist (Aug et al., 2005; Calcagno et al., 2008; Caumon et al., 2013; Cowan et al., 2003; Frank et al., 2007; Moyen et al., 2004). These methods typically consider the final state of deformation and attempt to produce final 3D fold geometry from spatial measurements such as form lines, and strike and dip measurements. However, these methods generally use variants of isotropic Laplacian minimization, which is only appropriate when spatial observations are densely sampled. In sparse data settings, this

isotropic assumption tends to generate structural geometries that are incompatible with the strong curvature anisotropy classically observed in folded terrains (Lisle and Toimil, 2007; Mynatt et al., 2007) and are highly non-developable (Thibert et al., 2005).

The problem of geometrically modeling folds has been addressed by a number of authors (Hillier et al., 2014; Laurent et al., 2016; Massiot and Caumon, 2010; Maxelon et al., 2009; Thibert et al., 2005). These approaches have provided the framework to incorporate the fold axial surface (Laurent et al., 2016; Maxelon et al., 2009; Thibert et al., 2005), fold axis (Hillier et al., 2014; Laurent et al., 2016; Massiot and Caumon, 2010) and a description of fold geometry and overprinting relationships (Laurent et al., 2016). Laurent et al. (2016) introduced a global fold frame which provides a reference coordinate system for each deformational event based on the structural elements of the fold. This allows for the geometry of older folds to be described without the effects of younger deformation events. For each folding event two rotation angles are calculated from field data: (1) the fold axis rotation angle, and (2) the fold limb rotation angle. To parametrise the variations of these two angles with respect to the fold frame, Laurent et al. (2016) use a periodical fold shape, which depends on estimations of fold wavelength, amplitude and location of fold hinges. In Laurent et al. (2016) these parameters are inferred using trial and error.

In this contribution, we present a method for directly extracting and characterising the geometry of folds from field data. The two fold rotation angles that are necessary for characterising a fold geometry can be calculated locally from field observations and interpolated throughout the model volume using multiple scalar and vector fields. We present two approaches for characterising the fold rotation angles within the fold frame: (1) standard interpolation, where there is enough structural data to characterise the fold shape, or; (2) a combined interpolation and extrapolation method using a Fourier series to represent the fold geometry. Where insufficient observations exist to characterise the geometry of the fold throughout the model volume, the Fourier series approximation of the fold geometry provides a geologically reasonable estimate that is objectively defined by the structural observations. We demonstrate these approaches on: (1) a synthetic example of a doubly plunging fold series, and (2) asymmetrical folds from Cape Conran, Victoria.

3.2 Related work

3.2.1 Structural geology of folds

Structural geologists describe the geometry of folds using the geometrical characteristics of the folded surfaces (Ramsay and Huber, 1987, p. 311-317): (1) the fold hinge is the location of maximum curvature for the folded surface, (2) the axial surface separates opposing limbs and contains fold hinges of conformable surfaces, and (3) the fold axis as either the fold hinge line or the line of intersection between the folded foliation and the axial foliation.

A planar fabric can often be observed orthogonal to the direction of principal shortening and roughly parallel to the fold axial surface (Hudleston and Treagus, 2010; Ramsay and Huber, 1987). This foliation can be used in a general case, to characterise the geometry of the axial surface away from fold hinges. This fabric is often pervasive and is commonly recorded by geologists to map the geometry of the fold axial surface. The intersection of this foliation and any older folded foliation provides a lineation that is parallel to the direction of the fold axis. These foliations and lineations can themselves be deformed by later folding events. By identifying structural elements of successive folding events and mapping their spatial

distributions and overprinting relationships, structural geologists are able to unravel complicated geological structures (e.g. Armit et al., 2012; O’dea et al., 2006).

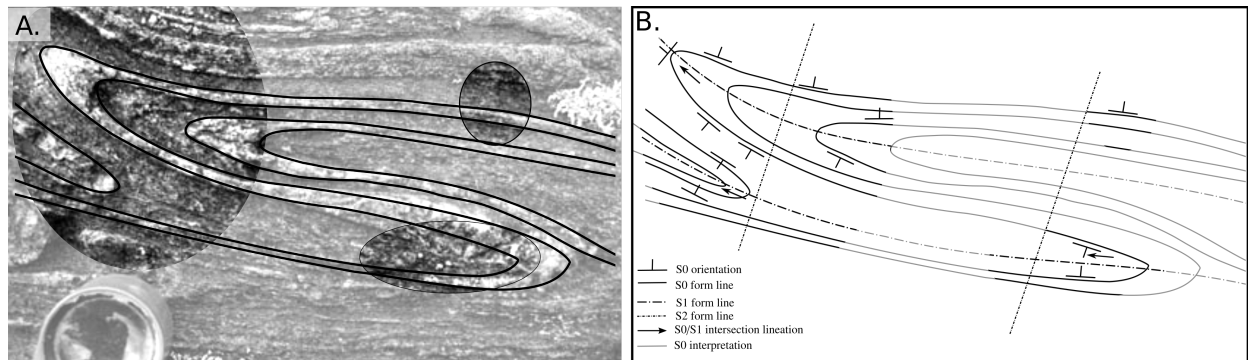


Figure 3.1: A: Outcrop from Kinlochleven, Scotland of a refolded fold (Hilgers, 2006). B: A schematic sketch showing the possible structural observations that could be collected from key locations highlighted areas in (A). The fold hinges are located at the intersection between S_0 and S_1 form lines, the fold axis cannot be observed in the photograph and the S_1 form lines represent the intersection between the axial surface and the outcrop surface. Light lines represent a possible interpretation between these key locations.

In a typical field mapping campaign, a structural geologist will systematically record the orientation of foliation surfaces and associated lineations (Ramsay and Huber, 1987, p. 677-678). These geometrical observations are typically interpreted and summarised onto a map as form lines. Fig. 3.1A shows the bedding trace of a small outcrop and Fig. 3.1B shows the relevant structural information that could be used to unravel the geometry of this outcrop from only selected areas. Form lines are usually a representation of the trend of observations and will often record at the scale of the map, the overprinting relationships that can be observed in and between outcrops (Alsop and Holdsworth, 1999; de Kemp, 2000; Lisle, 2003). Form lines that represent the trace of the axial surface record the location of the fold hinge.

3.2.2 Implicit fold modeling

Laurent et al. (2016) use the structural elements of the fold (fold axis, axial foliation and fold vergence) to define additional orientation constraints for implicit modeling. A fold frame is defined with coordinates represented by 3D scalar fields, denoted as x , y and z . Three local direction vectors (e_x , e_y and e_z) are implicitly defined by the fold frame coordinates for any location and are used to define the relative orientation of deformed foliations and structural elements. One of the main ideas of the method is to use classical interpolation (and the associated isotropic smoothness assumption) on the least deformed surfaces defining the fold frame, then to use this information to allow for anisotropic interpolation of more deformed surfaces.

For example, to model the geometry of a structure resulting from two folding events, the axial surface (S_2) of the most recent fold (F_2) would be first modeled by interpolating field observations of the axial surface or associated foliation. The orientation of the axial surface (S_1) of the older folding event (F_1) can then be constrained with respect to (S_2) using a description of the fold geometry for F_2 folds. This additional orientation constraint is in turn used for interpolating S_1 geometry and the process is finally repeated for S_0 . Locally the fold geometry is constrained using a global scalar field representing the angle between consecutive foliations, e.g. S_1 and S_2 .

The local orientation of the folded surfaces can be characterised using the local direction vectors (e_x , e_y and e_z) and two rotation angles. The fold axis rotation angle rotates e_y around e_z to give the orientation of the fold axis (L_i). The orientation of the folded foliation (S_{i-1}) is characterised by rotating the whole

fold frame around the fold axis L_i by the fold limb rotation angle. The fold axis and fold limb rotation angles are the most important aspect of the fold modeling workflow because they control the geometry of the folded surface. The orientation of the folded surfaces need to fulfill the following criteria. It should be as close to the observations of the folded foliation as possible. Where no orientation constraints exist, the geometry of the folded foliation should fit the most geologically reasonable estimate, for example a folded surfaces should continue to be defined by localised variations in curvature away from observations instead of becoming a smooth surface (Jessell et al., 2014).

3.3 Fold geostatistics

The fold axis (α_P) and the fold limb (α_L) rotation angles can be calculated for each observation of the folded foliation or lineation. Both α_P and α_L can range in value from -90° to 90° (e.g. Fig. 3.2) and are 0° when the folded structural element is parallel to the direction of the fold frame coordinate. The larger the absolute value of a fold rotation angle, the larger the angle between the folded structural element and the fold frame. The geometry of the folded surfaces can be extracted by analysing the fold rotation angles within the fold frame coordinates.

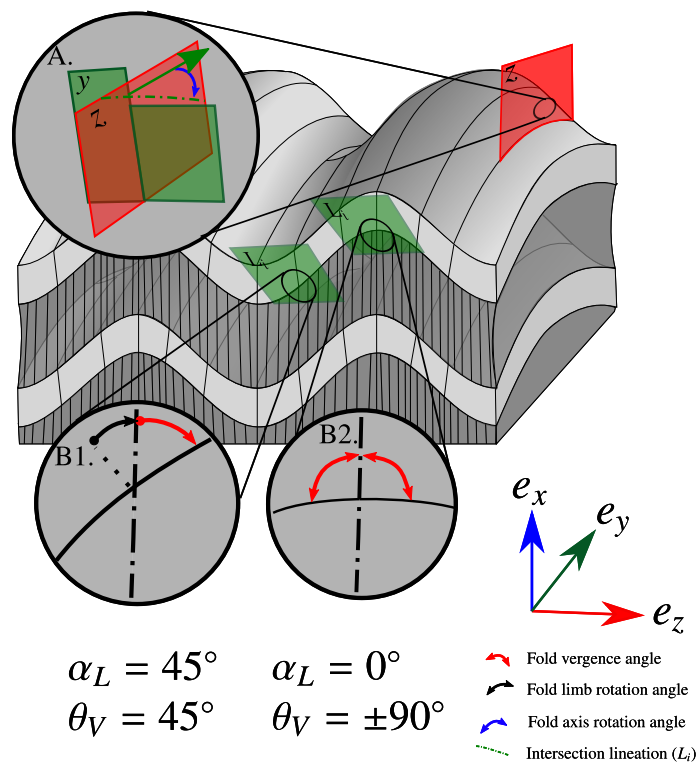


Figure 3.2: Schematic fold sketch showing: A: Fold axis rotation angle is the angle between the lineation L_i defining the local fold axis and e_y . B1: The fold limb rotation angle α_L is the angle between the normal to the folded foliation and the axial foliation, and is the complementary angle to fold vergence θ_V . The fold limb rotation angle is 0° in the hinge of the fold (B2) and can reach -90° or 90° in the limbs of a isoclinal fold.

3.3.1 Fold axis rotation angle

The fold axis rotation angle (α_P) is the angle between observations of the fold axis L_i and e_y (Fig. 3.2A) α_P is equivalent to the pitch of the fold axis in the axial surface of the fold if e_y is horizontal. The fold

axis is usually defined by field observations of the intersection lineation between the axial foliation and the folded foliation or by directly observing the hinge of a fold. To supplement these observations, which are often too sparse to characterise the geometry of the fold axis, we suggest to first interpolate the z coordinate of the fold frame that represents the axial foliation (S_{i-1}) from available foliation observations. This interpolation makes sense as these cleavage directions, which are more or less parallel to the fold axial surfaces, are generally smoother than the fold foliation (S_i). Even in the presence of cleavage refraction (Treagus, 1983), the intersection of this foliation field (S_{i-1}) with the folded foliation measurements (S_i) locally defines the fold axis. A fold axis rotation angle of 0° means that the fold axis is parallel to e_y . For example, this would occur, in the peaks and troughs of a type 1 interference pattern. A cylindrical fold will have a constant α_P throughout the model, normally 0° .

3.3.2 Fold limb rotation angle

The fold limb rotation angle (α_L) is the complementary angle to structural vergence. α_L is calculated by finding the complementary angle between e_z and the normal to observations of the folded foliation (S_{i-1}) in the plane perpendicular to the fold axis (L_i) (Fig. 3.2B). For example an α_L value of 0° indicates the location of the fold hinge (Fig. 3.2B). The sign of α_L in the limbs of the fold is dependent on the e_z direction.

3.3.3 S-Plot for analysing fold profiles

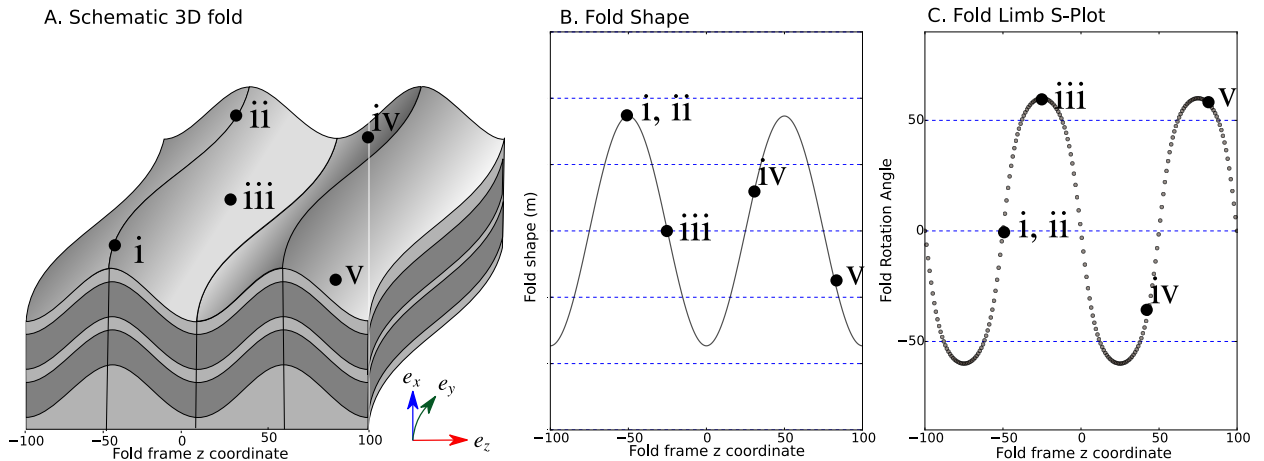


Figure 3.3: A: 3D diagram showing folded surfaces with a deformed axial surface. *i* and *ii* are locations along the same fold hinge along the axial surface. *iii* corresponds to the point of inflection in one fold limb. *iv* and *v* are points on either limb of an antiform with a large Euclidean distance between them. B: Synthetic fold profiles representing the shape of the fold in the fold frame. The key locations in (A) are indicated in the fold profile. C: S-Plot showing fold rotation angle profile for the fold in (A) with the key locations indicated on the S-Plot. *i* and *iv* are closer in the fold frame coordinate than in Euclidean distance.

The S-Plot is a cross plot of either α_P or α_L , and the associated fold frame coordinate. α_P is plotted against the y coordinate, and α_L is plotted against the z coordinate. The S-Plot allows for the characterisation of the effect of the younger deformation event on the geometry of the older structural feature independent of overprinting deformational events.

Fig. 3.3A shows a series of folded units with deformed axial surfaces. Fig. 3.3B is the fold shape viewed along the fold axis. Fig. 3.3C is the corresponding S-Plot to the 3D fold showing α_L plotted against the z coordinate of the fold frame. In this case, the fold frame is folded, however the effects of that folding have no impact on the S-Plot for the older folding event. Because the S-Plot uses the fold frame coordinates,

points are considered based on their location within the structure, *e.g.* the points i and ii in Fig. 3.3 are found on the same fold hinge (Fig. 3.3A) and occur at the same axial foliation scalar field value on the S-Plot (Fig. 3.3C). The S-Plot can be subdivided into three segments based on fold geometry: positive values of fold rotation angle characterise a fold limb (*e.g.* Fig. 3.3iii), negative values characterise an opposing fold limb (*e.g.* Fig. 3.3iv) and the location where the fold profile crosses 0 correspond to the fold hinge (*e.g.* Fig. 3.3i, ii).

The fold wavelength (distance in the z coordinate of the fold frame for α_L) can be identified by finding the location of two fold hinges and can be characterised for each fold closure independently. Synforms and antiforms can be differentiated by looking at the sign of the gradient of the fold profile for the hinge location. The sign of the rotation angle is dependent on the location chosen as the origin for the fold frame coordinates and on the polarity of the fold frame scalar field. When using scalar field interpolation algorithms (Calcagno et al., 2008; Cowan et al., 2003; Frank et al., 2007; Hillier et al., 2014; Mallet, 2002) this can be controlled by specifying a normal constraint.

3.3.4 S-Variogram for analysing spatial correlation

Although folding results in rapid variations in the orientation of the folded surfaces, it also introduces structure into the spatial distribution of orientations. As a result of folding, two points that are close together will generally have similar orientations and pairs of points sampled in opposing limbs will systematically exhibit large variations. For periodical structures, points sampled at a distance close to any multiple of the fold wavelength will have a similar orientation. The spatial evolution of variability can be quantified using a sample semi-variogram (Chilès and Delfiner, 2008, p. 34), which plot the mean-squared-variance between pairs of points separated by a distance h . Such statistical tools are commonly used in geostatistics because they provide insight into spatial variability without requiring assumptions about the mean of the property being sampled (Chilès and Delfiner, 2008, p. 32).

Folded surfaces generally exhibit a strong anisotropy in the orientation of the surface relative to the structural elements of the fold (fold axis and axial surface). Changes of orientation are statistically smaller for pairs of points aligned along the axial foliation and higher for pairs of points aligned orthogonal to the axial foliation. Such anisotropy can be revealed by considering only pairs of points aligned in a specified direction.

Gumiaux et al. (2003) successfully apply this strategy for identifying trend in a fold series. The variogram value reaches local maximum values where the points are separated by half a wavelength present in the fold trend, and reaches a local minimum where the points are separated by a wavelength of the fold. A variogram calculated along the axial surface shows minimal changes in variance between the pairs.

The identification of a suitable coordinate system and direction of anisotropy is necessary for robustly characterising the fold wavelength. For example, a curvilinear distance defined by geological distances, *e.g.* down dip, along strike and across strike for measurements in folded beds (Chilès and Delfiner, 2008, p. 48). The fold frame coordinate system (Laurent et al., 2016) provides a suitable coordinate system for characterising the geometry of the fold, even in the case of overprinting deformations. The S-Variogram is a sample semi-variogram calculated on the fold axis or limb rotation angle using the associated fold frame coordinate, respectively y and z . The S-Variogram is defined as follows for a series of observations of fold

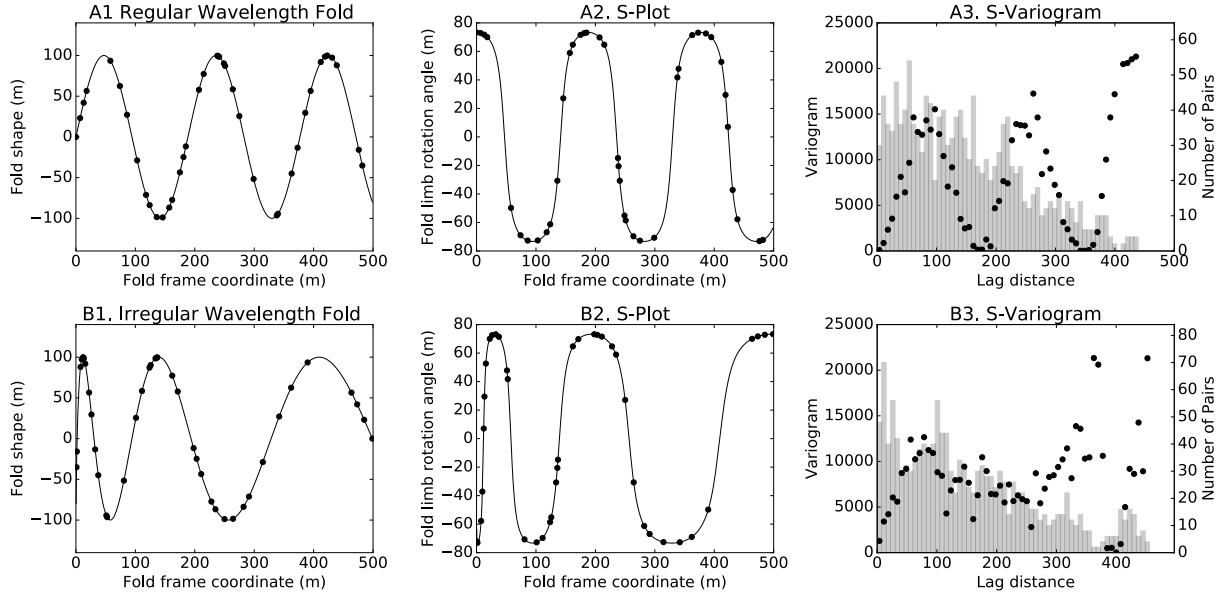


Figure 3.4: A1: Fold geometry with regular wavelength between adjacent fold hinges, black dots showing 40 random sampling locations. A2: S-Plot for fold in (A1). A3: S-Variogram calculated on sample locations showing periodic results. B1: Fold geometry of irregular wavelength fold with black dots showing 40 random sample locations. B2: S-Plot for fold in (B1). B3: S-Variogram for sample locations from (B1) with a subtle periodic trend.

rotation angles α_i at location z_i , with i ranging from 1 to the number of observations:

$$\gamma(h) = \frac{1}{|2N(h)|} \sum_{(i,j) \in (1,n)} |\alpha_i - \alpha_j|^2 \quad (3.1)$$

The lag distance h , is the distance between two data points in a pair, *e.g.* $|z_i - z_j|$. $N(h)$ is the number of pairs in the set. In practice a lag distance tolerance is generally applied ($h \approx |z_i - z_j|$) so that $N(h)$ is large enough to compute a reliable average. Each rotation angle is analysed using the associated fold frame coordinate. This means that the direction of anisotropy for the variogram is implicitly defined by the geometry of the fold frame.

The S-Variogram is used as an analytical tool to help characterise the fold geometries. If the experimental S-Variogram exhibits a periodical shape with a hole effect, the structural observations can be confidently interpreted as a fold train where the half wavelength between adjacent fold hinges is relatively regular Fig. 3.4A. In contrast, if the variogram does not show a periodical shape, there may be insufficient data for characterising the periodicity of the fold geometry or the fold may not have regular wavelengths between adjacent fold hinges (*e.g.* Fig. 3.4B). The S-Variogram provides a quantitative approach for analysing the fold geometry in terms of fold wavelength and periodicity, which are key fold characteristics. The location of the first local maximum on the S-Variogram will correspond to the shortest wavelength of the folding (where the folding has a regular wavelength). We propose using the gradient descent method (Cauchy, 1847) to identify this location by traversing the S-Variogram with increasing step sizes until the gradient to the nearest neighbour is negative. The gradient is estimated for each step distance by finding the best fit straight line to surrounding points. In most cases the data points will not be uniformly distributed throughout the fold frame, and the number of pairs for each lag distance may vary. If the local maximum for the variogram value is also a local minimum for the number of pairs, this estimate is not used. This methodology may also be used by varying the lag distance tolerance used to apply Eq. 3.1.

Choosing an appropriate step size for computing a sample variogram is not trivial and manual adjustments are often necessary in practice for obtaining good results. Here, we define a relatively robust strategy for making S-Variogram compatible with modeling without requiring too much user supervision. The proposed strategy is to choose a step size that is 20 percent larger than the average spacing between data points and a tolerance equal to the step size. This strategy yields reasonable results for the examples presented here and should apply to most structural data.

3.3.5 Synthetic examples

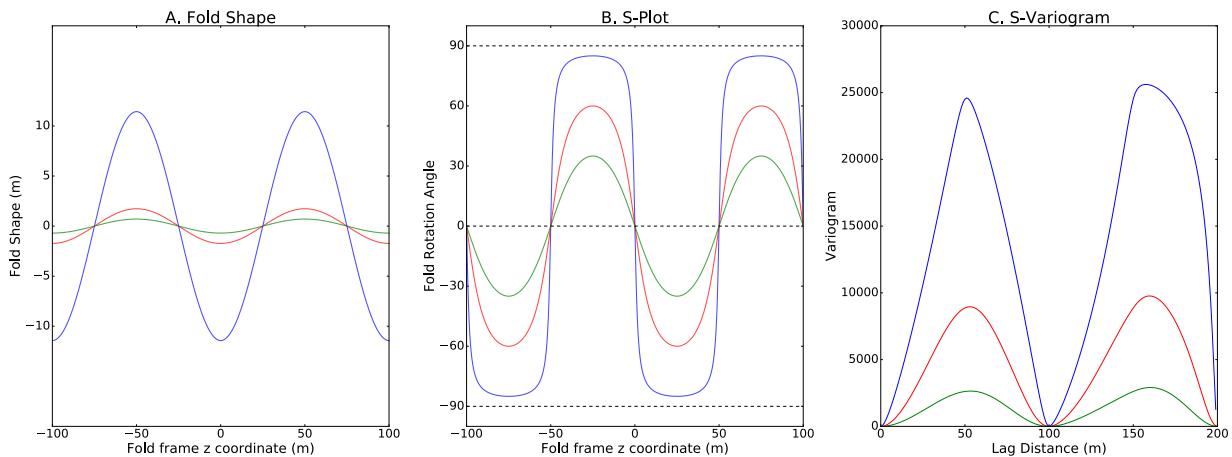


Figure 3.5: A: Three fold geometry viewed looking along the fold axis. Blue line represents fold with largest amplitude, red and green have decreasing amplitudes. The fold shapes all have a wavelength of 100m. B: S-Plot for the fold profiles in (A) the colour of the S-Plot curve corresponds to the associated fold shape in (A). C: S-Variogram for the fold shapes in (A) and the colour of the S-Variogram curve corresponds to the associated curves in (A) and (B).

In Fig. 3.5 three sinusoidal fold shapes of varying amplitude are shown. In these examples the fold wavelength has not been changed. As the amplitude of the fold increases, the tightness of the fold also increases. The folds range in tightness from blue (tightest), to red and green (most open). The tighter the fold, the steeper the gradient of the fold rotation angle where it crosses 0. This is consistent with structural geology observations where fold vergence will change quickly around the hinge when dealing with tighter folds. For isoclinal folds this will mean that identifying the locations of the fold hinges, or changes in fold vergence will be key to picking the appropriate fold geometry (which is usually the case in the field as well). This observation is also essential in the dip domains approach for modeling folds (Caumon et al., 2013; Fernandez et al., 2009).

Figure. 3.6 shows two different examples of asymmetrical folds that can be observed in the field. In Fig. 3.6A small scale folds occur within a larger scale antiform. The S-Plot showing the fold limb rotation angle for this example shows a series of small wavelength folds where the maximum and minimum rotation angles for the smaller scale fold decrease as the z coordinate increases. The change in these extreme values with increasing z coordinate represents the wavelength of the major antiform. The S-Variogram shows a periodic shape with the local maxima and minima representing the half wavelength and wavelength of the parasitic folds respectively. The S-Variogram can be used to robustly identify the half wavelength of the structure from irregularly spaced data for example in Fig. 3.4A.

A different type of asymmetrical fold can be observed in the field where the asymmetry is not associated with a larger scale folding event, or a folding event much larger than the study area. This could also be

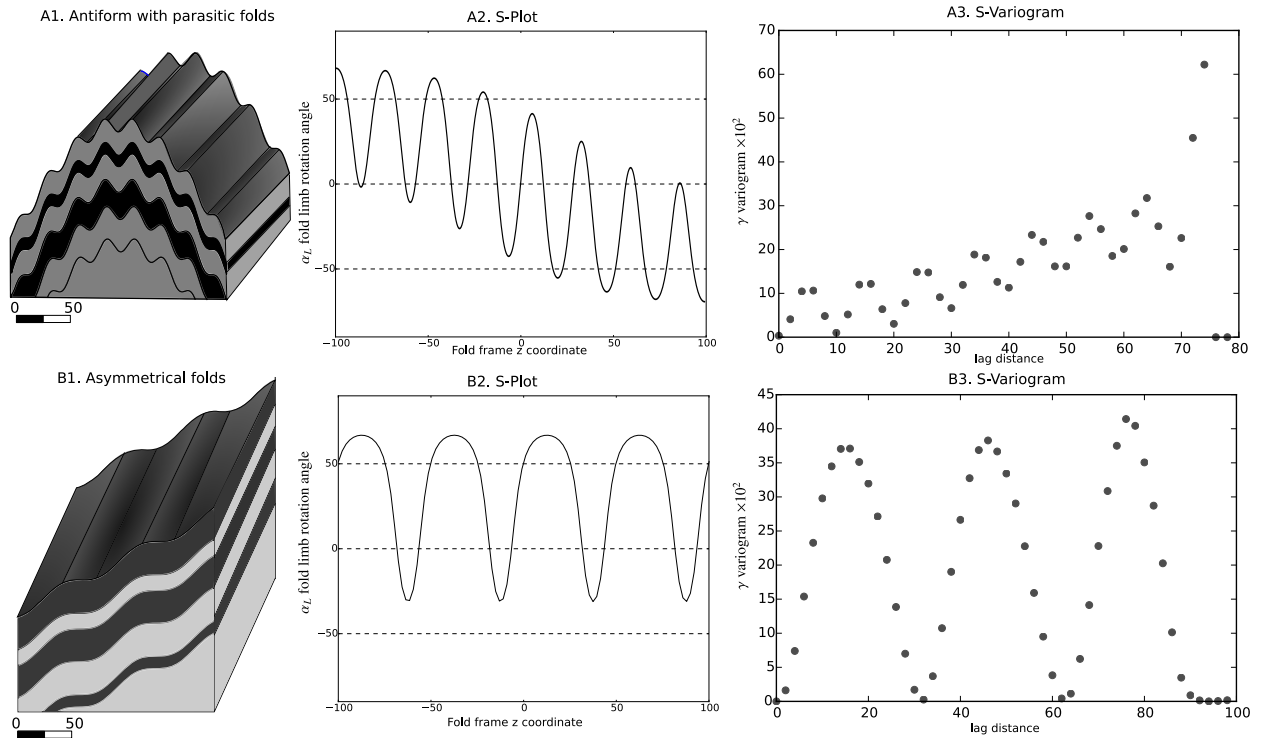


Figure 3.6: A1: Large scale antiform with smaller parasitic folds. A2: S-Plot for fold limb rotation angle. A3: S-Variogram of fold limb rotation angle. B1: Asymmetrical folds. B2: S-Plot for fold limb rotation angle. B3: S-Variogram of fold limb rotation angle

the result of the shortening direction of the fold not being orthogonal to the folded surface, for example when refolding a surface defined by a foliation. This type of asymmetrical fold and the associated S-Plot is shown in Fig. 3.6B. For each fold wavelength the features in the S-Plot for Fig. 3.6A and Fig. 3.6B are very similar. The maximum and minimum rotation angles remain constant for all folds in Fig. 3.6A.

3.4 Automatic fold modeling

The interpolation of the fold rotation angles is the most important stage of the structural modeling workflow proposed by Laurent et al. (2016) as the values of these rotation angles directly controls the orientation of the folded surfaces. The interpolation of angular data can be a complicated task and traditional statistical techniques are not necessarily applicable (Gumiaux et al., 2003). For example, the fold rotation angles must be between -90° and 90° . We interpolate the fold rotation angle by representing the fold rotation angles as $\hat{\alpha} = \tan \alpha$. This results in the interpolated fold rotation angle values not exceeding these boundary conditions.

To capture the complex geometries that are seen in natural folds, the fold profile needs to be interpolated directly from the available structural data. The fold rotation angles can be interpolated within the fold frame coordinate using any standard one-dimensional interpolation algorithms (*e.g.* Splines, Kriging, Radial Basis Functions). This approach will work well when the geometry of the fold is regularly sampled in the S-Plot. Where the model area extends away from outcrops then these methods will most likely fail to capture the fold style. For example the fold series in Fig. 3.7A has samples from two outcrops capturing the geometry of two fold hinges separated by three unobserved fold hinges. The S-Plot in Fig. 3.7B shows the fold rotation angle for the observations (black dots) and the resulting interpolation using standard interpolation

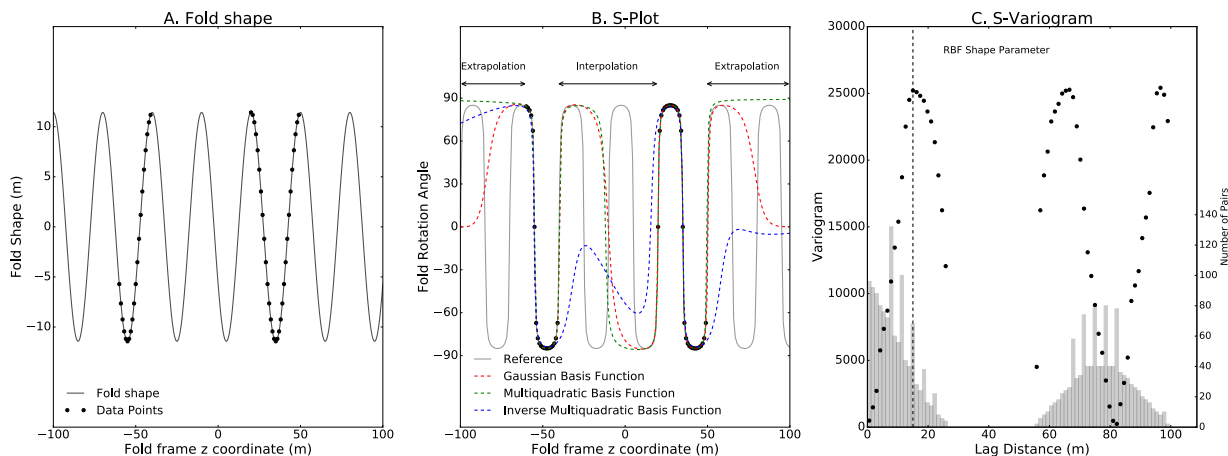


Figure 3.7: A: Synthetic fold train sampled from two outcrop localities. B: Interpolation and extrapolation of the fold rotation angle using different basis functions with Radial Basis Function interpolation. C: S-Variogram of fold rotation angle, the vertical dashed line represents the shape parameter used for the basis functions.

schemes. Three different basis functions, where the shape parameter is chosen to be the half wavelength of the fold (shown in Fig. 3.7C as the dashed line) are used for Radial Basis Function (RBF) interpolation. All three basis functions show similar results when interpolating within the half wavelength of the fold but generally deviate from the observed structural style when interpolating points further than a half wavelength from the nearest data point. This is because these methods tend to fit a smooth curve between structural observations and do not incorporate geological knowledge about the structural style of the folding (Jessell et al., 2014) (e.g. Fig. 3.7B).

To build a geologically reasonable estimation of the folding style the geologist will generally look at the surrounding structures, fold style and vergence to predict the location of fold closures. This process is difficult to quantify and undertake objectively. The basic assumption that can be used to predict the geometry of folds between outcrops is a continuation of the same shape folding. For example, in Fig. 3.7 there are two outcrop locations sampled from a simple sinusoidal fold train. The geologically reasonable estimation for the fold geometry would be to continue the same shape between the outcrops. Using the S-Variogram, the periodicity of the folding can be tested and where this assumption is valid (where a hole effect is observed) the periodicity of the folding can be modeled by finding the best fit Fourier series to the available dataset. If the folding cannot be modeled using a periodic model and the data sufficiently describes the fold geometry this can be interpolated using standard interpolation. Here, we use a one-dimensional RBF interpolation scheme.

3.4.1 Interpolating fold geometries using Radial Basis Functions

Radial Basis Function (RBF) interpolation is a commonly used method for interpolating spatial data. RBF methods are used to approximate multivariate functions from data in n -dimensional space for observations of the function value (Buhmann and Levesley, 2004). It is a widely accepted algorithm for interpolation in various scientific fields including applications to 3D geological modeling (Cowan et al., 2003; Hillier et al., 2014). The RBF interpolant can be used in any dimensions as the interpolant is a function of distance between the points. We use the RBF interpolation algorithm to interpolate the 1D fold rotation angle profiles. The value of either fold rotation angle for the relevant fold coordinate (z or y) is estimated using all observations of the fold rotation angle. A standard RBF interpolation approximates the unknown function,

using the weighted sum of N radial basis functions (ϕ) acting on the distance between the location being estimated x and the location of the observations x_i .

$$\hat{\alpha}(x) = \sum_{i=1}^N \omega_i \phi(\|x - x_i\|) \quad (3.2)$$

A number of different basis functions, with different interpolation properties exists. Generally the basis functions have two parameters: a shape parameter σ which is generally constant for all basis functions used in the interpolation and the distance between two points $r = \|x - x_i\|$. In this study we use a Gaussian basis function:

$$\phi(r) = e^{-\left(\frac{r}{\sigma}\right)^2} \quad (3.3)$$

The shape parameter for the RBF adjusts the area of influence for particular data points. It controls the distance up to which a data point will significantly influence the interpolated value. It is comparable to the range of a semi-variogram model used for kriging interpolation. To interpolate the fold rotation angle we choose to use the range of the S-Variogram as the shape parameter for the RBF interpolation. The RBF interpolant is only used to interpolate the fold rotation angles where no interpolated locations are more than a half wavelength from the nearest data point. This criterion is used because folding is periodic and after a half wavelength of the fold the correlation between pairs of points separated by a half wavelength of the fold should increase (where the variogram value decreases). As the distance between points increases, the interpolant places less weight on the surrounding points, effectively reducing the correlation between observations, this would result in interpolation artefacts such as in Fig. 3.7B where the interpolant fails to capture the folding style.

3.4.2 Extrapolating fold geometries using Fourier series approximation

Early work on fold shape analysis used a Fourier series approximation of the fold shape (Hudleston, 1973; Ramsay and Huber, 1987; Stabler, 1968; Stowe, 1988). The Fourier coefficients were optimized using least squares fitting of the coefficients for a known fold wavelength. This approach is suitable for analysing and representing the geometry of a single observable horizon looking along the fold axis. We propose using a Fourier series representation of the fold rotation angles to represent both the fold axis and fold limb rotation angles.

The Fourier series is a combination of trigonometric functions that can be used for approximating a periodic function. In its standard form the Fourier series is:

$$\hat{\alpha}(x) = A_0 + \sum_{k=1}^{\infty} A_k \cos \frac{k\pi x}{\lambda} + B_k \sin \frac{k\pi x}{\lambda} \quad (3.4)$$

where the Fourier coefficients A_k, B_k , represent the contribution of each frequency to the function being approximated. λ represents the wavelength of the fundamental frequency of the periodic function being estimated. The wavelength of the fold can be automatically identified from the S-Variogram.

The values for a finite number of Fourier coefficients can be solved using least squares. To ensure that a solution can be found there needs to be a greater or equal number of data points to the number of coefficients being estimated. The coefficients $A_0, A_1, B_1, \dots, A_k, B_k$ can then be used in the Fourier series (Eq. 3.4) to interpolate the fold rotation angle for any value of the fold frame scalar field.

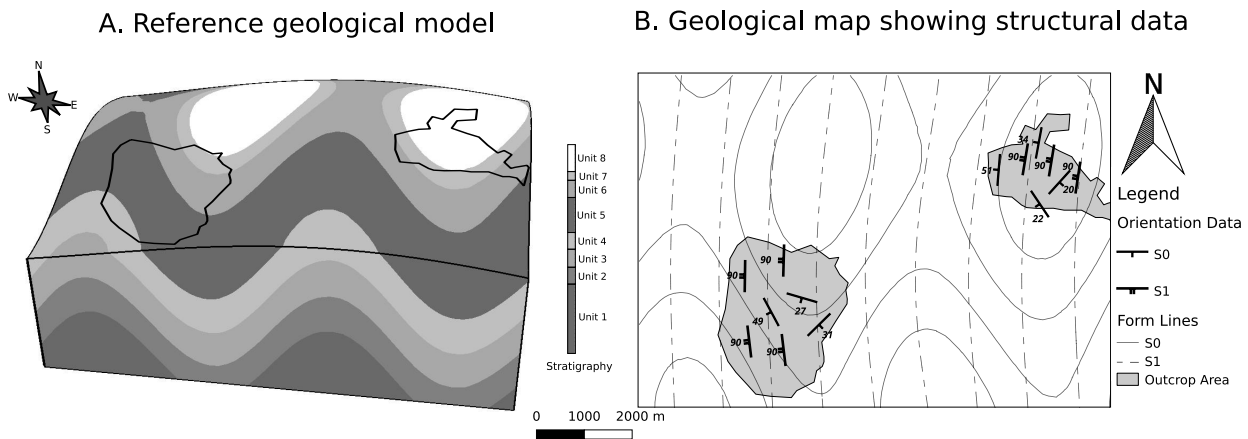


Figure 3.8: A: Reference model of doubly plunging fold showing outcrop locations. B: Geological map showing outcrop locations with structural data and bedding form lines for model area.

The number of coefficients used controls the complexity of the fold geometry that is modelled. Irregular sampling, ambiguity and uncertainty in the structural observations can result in an overfitted Fourier series curve if too many coefficients are chosen. The interpolated fold rotation angle curve needs to be locally smooth while still describing the underlying fold shape. One way to control the resulting profile is to optimize the number of coefficients using a regularization approach with an objective function that assesses the required criteria. An alternative approach is to filter the noise from the data prior to fitting the Fourier series. To address irregular sampling which is problematic in Fourier analysis (Chilès and Delfiner, 2008, page 57), we propose using the RBF interpolation scheme prior to fitting the Fourier series where the interpolation is performed only on data points separated by less than the half wavelength of the fold.

3.5 Case studies

3.5.1 Proof of concept: synthetic fold

Fig. 3.8A is a doubly plunging fold series generated in Noddy (Jessell and Valenta, 1996) using the python interface, pynoddy (Wellmann et al., 2016). Two outcrops are used for sampling structural observations both located in fold hinges. The main folding (associated with S_1 axial foliation observations) in the reference model has a wavelength of $5000m$ and an amplitude of $1000m$. The doubly plunging effect is created by super imposing a second folding event with an axial surface perpendicular to the main folds axial surface creating a Type 1 fold interference pattern. Orientation measurements representing the orientation of the axial foliation (S_1) and the folded bedding surface (S_0) are shown on the geological map (Fig. 3.8B). The form lines shown on the geological map are not used to create the geological model and are only shown for highlighting the reference geometry. The axial surface of the fold train has a curvilinear geometry which can be seen by the subtle change in strike of S_1 in the northern outcrop. The z coordinate of the fold frame is modelled using observations of S_1 (Fig. 3.9D). The interpolated z coordinate captures the curvilinear geometry of the axial surface in the reference model. The y coordinate is modelled using the constraints that e_y is orthogonal to e_z and is horizontal ensuring a unique solution for the scalar field (Fig. 3.9A). The intersection lineation is locally calculated by finding the intersection between S_0 and the isosurfaces of the interpolated z coordinate scalar field. The fold axis rotation angle is calculated by finding the angle between the intersection lineation and e_y in the plane perpendicular to e_z . The S-Variogram for the fold axis rotation

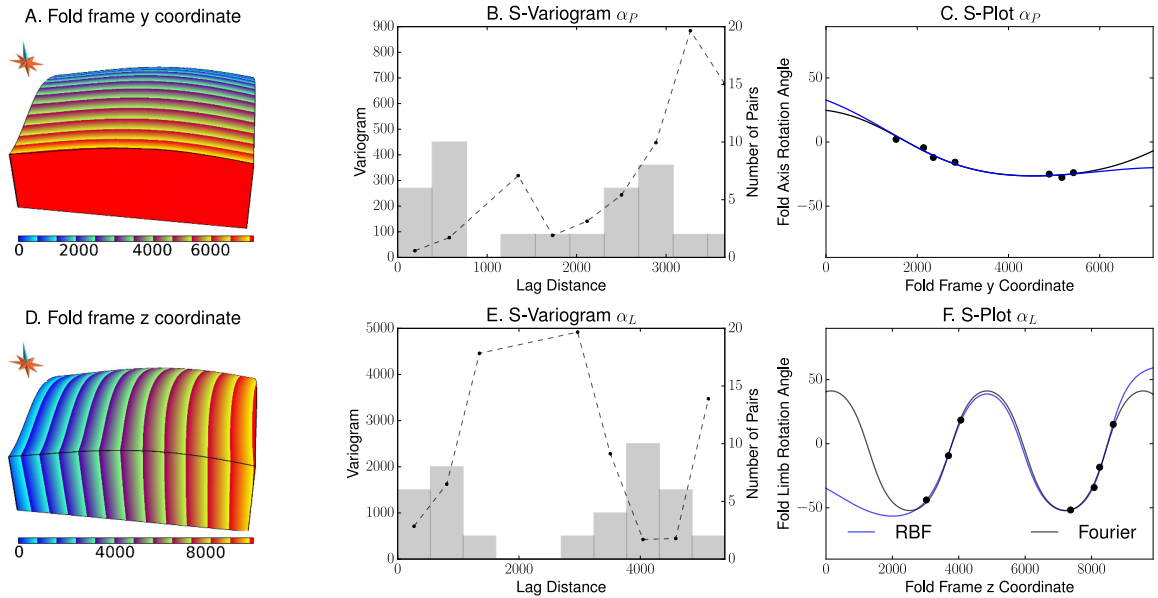


Figure 3.9: A: Interpolated y coordinate scalar field. B: S-Variogram of α_P with a step distance of 300m. C: S-Plot of α_P and y showing the fold profile interpolated using an RBF interpolant (blue curve) and Fourier series (black curve). D: Interpolated z coordinate scalar field. E: S-Variogram of α_L with a step distance of 500m. F: S-Plot of α_L and z and interpolated fold profile using an RBF interpolant (blue curve) and Fourier series (black curve).

angle can be seen in Fig. 3.9B. The number of pairs for each lag distance shows a significant drop between 1000m and 2000m. This indicates there are not enough pairs of points in these locations to robustly estimate the variogram value. In order to avoid identifying the incorrect wavelength the number of pairs can be used to validate the identification of a local maximum. If the identified local maximum also corresponds with a local minimum in the number of pairs (such as seen at a lag distance of 1000m in Fig. 3.9B) this wavelength estimate is discarded. In this example the variogram value continues to increase at larger lag distances and neither a hole or sill effect can be observed. This suggest that the orientation data does not sample more than the fold half wavelength. In this case it is not possible to determine whether the folding has a regular wavelength distance or if the estimated wavelength is a true estimate of the fold wavelength.

We use the maximum lag distance of 3780m for the S-Variogram as the RBF shape parameter. In this case the fold axis rotation angle only needs to be extrapolated a maximum of 1700m away from the nearest data point. Fig. 3.9C shows the fold axis rotation angle calculated for the structural observations that are marked by black dots, the interpolated fold axis rotation angle profile inferred with a RBF interpolant (blue line) and using the Fourier series (black line). The interpolated profile is shown for the range of y coordinate values in the model space (Fig. 3.9A). The two interpolation methods produce very similar results because minimal extrapolation is required. If the model area were extended further in the north (or south) then the difference between the two interpolation methods would be exaggerated. However, because the S-Variogram does not show a sill or hole effect, it is not possible to determine a good estimate for the fold wavelength. In these cases the wavelength may need to be refined by the geologist, or additional data must be collected to better constrain the geometry of the folding.

The fold axis is defined throughout the model space by locally rotating e_y around e_z using the interpolated fold axis rotation angle for the y coordinate values. The fold limb rotation angle is calculated by finding the angle between the normal to the bedding orientation (S_0) and e_y in the plane perpendicular to the interpolated fold axis. Fig. 3.9E shows the S-Variogram for the fold limb rotation angle in the z coordi-

nate, with a histogram representing the number of pairs of points for lag distance. The number of pairs is irregular with a low number of pairs occurring between 1500m and 3500m. These lag distances are greater than the maximum distance within an outcrop and less than the distance between outcrops (Fig. 3.8B). There is a higher number of pairs at a lag distance greater than 4000m correlating with a hole effect for the S-Variogram. A local maximum for the S-Variogram value is seen for a lag of 3000m, however this variogram value is also surrounded by lag distances with no data pairs. This suggests that the half wavelength of the fold is between 1500m and 3000m which is consistent with the reference model fold wavelength of 5000m. If the folding is symmetrical and has a regular wavelength between fold hinges a hole effect should be observed at a lag distance equal to the fold wavelength. In this case a hole effect is seen at 4000m with a local minimum occurring at 4500m. The hole effect seen at $\sim 4000m$ is consistent for step distances between 200m and 700m, the step distance in Fig. 3.9E is equal to the average nearest neighbour of $\sim 450m$. Small variations in the estimated wavelength for different variogram step distances could be used to explore geological uncertainty associated with the fold geometry.

The S-Plot of the fold limb rotation angle (Fig. 3.9F) shows two populations of data points that correspond to the locations of the outcrops in Fig. 3.8B. To interpolate the fold rotation angle profile using the RBF interpolation scheme, we specify the shape parameter for the basis function as the half wavelength of the fold (2250m) and interpolate between the outcrop edges. The resulting interpolation using the RBF is shown in Fig. 3.9F using the blue curve and the Fourier series profile is shown by the black curve. The Fourier series is fitted to the RBF interpolated profile for the range of z coordinate values for the data points (between 3000m and 8300m). The main differences between the two interpolated profiles occurs where the fold geometry needs to be extrapolated. The Fourier series fold limb rotation angle curve continues the same structural style as observed in the outcrops. The RBF interpolation misses the fold hinge at $z = 1800m$, which roughly corresponds with the western fold hinge in the reference model. In the eastern area of the model, less extrapolation is required and the differences between the interpolated fold rotation angle values is minimal and will not significantly impact the model geometries.

Each fold limb rotation angle profile will result in a different set of constraints for implicit modeling of the folded surfaces. The orientation of the folded surfaces are constrained by rotating the fold frame around the fold axis by the fold limb rotation angle. Using these constraints and the orientation observations of bedding from Fig. 3.8B, the model (S_0) is interpolated using Discrete Smooth Interpolation (DSI) (Frank et al., 2007; Laurent et al., 2016; Mallet, 2002). The resulting model for both rotation angles being interpolated using the RBF scheme is shown in Fig. 3.10C. Fig. 3.10B is the resulting model interpolated using the Fourier series scheme for both rotation angles. The scalar field values of the interpolated models are constrained using a single data point in the north eastern outcrop. Both models deviate from the reference model in the western area due to the minimal value constraints used. This is intentional because the value constraints are integrated into the implicit scheme as equality constraints and if too many are used they can introduce significant geometrical artefacts. This problem could be solved using inequality constraints (Frank et al., 2007; Hillier et al., 2014) to constrain outcrop lithologies using a range of scalar field values rather than a single value or using the iterative process suggested by Collon et al. (2016).

Unit 5 is a good marker horizon for comparing the fold geometries. In the reference model (Fig. 3.10A) two antiforms can be seen and the north western area of the model shows a saddle structure. The Fourier series model Fig. 3.10B captures both antiforms, however the western antiform hinge location is shifted to the west. The saddle structure does not outcrop, however the geometry of the interpolated surfaces do

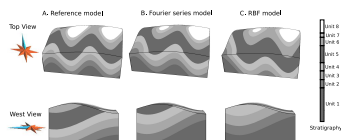


Figure 3.10: A: Reference model looking from the top and from the west. B: Model interpolated using Fourier series for fold axis and limb rotation angles looking from the top and the west. C: Model interpolated using RBF series for fold axis and limb rotation angles looking from the top and the west.

capture this geometry. The difference in map pattern is most likely the result of the limited constraints used for the scalar field values because the dome structure is seen to the east of this antiform. The model interpolated with the RBF interpolant (Fig. 3.10C) only captures a single antiform. Along the axial surface the fold geometry of the two interpolated models and the reference model are very similar, all showing a non-cylindrical fold axis. The interpolated models have a fold axis that has been folded by a shorter wavelength fold ($7560m$) than the reference model ($13055m$). This is consistent with the S-Variogram analysis where it was not possible to confidently estimate the fold wavelength. Both interpolated models capture the main fold geometry in the areas constrained by observations. The model interpolated from the using RBF interpolant does not capture the structural style away from observations and misses the continuation of the fold train. The Fourier series model captures the structural style of the reference model, however there are some variations in the outcropping geometry and location of fold hinges. These differences are due to a combination of the sparse data and the location of samples relative to the fold geometry collected from the reference model.

3.5.2 Implicit modeling of Cape Conran, Victoria

Finally, we present an application of the fold geostatistics and fold modeling (Laurent et al., 2016) to a case study from Cape Conran in the Palaeozoic Lachlan Fold belt, Eastern Victoria, Australia (Fig. 3.11A). The outcrop (location shown in Fig. 3.11B and a schematic structural map in C) is an asymmetric fold of a turbiditic sequence found in the limb of a larger antiform (Burg and Wilson, 1988). There is a degree of disharmony in the fold geometries across different layers (mudstone and sandstone) of varying competency and thickness. We use field observations of the axial surfaces of folds (Fig. 3.11C, S_1) to interpolate the

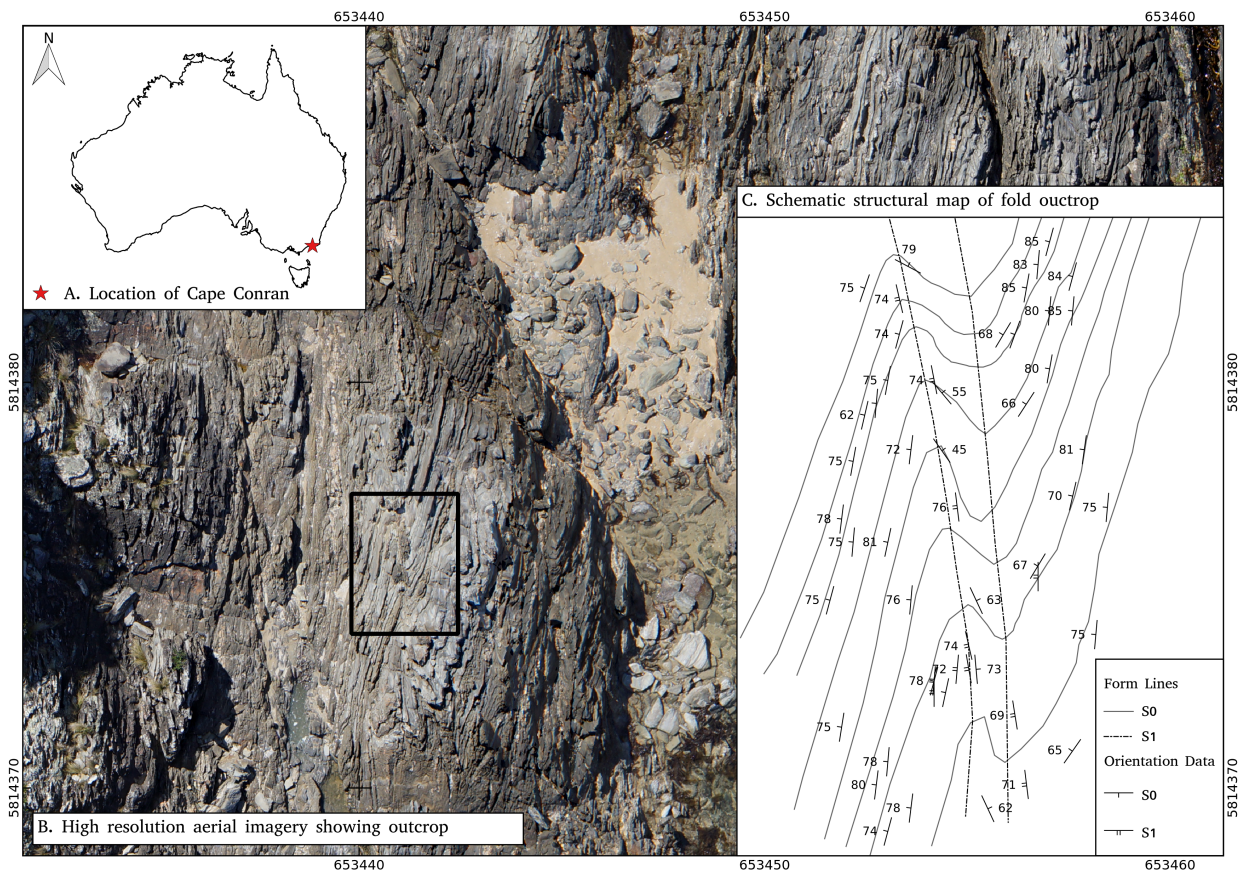


Figure 3.11: A: Location of Cape Conran in the Palaeozoic Lachlan Fold belt, Eastern Victoria, Australia GDA94 zone 54. B: Aerial photograph of rock platform depicting folded turbidite packages. C: Schematic structural map of outcrop used in this study.

z coordinate of the fold frame. The orientation of bedding (S_0), is representative of the folded sandstone layers and was collected in the field (Fig. 3.11C). The form lines shown in Fig. 3.11C show the interpreted structure from aerial imagery and the collected field observations. In this example, the form lines are not used in the modeling scheme and the geometrical model is based entirely on the orientation observations.

The scalar field representing the z coordinate of the fold frame is interpolated using Discrete Smooth Interpolation (DSI) (Frank et al., 2007; Mallet, 2002) on the field observations (S_1 in Fig. 3.11C). To ensure a unique solution, the normals to the (S_1) foliation are all directed towards the east, imposing an eastward growing scalar field. The scalar field is shown in Fig. 3.12D and appears to conform well with the data and the geometry of the interpreted S_1 form lines. The fold axis is represented by the average direction of the intersection between observations of bedding and e_z , plunging 53° towards 356° . The fold limb rotation angle is calculated as the angle between field measurements of bedding S_0 and e_z in the plane perpendicular to the fold axis. The S-Variogram of the fold limb rotation angle is shown in Fig. 3.12A. The lag distance for the variogram is equal to the average nearest neighbour distance and the number of pairs (indicated by the histogram) decreases with increasing step distance. The S-Variogram reaches a maximum value at approximately $0.57m$ and shows a hole effect at a lag distance of $0.7m$. The fold wavelength can be estimated to be $1.14m$. The discrepancy between the hole location and the wavelength estimate is most likely the result of the fold asymmetry and suggests that there is a difference between the length of the short limb wavelength and the long limb wavelengths. This is also the cause of the low variogram values from $0.7m$ to $1.3m$.

The geometry of the fold can be extracted using the S-Plot Fig. 3.12B and C. The negative values of the fold limb rotation angle correspond to the longer limbs of the fold and the positive values the shorter limbs. The fold limb rotation angle data points show an asymmetrical shaped fold with a larger absolute value for maximum fold limb rotation angle for the longer limb. These characteristics are very similar to the pattern observed in the asymmetrical fold in Fig. 3.6B.

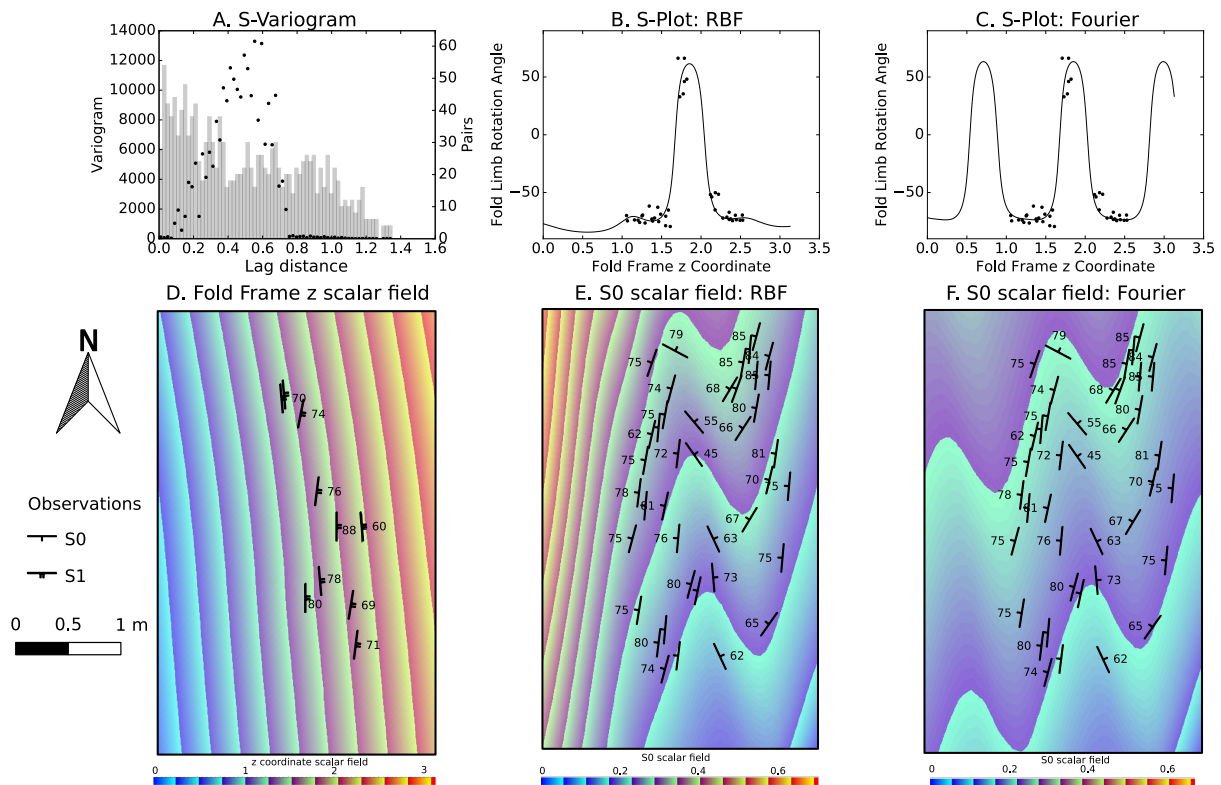


Figure 3.12: A: S-Variogram of fold limb rotation angle. B: S-Plot with RBF interpolated fold rotation angle curve. C: S-Plot with Fourier series fold rotation angle curve. D: Scalar field representing the fold frame z coordinate viewed from above. E: Scalar field representing bedding using the fold geometry constrained using the RBF curve viewed from above. F: Scalar field representing bedding using the fold geometry constrained by the Fourier series curve viewed from above.

Fig. 3.12B shows the fold limb rotation angle interpolated using RBF interpolation with a shape parameter of $0.57m$. In the areas where the fold rotation angle is extrapolated away from the observations the interpolation is biased towards the long limb of the fold (where the majority of observations occur). The resulting interpolated geometry captures the observed fold hinge well. However, away from the observations, there are no additional folds and the model continues with the same geometry as the long limb of the fold. Given the input structural observations (Fig. 3.11B) where the folding is asymmetrical and there are no mapped structures that suggest the fold is not a part of a fold series, this model is probably not the most geologically reasonable approximation.

The Fourier series representation of the fold rotation angle (Fig. 3.12C) uses the estimated wavelength of the fold ($1.14m$) to create a regular periodical representation of the fold geometry. The Fourier series uses the fold geometry captured by the RBF interpolation of the data points within the outcrop to produce a continuation of the same structural style away from the outcrop. The resulting model fits the structural observations well and continues the same structural style away from the outcrop with an additional antiform to the east and a synform and antiform to the west.

In this example only a single short limb is captured by the structural observations making it difficult

to determine from the data whether the asymmetrical fold is a parasitic fold associated with a larger wavelength fold (Fig. 3.6A) or whether the folding is asymmetrical folding unrelated to larger scale fold. In this case, regional context suggests that the asymmetrical folding is associated with a large antiform closing to the east of the model area (Burg and Wilson, 1988).

3.6 Discussion

Laurent et al. (2016) introduce a framework for modeling folds where the structural elements of folds (fold axes, axial foliation) and two rotation angles are used to define the orientation of the folded surface everywhere in the model. The use of this frame allows to simplify 3D fold analysis by considering variations along two one-dimensional profiles. This method is suitable to non-cylindrical structures, assuming the main shortening axis can be reliably obtained from the foliation associated to folding. In Laurent et al. (2016), the fold rotation angles are defined by estimating the geometry of the fold using a trial and error approach and fitting a modified sinusoidal fold geometry. In this contribution, we have addressed the main limitation in the method by using a data driven method for characterising and interpolating the fold rotation angles. We introduce two plots that allow for the geometry of the folds to be extracted from the available structural observations. The S-Plot shows the fold shape when looking down plunge of the fold and the fold axis rotation angle provides information about the non-cylindricity of folding. The S-Variogram is used to test whether the fold wavelength is regular between observed fold hinges, and to estimate the dominant wavelength. These tools could be used during field mapping by the structural geologist to help understand the geometries of the structures being mapped and predict where more information is needed to characterise fold geometries.

The modified sinusoidal fold profile addresses two issues with classical implicit interpolation schemes highlighted by Jessell et al. (2014): (1) the inability to interpolate or extrapolate fold series with continuous structural style; (2) the shape of fold hinges are not being controlled (and often being smoothed). In this contribution we directly interpolate the observed fold rotation angles to produce a model-wide representation of the fold rotation angles. The fold geostatistics are used to determine the appropriate interpolation method and the associated parameters for interpolation/extrapolation. The fold hinge geometry is characterised by the slope of the fold rotation angle curve at the hinge locations and is determined by the structural observations for each hinge where available or by extrapolating the geometry of the observed fold hinges. We believe this is advantageous because it is a data driven approach and the tightness of each observed fold hinge can be independently controlled by the structural observations.

In both Fig. 3.10 and Fig. 3.12, the fold geometries characterised using the Fourier series and the RBF interpolant are significantly different. The main differences between the resulting models are where extrapolation is required. In Fig. 3.12 the Fourier series model predicts a regular repetition of fold hinges away from the observations. The Fourier series model is based on the geometry of the observed single parasitic fold meaning the long limb distance between synform and antiform (measured in the z coordinate) is interpreted to be the same as the short limb distance. Without observing more fold hinges it is difficult to confidently constrain the appropriate wavelength value to use. However, the most geological reasonable estimation of the structure given the available data is to continue the same structural style. If more data is collected, for example sampling another fold hinge at Cape Conran, the model can be updated using additional data.

The outcrop at Cape Conran has a high density of structural observations that capture the disharmony in the folding between the different sandstone layers. At the regional scale it is unlikely that enough structural observations and outcrops will be present to capture disharmony in folding. There are other sources for noise and uncertainty in the structural observations such as: geological uncertainty and ambiguity in observations and interpretations (Bond et al., 2007a,b; Jessell et al., 2010; Lindsay et al., 2012; Wellmann and Regenauer-Lieb, 2012; Wellmann et al., 2010). Noise and irregular data sampling can add complexity to the model fitting process. Data points are evenly weighted and collocated data points can significantly skew the resulting model to a particular feature that may not be associated with the fold geometry. The use of the RBF interpolation prior to fitting the Fourier series model provides a suitable approach for filtering out the noise and uncertainty. The half wavelength of the fold is used to constrain the shape parameter for the basis functions. This will remove noise and ambiguity from the observed data for the model fitting without smoothing out the information associated with the folding.

The linear regression used to find the best fit Fourier series requires the largest fold wavelength to be known. This is identified by finding the range of the S-Variogram using the gradient descent method. The Fourier coefficients are optimised to find the best fit Fourier series for the given base wavelength. If the wavelength is underestimated, then the largest wavelength of the fold cannot be modeled. In contrast, if the wavelength is too large the extrapolated fold geometries may not be geologically reasonable. While the method is generally adequate for finding the best fit Fourier series, it may fail in the cases, where there is additional noise or where the half wavelength of the fold is not visible in the S-Variogram. In these cases, the wavelength could be specified by the geologist and refined to fit the observations. As shown in Fig. 3.9E the S-Variogram is limited by the spatial distribution of the structural observations. If there are not enough observations separated by the fold half wavelength, it is not possible to confidently estimate the half wavelength of the fold. Another limitation in this method is the resolution of the wavelength estimate will be dependent on the step distance of the S-Variogram. It would be beneficial to optimise the wavelength parameter as well as the Fourier coefficients, using a non-linear least squares approach.

A single best fit model was produced for the observed structural data. In Fig. 3.12 the range in the fold rotation angles for the long limb of the fold is $\pm 15^\circ$. A single fold rotation angle curve cannot represent the range in possible fold geometries that could be fitted to these observations. Preliminary work using Bayesian inference to solve the Fourier series regression has provided promising results providing a range in possible fold geometries that could be fitted to the structural observations.

3.7 Conclusion

In this contribution we have expanded the capabilities of the fold modeling framework presented in Laurent et al. (2016) by using structural data to directly inform the modeled fold geometry. Two main contributions to geological modeling and structural geology are presented in this paper:

- The fold geostatistic (S-Plot and S-Variogram) allow for the geometry of folds to be characterised directly from the field structural observations.
- The representation of the fold geometry using a Fourier series fitted to the structural observations produces a geologically reasonable extrapolation of the fold shape.

We have demonstrated an application of these tools to fold modeling with a proof of concept synthetic model and a more complicated asymmetrical fold from the Cape Conran, Victoria. We have primarily fo-

cused on the application of the fold geostatistics for geometrical modeling, however we also expect that these tools can be applied for structural analysis of folds. The representation of the fold geometry using a Fourier series has provided more flexibility in the possible fold geometry, allowing for a complex asymmetrical fold to be modeled, which was not possible using the previous methodology. Further developments are required to incorporate structural uncertainties into this work flow.

Acknowledgements

The authors would like to thank Peter Hudleston and an anonymous reviewer for their comments that significantly improved this manuscript. This research was partially funded by Australian Research Council Discovery grant DP110102531 and Australian Research Council Linkage grant LP140100267. Part of this work was performed in the framework of the “Investissements d’avenir” Labex RESSOURCES21 (ANR-10-LABX-21) and of the RING project at Université de Lorraine. The authors are grateful to the industrial and academic sponsors of the Gocad Research Consortium managed by ASGA (Association Scientifique pour la Géologie et ses Applications, <http://ring.georessources.univ-lorraine.fr/>) for their support. We thank Paradigm for providing the GOCAD-SKUA software and API. All of the models in this publication have been generated with the StructuralFactory plugin for Gocad, based on RING’s StructuralLab plugin. The synthetic dataset in Fig. 3.8 was generated using Noddy.

Chapter 4

Inversion of structural geology data for fold geometry

L. GROSE¹, G. LAURENT^{1 2}, L. AILLERES¹, R. ARMIT¹, M. JESSELL³, T. COUSIN-DECHENAUD²

¹School of Earth, Atmosphere and Environment, Monash University PO Box 28E, Victoria, Australia

²GeoRessources (UMR 7359), Université de Lorraine-ENSG, CNRS,CREGU
Campus Brabois, TSA 70605, 54518 Vandoeuvre-lès-Nancy Cedex, France

³The University of Western Australia, Centre for Exploration Targeting,
School of Earth and Environment, Perth, Western Australia, Australia

Submitted to Journal of Geophysical Research: Solid Earth on 7 November, 2017, manuscript number 2017JB015177

Review pending

Abstract

Recent developments in structural modeling techniques have dramatically increased the capability to incorporate complex fold related data into the modeling workflow. However, these techniques are lacking a mathematical framework for properly addressing structural uncertainties. Previous studies investigating structural uncertainties have focused on perturbing the input data as a way to analyse the sensitivity of the interpolator to the dataset. These approaches do not consider the contribution of the geological structures and interpolation process to the overall uncertainty. In this work, we frame structural modeling as an inverse problem and use a Bayesian framework to reconcile structural parameters and data uncertainties. Bayesian inference is applied for determining the posterior probability distribution of fold parameters given a set of structural observations and prior distributions based on general geological knowledge and regional observations. This approach allows for an inversion of structural geology data, where each realisation can differ in the structural description of the fold geometries, instead of finding only a single best fit solution. We show that analysing the set of resulting models with information entropy and a new metric quantifying the difference in the interpolated geometries highlights the areas with the highest uncertainty. These areas can be used to target where additional data would be most beneficial for improving the model quality and efficiently reducing structural uncertainty.

4.1 Introduction

Three dimensional geological models are a representation of the distribution and structural relationships between rock units in 3D space. They find practical applications throughout a wide range of geoscientific disciplines ranging from visualisation, interrogation, advanced analysis and process simulation. Three dimensional models are more difficult to create than a geological map because they require the prediction of geological structures at depth, which are difficult to constrain from surface observations. There are a range of different approaches where modeling methods: (1) almost exclusively use prior geological knowledge (Jessell, 1981; Jessell and Valenta, 1996), (2) a hybrid approach where geological knowledge is incorporated by adding some kinematic information and incorporated with direct observations (Bigi et al., 2013; Laurent et al., 2013, 2016; Moretti, 2008), and (3) other systems only using observations in 3D space. A common method for building 3D models is to only consider observations to create an *explicit* representation of the surface by either interpolating between data points or triangulating a surface directly from the data (Caumon et al., 2009; Mallet, 1992, 2002). Another framework for representing these surfaces is to use an *implicit* representation of the surface (Aug et al., 2005; Caumon et al., 2013; Cowan et al., 2003; Frank et al., 2007; Hillier et al., 2014; Lajaunie et al., 1997) where the geological surface(s) are represented as iso-values of a volumetric scalar field. All of these approaches create a single best fit model for the structural observations.

Folds have the potential to introduce dramatic complexity and uncertainty in the process of structural modeling. Even relatively gentle folded structures perturb the spatial correlation of structural information. For this reason, folds remain a challenge for the interpolation schemes at the basis of implicit structural modeling. To constrain the geometry of folds, the geologist is generally required to draw fold profiles on cross sections or level maps, using bedding orientations (Jessell et al., 2014, 2010; Maxelon et al., 2009). Additional foliations and lineations are generally overlooked and not directly used. In particular, it is not trivial to input the structural information recorded from field studies such as fold axial traces and their structural elements (fold axes, fold vergence and fold overprinting) into the implicit scheme (Jessell

et al., 2014). Laurent et al. (2016) incorporate these additional structural datasets by modeling all foliations starting from the most recent, modeling each preceding event accounting for the geometry of the younger foliation. With this approach, folds are embedded into a fold frame that represents the structural elements of the fold: axial surface, axis, and vergence. The geometry of each folding event can be derived from the available structural data using geostatistical analysis within the fold frame (Grose et al., 2017a). The geometry is characterised using the best fit Fourier series to the field observations using the maximum likelihood method. The characterisation of the fold geometry can be framed as an inverse problem where the aim is to determine the model parameters representing the observations. Using the maximum likelihood approach and finding a single solution to an inverse problem is usually not sufficient due to the complex multidimensional parameter space (Mosegaard and Tarantola, 1995). In general, an understanding of the associated uncertainty is usually required, for fold geometries the aim is to understand the distribution of possible fold shapes given the observed data and not to only find the single best fit fold geometry.

Previous approaches for sampling structural uncertainties have focused on either perturbing the input data (e.g. Jessell et al., 2010; Lindsay et al., 2012; Wellmann and Regenauer-Lieb, 2012) or perturbing reference model surfaces (e.g. Suzuki et al., 2008; Tacher et al., 2006; Thore et al., 2002). Neither of these approaches properly address the uncertainty in the description of the geological structures and interpolation process. In this contribution, we use the modeling framework of Laurent et al. (2016) and introduce a probabilistic representation of the fold geometry. The fold geometry is represented using a Fourier series where parameters constraining the wavelength and fold shape are represented by probability density functions (PDF). Each parameter is given a prior distribution containing the information that is known about the parameter, independent of the model that is being fitted. The prior distributions are constrained by a combination of additional data analysis, geological knowledge, and valid parameter ranges. The joint posterior distribution for the combined parameters is sampled using a Markov Chain Monte Carlo (MCMC) sampler. Using this system data uncertainty is represented using an uninformed prior PDF (no information about the data uncertainty is included in the sampling). We demonstrate the inversion of structural geology data for characterising fold geometries first on a range of simple fold shapes in one dimension, and then on a more complicated synthetic 3D model representing doubly plunging parasitic folding.

4.2 Description and modeling of complex fold geometries

Laurent et al. (2016) introduce a global fold frame with three coordinates (x , y , and z) representing the structural elements of the fold. The z coordinate of the fold frame is constrained so that direction vector e_z is perpendicular to the observations of the axial foliation associated with the folding event and observations of the axial surface of the fold (Laurent et al., 2016). The y coordinate of the fold frame measures the distance along the axial surfaces and is constrained so that e_y and e_z are orthogonal and e_y aligns at best with the observations of the fold axis.

Two rotation angles representing the geometry of the fold axis and the fold shape can be calculated from structural data. In Figure 4.1a the fold axis rotation angle is shown as the angle between e_y and the intersection lineation. The fold limb rotation angle is the angle between the normal to the folded foliation and e_z (Figure 4.1b,c). Figure 4.1d shows that the difference in calculated fold limb rotation angle is dependent on the orientation of the fold axis, or the fold axis rotation angle at that location. The S-Plot is a cross plot of a fold rotation angle and the scalar field representing the associated structural elements

direction (Grose et al., 2017a). A sample semi-variogram comparing the fold rotation angles in the fold coordinate system can be used to identify the main wavelength of folding. The S-Variogram (Grose et al., 2017a) also uses the fold frame coordinates to analyse the fold rotations angles. The half wavelength of the fold can be automatically identified by finding the local maximum values of the S-Variogram (Grose et al., 2017a).

In Laurent et al. (2016), the fold shape is constrained by fitting an analytical fold profile that produce a periodical fold geometry. This allowed for the fold to be described by parameters that are comparable to the geometrical description of the fold used by structural geologists, e.g. the fold wavelength, tightness, and asymmetry. Grose et al. (2017a) use a data-driven approach to interpolate the best fit description of the fold based on the structural observations by smoothing and interpolating the observations before fitting a Fourier series. The local orientation of the fold axis is found by rotating e_y around e_z by the fold axis rotation angle (an angle between -90° and 90°). The orientation of the folded foliation is locally constrained by rotating the fold frame around the fold axis by the fold limb rotation angle.

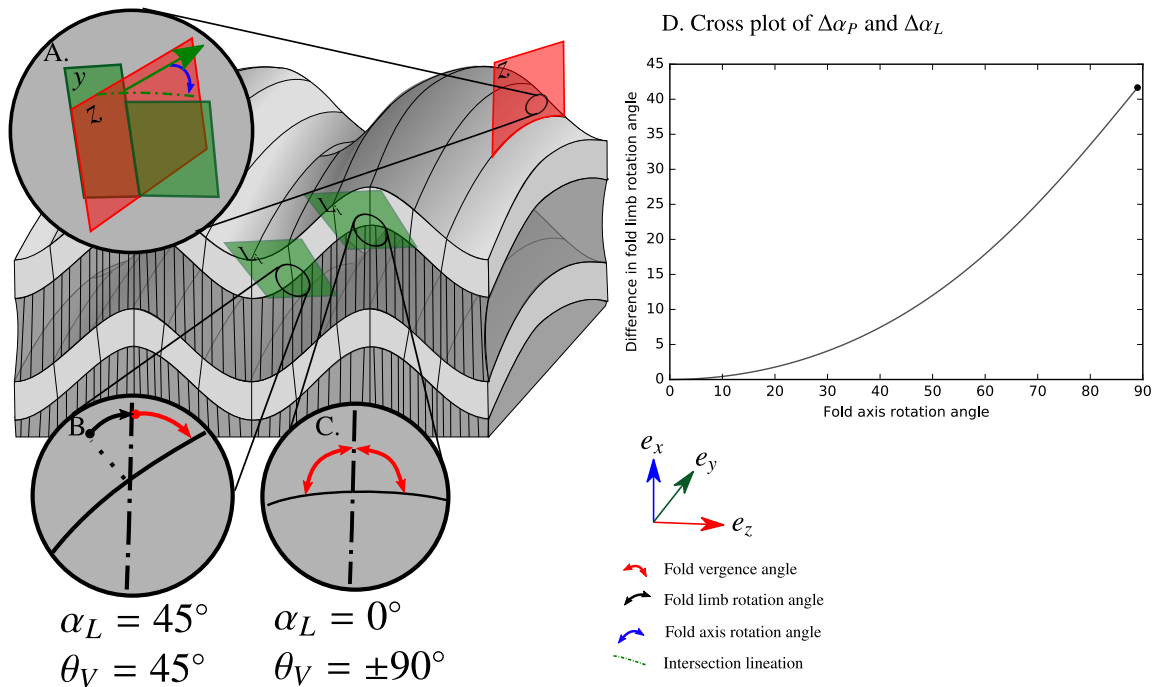


Figure 4.1: Schematic fold showing the fold axis rotation angle. (a) The fold limb rotation angle calculated in the plane normal to the fold axis. (b) and (c). (d) Cross plot showing the change in fold limb rotation angle α_L plotted against changes in the fold axis rotation angle α_p . Adapted from Grose et al. (2017a).

4.3 A probabilistic framework for modeling fold geometries

In both Laurent et al. (2016) and Grose et al. (2017a), only a single best fit fold geometry is produced for a single data set. In practice, the single fold geometry does not capture the shape of all of the observations without over fitting. The fold geometry parameters, either in the form of an analytical profile (Laurent et al., 2016) or the Fourier series parameters (Grose et al., 2017a), should be considered as uncertain variables. In the following section, each model parameter is represented by a probability density function (PDF), and

frame the fold geometry as a Bayesian inference problem. The joint posterior distribution can be sampled from a Gaussian likelihood function.

4.3.1 Fourier series representation of fold geometry

The fold rotation angles ($\alpha_{P,L}$) is first transformed to range from $(-\infty, \infty)$ using the transformation, $\hat{\alpha}_{P,L} = \tan \alpha_{P,L}$ (Grose et al., 2017a). The transformed fold rotation angles can then be represented using a Fourier series, i.e. a linear combination of trigonometric basis functions.

Parasitic folds are very characteristic features of geological multilayer buckle folds. They typically share the same (or similar) fold axis orientation and axial plane orientation as the larger fold. Parasitic folds exhibit a characteristic asymmetry (or fold vergence), often referred to as S and Z shape on either limb of the larger fold, and symmetric W or M shape close to the hinges of the larger fold. Therefore, the geometry of parasitic folding needs to be captured in the interpolated fold rotation angle fields. The observed curve in the S-Plot will be a superposition of both fold wavelengths.

In Grose et al. (2017a), fold wavelengths are inferred by identifying the first local maximum for the S-Variogram. The first local maximum corresponds to the smallest wavelength captured by the structural observations. In most cases, this will be the wavelength of parasitic folds. The scale of identified wavelength depends on the minimal step size used for computing the S-Variogram. It is first computed with a step size 20% greater than the minimal distance between data points for identifying the smallest meaningful wavelength (λ_1). To identify larger wavelengths of the fold the most intuitive approach may be to use previously identified fold wavelength (λ_1) as the step size for a new S-Variogram and repeat the process. However, this will often identify wavelengths equal to multiples of the parasitic fold wavelength. Instead, we identify consecutive pairs of extrema and calculate the moving average for the variogram using pairs of extrema. The moving average can then be analysed for any extrema. If there are multiple wavelengths of folds evident in the dataset then the moving average curve will show either a periodical trend or a general increase as the step distance increases. For an identified wavelength to be valid we apply the following criteria: (1) the variogram for the maximum must be greater than its neighbouring extrema by at least 5%, and (2) if a parasitic fold exists $\gamma(\lambda_2)$ for the larger fold must be 20% greater than $\gamma(\lambda_1)$ of the parasitic fold. These criteria allow for the wavelength of two scales of folding to be captured by the S-Variogram without identifying a wavelength that does not exist.

There are two possible approaches to characterise the geometry of the parasitic folds and larger scale fold using the Fourier series. The wavelength of the larger fold can be used to constrain λ and the number of coefficients, N , can be increased to ensure λ/N is equal to the parasitic fold wavelength. The alternative approach, used in this study, is to explicitly constrain the wavelength of each term of the Fourier series:

$$\hat{\alpha}(x_i|A_0, A_{1\dots n}, B_{1\dots n}, \lambda_{1\dots n}) = A_0 + \sum_{n=1}^N B_n \cos \frac{2\pi}{\lambda_n} x_i + \sum_{n=1}^N A_n \sin \frac{2\pi}{\lambda_n} x_i \quad (4.1)$$

where N is the number of wavelengths identified and λ_n corresponds to the different scale wavelengths.

4.3.2 Bayesian inference

The fold axis and fold limb rotation angle can be represented by Equation 4.1. The parameters could be estimated using a maximum likelihood estimation (MLE) approach if the wavelength(s) λ_n are known.

However, this assumes that the inferred wavelengths are the best representation of the fold geometry. In practice, this will rarely be the case and additional tuning may be required. We also suggest that with increasing geological complexity or where data does not sufficiently define the geometry of the folds, the wavelength values could be optimised using a non-linear approach such as the Levenberg-Marquardt algorithm. These methods typically assume that the model exactly represents the data and tries to optimise the parameters using this assumption.

Geological uncertainty exists both for the collection of the data (measuremental error) and also for the representivity of the measure (Carmichael and Ailleres, 2016), because of the upscaling process that takes part in collecting the data. In a frequentist framework, this could be incorporated using regularized or weighted least squares techniques. We propose using a hierarchical Bayesian approach where the data noise is integrated as a hyperparameter, similar to Muir and Tkalčić (2015).

Bayesian inference is commonly used method for solving non-linear problems with extensive application in the geosciences particularly in solving inverse problems in geophysics (e.g. Kolb and Lekić, 2014; Mosegaard and Tarantola, 1995; Muir and Tkalčić, 2015). The main advantage of using Bayesian methods over standard statistical methods is in the ability to incorporate additional knowledge in the form of prior distributions. Bayesian inference is a method for determining the parameters of a model using Bayes' theorem. The aim is to find the range of possible parameter values to be determined by combining the prior information (in this case, the range of possible fold geometries and predicted wavelength(s) using the S-Variogram) and data (in this case structural observations).

We sample from the posterior distribution $P(x_i, \alpha_i | A_0, A_{1...n}, B_{1...n}, \lambda, \sigma)$ using a Gaussian likelihood function. Using the assumption that the structural observations are sampled from an unknown Gaussian distribution, a similar assumption is used for geological observations in previous work (de la Varga and Wellmann, 2016; Wellmann and Regenauer-Lieb, 2012) and is commonly used in natural sciences where the underlying probability distributions are unknown. Previous studies have used $\sigma^2 = 5^\circ$ (Lindsay et al., 2012) or $\sigma = 10^\circ$ (Wellmann and Regenauer-Lieb, 2012) for the structural uncertainties. In practice, the uncertainty associated with structural observations is unknown and is difficult to estimate robustly. Geological uncertainty can have a wide range of sources that have been broadly separated into three categories (Bárdossy and Fodor, 2001; Cox, 1982; Mann, 1993) and applied to structural geology (Wellmann et al., 2010):

- Type 1: data imprecision, error, and bias, e.g. the location of a contact or the orientation of the surface,
- Type 2: uncertainty related to the unpredictability and randomness in the interpolation, and
- Type 3: lack of knowledge about the structure being modeled, e.g. how representative are the observations of the geometry of the surface being modeled.

In practice, it is impossible to quantify the contributions of each source of uncertainty and as a result, it is impossible to objectively quantify the uncertainty associated with structural observations. When using structural observations to create a 3D model, or in this case characterise the fold geometry, we are interested in the combined misfit between the model and the structural observations, i.e. how closely do we expect the model to fit the data. Rather than adding further subjectivity into the modeling process uncertainty of structural observations can be incorporated into the model by representing the standard deviation of the likelihood function using an uninformed hyperparameter, Jeffery's prior (Sivia, 1996). This allows for the noise in the data to be properly accounted for without requiring subjective, and usually wrong, user input

quantifying the uncertainty associated with the data. This technique has been applied extensively in the geophysical literature (e.g. Bodin et al., 2012a,b; Kolb and Lekić, 2014; Muir and Tkalčić, 2015). This is an improvement on Grose et al. (2017a) where the data are smoothed using a radial basis interpolation scheme and no specific assumptions are made about the noise in the data.

Defining prior distributions

The wavelength(s) ($\lambda_{1...n}$) can be represented by a normal prior distribution with a fixed standard deviation of $\sigma = \lambda/3$. This prior distribution is an empirically informed prior, as 99.97% of the wavelength values sampled from the distribution will be positive, which is a realistic constraint on the wavelength value as negative wavelength values are not physically possible.

The prior distribution for the Fourier coefficients are each represented by Gaussian distributions with a mean of 0 and a standard deviation of 5. These weakly informative prior distributions for the coefficients cover the range of common fold geometries. The choice of coefficient priors does not prevent extreme fold geometries (such as chevron or box folds) from being modeled when strongly supported by data.

Sampling from the posterior distribution

The posterior distribution can usually only be solved analytically for simple low dimensional examples (de la Varga and Wellmann, 2016). Numerical methods are required to obtain a solution for most real examples, e.g. the Maximum A Posterior (MAP) and Markov Chain Monte Carlo (MCMC).

The MAP sampling method finds only a single point solution for the posterior distribution. The MAP solution is the mode of the posterior distribution and in some cases, may not be representative of the true shape of the posterior distribution. For this reason, we propose sampling from the joint posterior distribution using a MCMC sampler implemented in PyMC2 (Patil et al., 2010). This implementation uses the adaptive Metropolis-Hastings step method to tune the parameters to their optimal values. To ensure convergence the sampler is run using a “burn in” period which effectively conditions the parameter values to ensure that the samples are representative of the posterior distribution.

The fold limb rotation angle α_L is calculated using the intersection of the folded foliation and the z coordinate, and the priors for λ_n and A_0 are calculated from these values. The joint posterior distribution is sampled using two likelihood functions, one representing α_P and the other representing the calculated α_L . By sampling from both likelihood functions, we are able to find the joint parameters distributions that best describes both aspects of the folds geometry.

The resulting joint posterior distribution can be sampled returning a combination of fold parameters that represent one location within the posterior PDF. These parameters can either be visualised independently using a histogram or Kernel Density Estimation or as the resulting fold profile geometries. To visualise the resulting fold profiles, we evaluate the resulting fold profile for each location in the posterior distribution and evaluate the resulting density (higher density indicates lower variability).

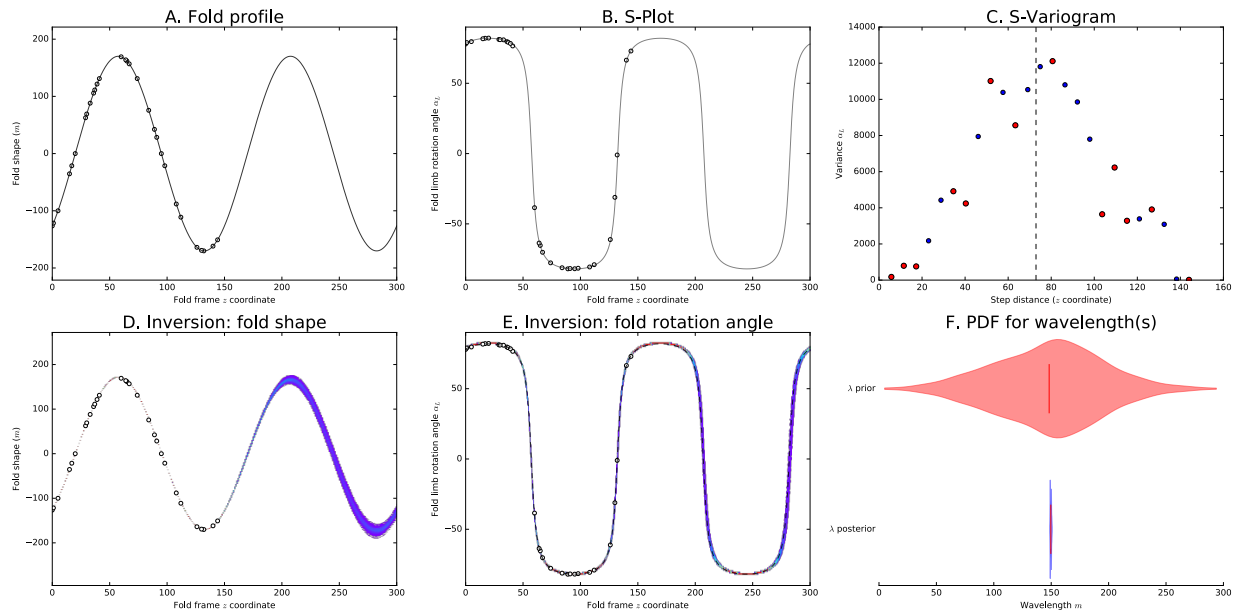


Figure 4.2: Proof of concept 1-D example for a sinusoidal fold geometry. (a) Reference fold shape with a fold wavelength of $150m$ and sample locations. (b) Reference fold profile and sample locations representing the fold rotation angle for the fold geometry in (a). (c) S-Variogram for the structural observations (blue dots in (a) and (b)). The dots represent the variogram for all points at the corresponding step size. The red dots are the locations identified as being local extrema. The estimated half wavelength is shown by the dashed line. (d) Interpolated fold shape probability showing the range of solutions sampled with MCMC. (e) Fold rotation angle profile probability sampled from the posterior using MCMC. (f) Violin plot showing prior and posterior distributions for the fold wavelength.

4.4 Case studies

4.4.1 Proof of Concept

Figure 4.2a is a symmetrical fold shape generated from a sine wave with a wavelength of $150m$. The orientation of the folded layer has been randomly sampled within a single fold wavelength capturing synformal and antiformal hinge zones. The sample locations are represented by the white dots in Figure 4.2a. The S-Plot for the fold shape in (a) is shown in Figure 4.2b and the calculated fold rotation angle for the structural observations in (a) are illustrated by the white dots. Figure 4.2c shows the S-Variogram where the step distance is chosen to be equal to the average nearest neighbour distance between the observations. Local maxima and minima (red dots) are identified in the resulting curve using the gradient descent method (Cauchy, 1847). Each pair of extrema is analysed to determine whether it represents a fold wavelength (e.g. multiscale folding) or if it is just capturing noise in the dataset. In this example, no small wavelength folding exists and the identified extrema are interpolated into a smooth curve and this is analysed to find the main fold wavelength. In this case, the peak at $75m$ is identified as the half wavelength to relate to folding with a wavelength of about $150m$.

The fold rotation angle is interpolated by sampling from the posterior distribution of the parameters for A_0 , A_1 and B_1 using only one wavelength parameter. The prior for the fold wavelength is represented by a Gaussian distribution with a mean of $150m$ and a standard deviation of $50m$. The profile in Figure 4.2d shows the fold geometry interpolated using the observations and fold constraints from the S-Plot (Figure 4.2e). In both Figure 4.2d,e the colour map represents the range of possible fold profiles sampled from the posterior distribution using the MCMC sampler. The sampler was run for 10,000 iterations and a burn in period of 5,000 iterations were discarded. Figure 4.2f shows the posterior and prior distribution for λ_1 . The

wavelength in this example is well constrained with a narrow estimated PDF capturing the reference fold wavelength of $150m$.

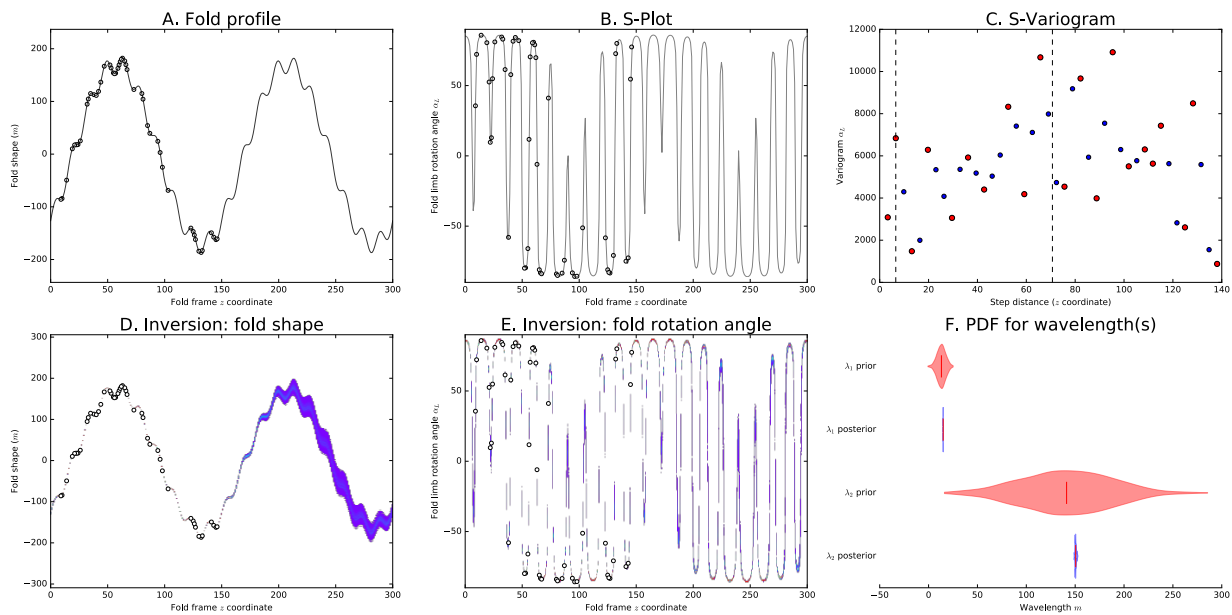


Figure 4.3: Proof of concept 1-D example for parasitic fold geometry. (a) Reference fold shape : $\lambda_1 = 15m$ and $\lambda_2 = 150m$. and sampling locations (b) S-Plot showing fold rotation angle for the fold in (a). (c) S-Variogram for the structural observations, white dots in (a) and (b). The dots represent the variance for all points at the corresponding step size. The red dots are the locations identified as being local extrema. The two estimated half-wavelengths are shown by dashed lines. (d) Interpolated fold profile probability sampled using the MCMC sample. (e) Interpolated fold rotation angle probability sampled by the MCMC sampler. (f) Violin plot showing the posterior and prior distribution for λ_1 and λ_2 .

A more complicated fold shape is shown in Figure 4.3a an additional fold with a wavelength of $15m$ has been superimposed on the reference fold from Figure 4.2. This model has also been sampled capturing one full wavelength of the larger scale fold. Figure 4.3b is the S-Plot for the reference fold shape showing the sample locations. The S-Plot plots the fold rotation angle that is representative of the slope of the fold shape and easily picks out the smaller scale parasitic folds. The large scale fold can be seen by the change in average fold rotation angle for each parasitic fold hinge. Figure 4.3c shows an S-Variogram for the observations in b. Each dot represents the variogram value for pairs separated by the step distance and the red dots also represent the points identified as extrema. A local maximum can be seen at approximately $9m$ and this has significantly higher variogram value than the surrounding extrema and can be interpreted to represent a fold wavelength of approximately $18m$. The extrema (red dots) are interpolated into a smooth curve and the local maxima of this curve is identified to be approximately $70m$ suggesting a wavelength of $140m$ for the larger wavelength fold. For both Figure 4.3d and e, the scaled colour map represents the joint posterior distribution sampled using MCMC. In Figure 4.3f, the prior and posterior distributions for λ_1 and λ_2 are shown. The red polygons show the prior PDFs and the blue polygons show the posterior PDFs. The posterior distribution for the parasitic fold (λ_1) has a mean of 15 and a standard deviation of < 1 suggesting that the data constrains the smaller scale wavelength very well. The posterior for the main fold (λ_2) is similarly well defined with a slightly larger standard deviation.

4.4.2 Parasitic non-cylindrical folding

In the final example, we demonstrate the application of these techniques to a 3D example where structural observations are inverted for the fold geometry. The reference model was generated using Noddy (Jessell and Valenta, 1996) using the python interface, pynoddy (Wellmann et al., 2016). It is a doubly plunging parasitic fold generated by superimposing a fold with a wavelength of 8,000m and amplitude of 1,500m with another fold with a wavelength of 1,000m and amplitude of 500m, the axial surfaces for the two folding events are parallel $N000/90$. To create the doubly plunging effect an additional folding event with an axial surface dipping at 72° to the north striking perpendicular to the existing folds was used with a wavelength of 14,444m and amplitude of 1,000m. The model was sampled from a synthetic topographical section. Observations constraining the orientation of the folded foliation, intersection lineation, and contact location are shown in Figure 4.4. The structural observations for bedding and the fold axis have been perturbed to simulate uncertainty in the observations by sampling from Gaussian distributions describing the azimuth and plunge of the normal vectors with a standard deviation of 10° .

The fold frame for F1 is constructed by first modeling the axial foliation of the fold using the observations for S1 to constrain the gradient of z coordinate, e_z (see Figure 4.1). The fold axis direction field y is interpolated so that $e_z \cdot e_y = 0$, this enforces the geological constraint that the fold axis must be a line within the axial foliation surface. We choose an arbitrary direction of $e_y = e_z \times (0 \ 0 \ 1)$ to make the resulting field unique. The fold axis direction field could also be interpolated using the average fold axis orientation. The differences between these fold profiles would be captured by the first term in the Fourier series (A_0) which controls the shift in the Y axis.

The fold axis rotation angle (α_P) is calculated by finding the angle between the local observation of the fold axis (either intersection lineation or direct observation of the fold axis) and the local orientation of the fold axis direction. This is plotted against the value of the y coordinate shown in Figure 4.5a. The S-Variogram (Figure 4.5c) appears to have a range of approximately 6,000m. There is insufficient data to determine whether the range corresponds to the true half wavelength of the fold or only the sampling extent. It does provide enough information for the weakly informative prior distribution for the wavelength parameter of $N(12000, 4000)$. The fold limb rotation angle (α_L) is calculated using the local intersection lineation between the observations and the fold frame z coordinate (Figure 4.5b). This calculation of α_L is used to define the prior distributions for the fold parameters. Two wavelengths are identified using the S-Variogram (Figure 4.5d). The smaller wavelength results in regular periodicity in the S-Variogram and the first maxima is found at 500m which correlates with a wavelength of 1,000m. The next wavelength is identified by the global maxima for the S-Variogram, in this case, 5,500m and correlates with a fold wavelength of 11,000m (Figure 4.5d). Both the parasitic fold (λ_1) and main folding (λ_2) are represented by normal priors where the mean is the wavelength identified by the S-Variogram and the standard deviation is one third of the mean. All Fourier coefficients (for α_L and α_P) are represented by Gaussian prior distributions $N(0, 5)$.

The joint posterior distribution for the Fourier coefficients and wavelength are sampled using two Gaussian likelihood functions where the standard deviations are represented by two separate hyperparameters. The values of α_L are calculated for each combination of parameters for the Fourier series representing α_P . The parameters are sampled using the MCMC sampler from PyMC2 with a total of 10,000 iterations where 5,000 are discarded for the burn in period.

The geological map (Figure 4.4) is inverted to find the joint posterior distribution for the fold geometry

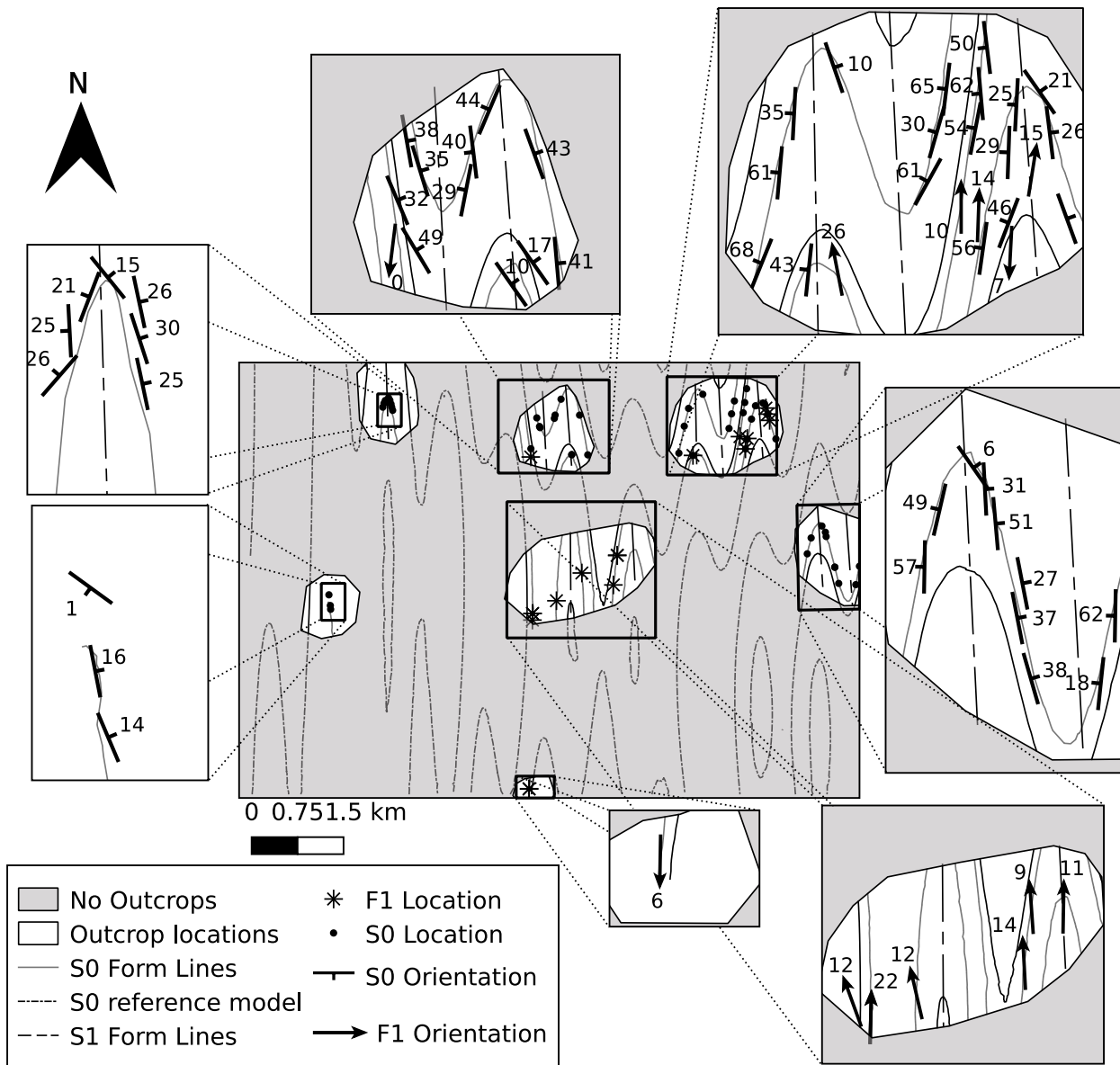


Figure 4.4: Synthetic topographical surface showing form lines representing bedding surface traces and location of orientation data points sampled from the reference model.

parameters for 200 realisations (Figure 4.5e and f). Figure 4.6 shows a random subsample of these models and the corresponding α_P and α_L curves. All models honour the structural style of the reference model showing two large scale fold hinges with parasitic folds occurring on the limbs. It is difficult to quantify the variability between models by visual inspection. Previous studies quantifying geological uncertainty in model simulations have used variability between the observed stratigraphy at unique locations throughout the model suite (Lindsay et al., 2012; Wellmann and Regenauer-Lieb, 2012; Wellmann et al., 2010). Wellmann and Regenauer-Lieb (2012) use information entropy as a measure for variability in geological model iterations. The idea is that the locations with more missing information have higher variability. In their work, the information entropy was calculated on the stratigraphic unit occurrences. In this study, we will adapt the concept of information entropy to the interpolated scalar field value because we are only interested in the geometrical variability between model suites not limited to the resolution of the chosen stratigraphy. Lindsay et al. (2012) increased the stratigraphic resolution by subdividing stratigraphic units.

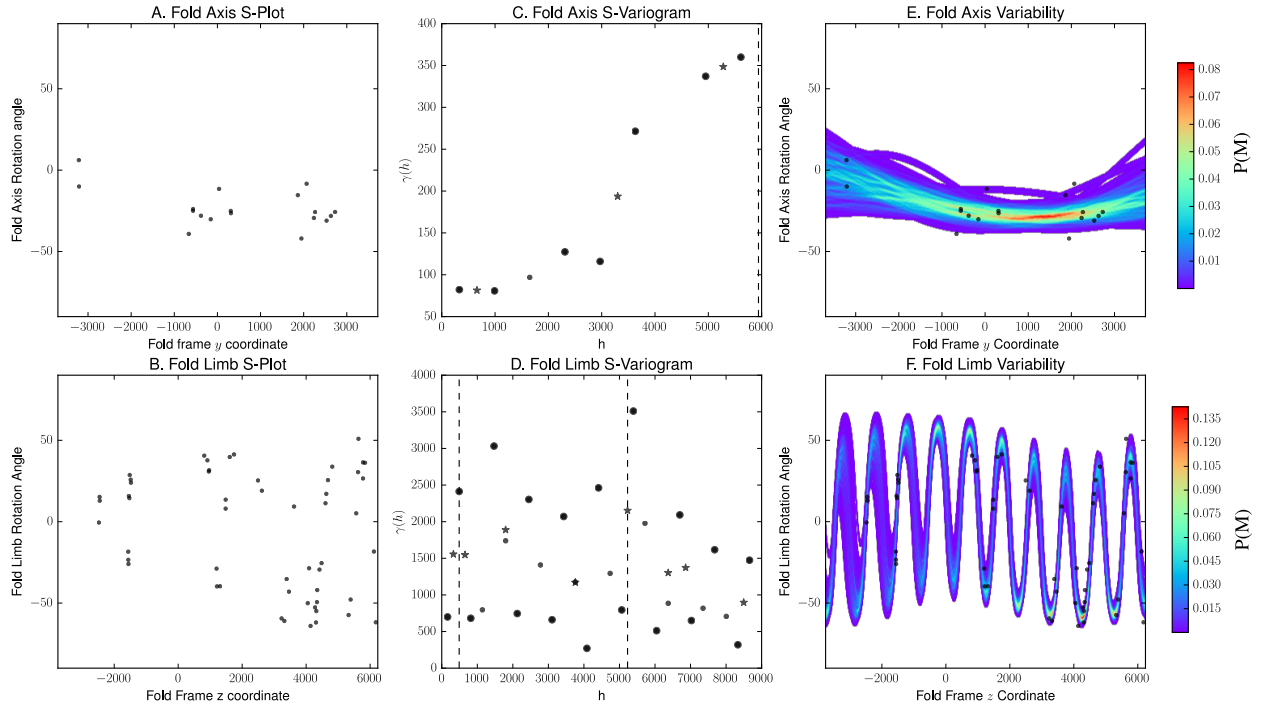


Figure 4.5: Fold geostatistics and Bayesian inference results for synthetic example. (a) S-Plot of α_P and y coordinate. (b) S-Plot α_L and z coordinate. (c) S-Variogram of α_P , dashed vertical line represents the location of $\frac{\lambda}{2}$. (d) S-Variogram of α_L , dashed vertical lines represents the location of $\frac{\lambda_N}{2}$. The fold profiles sampled from the joint posterior distribution are shown in (e) (α_P) and (f) (α_L). Where P(M) is the probability of α_L or α_P for the fold frame coordinates.

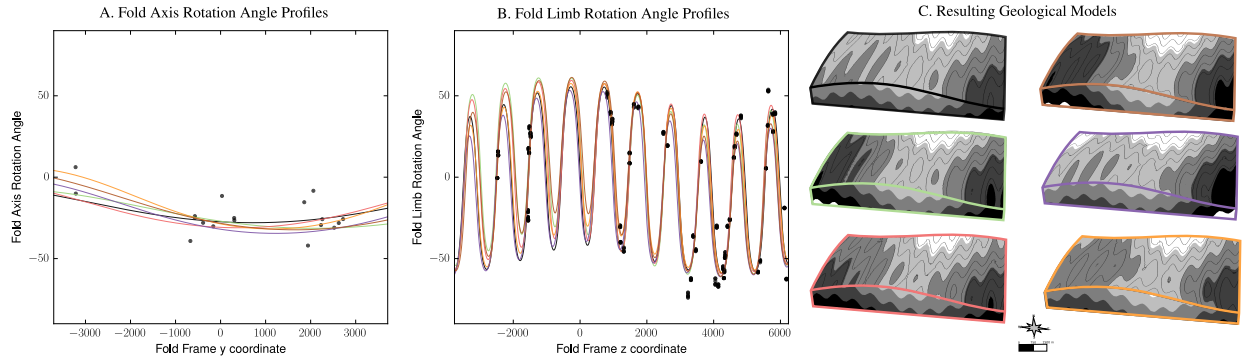


Figure 4.6: Six randomly selected models from model suite of 200 realisations showing: (a) fold axis rotation angle profile, (b) fold limb rotation profile, and (c) the resulting geological models.

Another method to identify regions of structural variability, e.g. location of fold hinges and the geometry of the fold axis, is to compare the orientation of the interpolated surfaces between model suites. The orientation variability can be defined as:

$$V = \frac{1}{N} \sum_{i=1}^N \cos(n_i \cdot n_{av}) \quad (4.2)$$

where V is the local variability value (in degrees), N is the total number of model iterations, n_i is the local orientation of the surface for model i and n_{av} is the mean orientation of all interpolated surfaces for this location in the model. The calculated value of V represents the standard deviation of the distribution of orientations for the particular tetrahedron and as a result, is a good proxy for geological uncertainty. A higher value for V indicates more structural uncertainty at that location in the model suite.

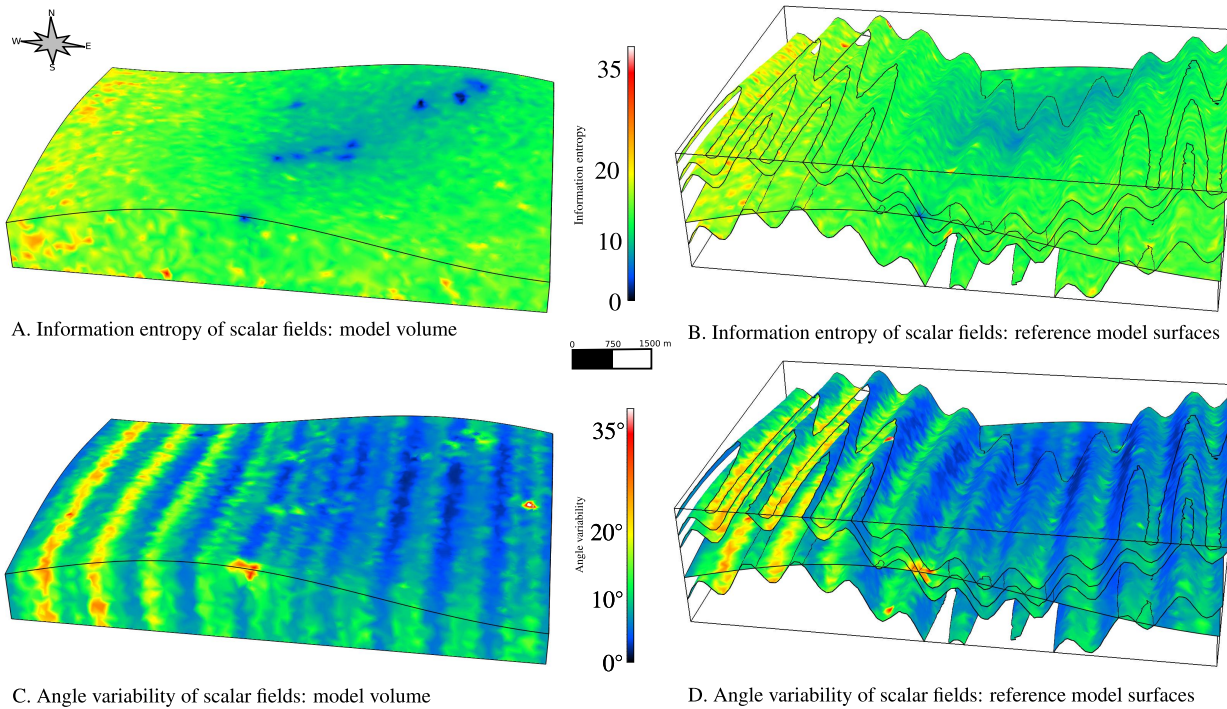


Figure 4.7: Model variability for simulation of 200 models. (a) and (b) information entropy used as a proxy for model variability, higher values indicates higher variability between models. (c) and (d) Angle variability between interpolated models

Figure 4.7a and b show the information entropy for the model volume and the reference model surfaces. In Figure 4.7c and d the angle variability is used as a proxy for geological uncertainty. Both information entropy and angle variability show an increase in geological uncertainty in the western region of the model. The angle variability (Figure 4.7c) shows a periodical trend of high and low variability across the model suite from east to west. The areas of high variability are associated with fold hinges in the reference model with increasing variability where the wavelength of the main fold is not constrained. The regions of lowest variability are associated with locations where there is a higher density of structural data. The locations where the scalar field values are constrained by control points are evident in the circular features in Figure 4.7a.

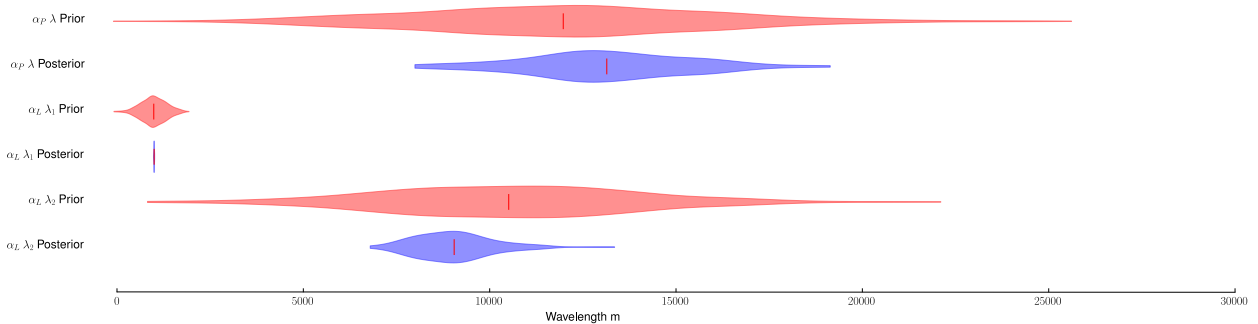


Figure 4.8: Violin plot showing the PDF for the prior (red) and posterior (blue) distributions for the wavelength parameters. Posterior distributions are estimated using a KDE for the wavelength parameters used to generate the 200 models from Figure 4.7

The regions of higher variability highlighted in Figure 4.7 can also be observed in Figure 4.5f where there is more variability in the interpolated profiles between -4000 and 0 in the z coordinate, which correlates to the western portion of the model. The geometry of the parasitic folds are well constrained in Figure 4.5f and Figure 4.8 where the posterior distribution has a relatively small standard deviation of $5m$. The

main fold wavelength is not as well defined and has a standard deviation of $300m$. This variation in the posterior for the larger wavelength is a major contribution to the variability increasing away from the main data locations in the north east of the model.

In Figure 4.5e there is high variability between the fold axis rotation angle profiles. The range in profiles can be up to 20° . However, in the variability models (Figure 4.7) this is not evident. A subtle trend can be observed along the fold axes in the information entropy Figure 4.7a and in the eastern region of the model in Figure 4.7c where the angle variability slightly increases in the north and south areas of the model. There are three reasons why the fold axis rotation angle does not contribute to model variability as significantly as the fold limb rotation angle: (1) In this model, the fold axis is only gently doubly plunging, with a maximum of 50° of variation between observations compared to up to 100° for the fold limb rotation angle; (2) in the western region of the model the contribution of the larger wavelength shifts the location of parasitic fold hinges and may cause variations in the orientation of the folded surface of up to 100° and; (3) the variation in fold axis is partially accounted for when the fold limb rotation angles are recalculated for each iteration of the fold axis due to the joint inversion of both angles.

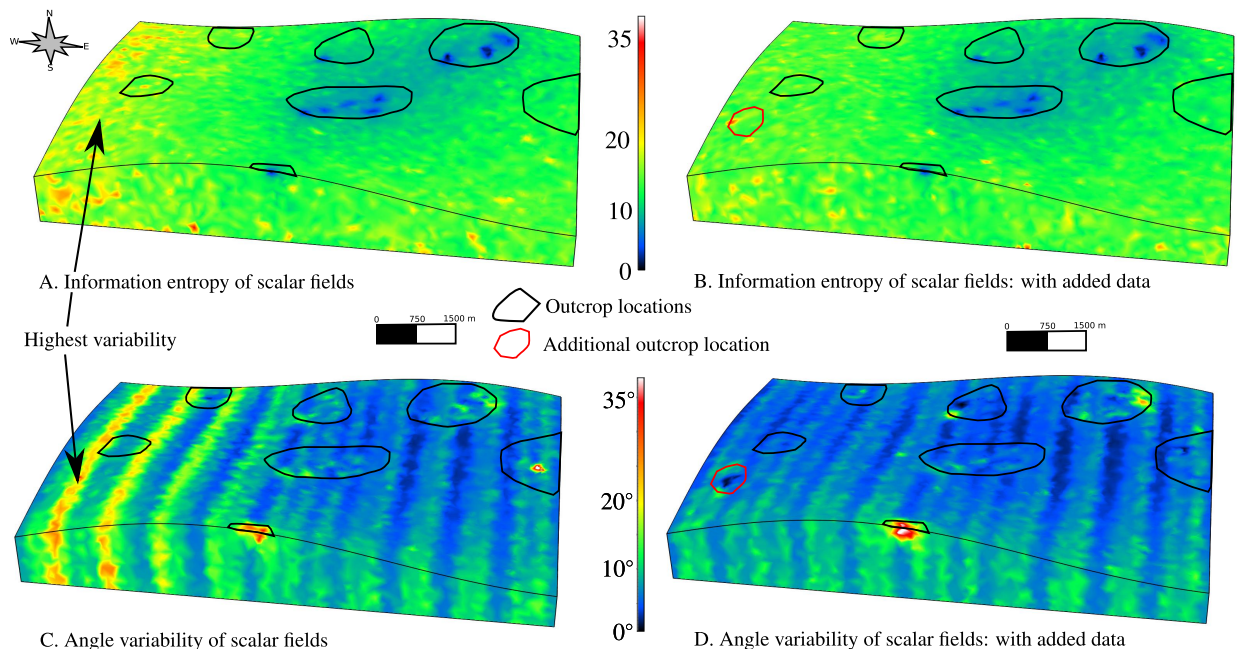


Figure 4.9: Comparison of model variability before and after adding additional data in the most variable location. (a) Information entropy calculated on interpolated scalar field for 200 model iterations using data in Figure 4.4. (b) Information entropy calculated on interpolated scalar field for 200 model iterations with additional data (c) Angle variability calculated on interpolated scalar field for 200 model iterations using data in Figure 4.4. (d) Angle variability calculated on interpolated scalar field for 200 model iterations with additional data. Outcrop locations are outlined in black and the additional outcrop location is outlined in red.

In Figure 4.7 the variability increases away from geological observations. The posterior distribution for the larger wavelength fold has a significantly higher standard deviation compared with the smaller parasitic fold posterior distribution. In order to reduce model variability, more data is needed to constrain the wavelength of the main fold. Figure 4.9 shows a comparison between the variability models for the original dataset (a and c) and a new model suite where additional orientation data has been sampled (b and d). The orientation data constrains the geometry of an additional parasitic fold hinge at the location of highest variability (indicated in Figure 4.9a,c). These additional orientation observations reduce the higher variability trend in the western portion of the models. Most of the variability in the updated model suite is associated with the location of the fold hinges and the geometry of the fold axis. The uncertainty associated

with the main fold geometry has been significantly reduced. The standard deviation for the wavelength posterior has been reduced by 68%. There are locations that exhibit localised high angle variability and low information entropy. They are associated with the locations for value control points that are collocated with the fold axis observations. This is because all model realisations are enforced to have very similar scalar field values at these locations. Varying fold models are thus accounted for by significant orientation variations at these locations. These are modeling artefacts resulting from the interpolation method. These artefacts could be reduced if value constraints, that in a geological sense only identify the stratigraphic unit and not the distance from contact locations, are implemented as inequality constraints (Frank et al., 2007; Hillier et al., 2014) or by using the iterative methods proposed by Collon et al. (2016). Inequality constraints define boundary values (e.g. the range for a particular stratigraphic unit) to the model instead of forcing a scalar field value at that location. This would result in less significant variability in the interpolated geometries.

4.5 Discussion

In this contribution, we have framed geological modeling as an inverse problem and demonstrated that using the appropriate geometrical description of geological structures it is possible to invert geological data for 3D geometry. Grose et al. (2017a) use the wavelength parameter estimated from the S-Variogram as a fixed constraint for the fold wavelength and solve the Fourier coefficients using least squares regression. The quality of the resulting fold profiles is dependent on the wavelength estimated from the S-Variogram. In some cases, it may not be possible to exactly pick the fold wavelength from the S-Variogram, resulting in a poor fit and/or unlikely model geometries. For example, in the parasitic non-cylindrical fold model (Figure 4.8) the mean of the prior distribution is the estimated wavelength using the S-Variogram. Where the wavelength is well characterised by the structural observations, the estimated mean and the mean of the posterior distribution are very close. Where the folds are not as well characterised by the data, e.g. the larger wavelength fold, the estimated mean is outside of one standard deviation from the posterior mean. This suggests that the wavelength estimated from the S-Variogram is not the best representation of that fold. The posterior in this example (Figure 4.8) has a large standard deviation suggesting that the data does not contain enough information to define a single wavelength value. If only a single model is produced and no uncertainty is associated with the different geometrical attributes, it would be difficult to predict the location and type of data that should be collected to reduce model uncertainty. When the posterior distribution for the fold geometries is sampled it is much easier to isolate the particular aspects of the fold geometry that are uncertain (e.g. in the synthetic case study more data constraining the large wavelength fold reduced model uncertainty).

The choice of prior distributions controls the search area (in parameter space) where parameter estimates can be drawn from. If the prior distributions are too restrictive then the resulting parameter estimates may not be able to represent the data. If the priors are too broad then the sampler may require a large number of iterations or may not converge. The choice of prior distributions is an important aspect of Bayesian statistics. In this study, we have chosen to use weakly informative prior distributions that are based on, where possible, empirical estimates for the parameter values from the geological data. While the chosen prior distributions are quite broad they allow for the model to be supported by data. However, in some cases, there may not be enough data for the joint posterior distribution to converge. There may be addi-

tional information that cannot be directly incorporated into the model using standard observations, such as fold wavelengths from outside of the map area, from geophysical data sets, or geological knowledge. In these cases, the relevant prior distributions could be made to be more informative. An alternative approach would be to incorporate these additional observations using an additional likelihood function. For example, de la Varga and Wellmann (2016) use multiple likelihood functions to incorporate additional geological knowledge such as fault offset and layer thickness that cannot normally be incorporated into the geological modeling system.

Most case studies where 3D models have been used to investigate geological phenomena have not incorporated parasitic folding into either the construction or the geometry of the geological model (e.g. Basson et al., 2016; Maxelon et al., 2009; Vollgger et al., 2015). This is mainly because using a standard modeling workflow the geometry of these folds would need to be defined manually by the user gleaned from either interpretive cross sections or synthetic data to constrain the resulting geometries. This process would be time consuming, subjective and probably not aid in interpreting the geology. Generally, parasitic folds do not significantly affect the resulting large scale 3D geometries and are ignored during modeling. This approach is not consistent with field studies where parasitic folds are often used by the structural geologists to understand larger scale fold geometries and overprinting relationships (e.g. Armit et al., 2012; Basson et al., 2016; Forbes and Betts, 2004; Tian et al., 2016). Another consideration is that parasitic folds will affect the spatial correlation between structural observations (e.g. if structural data is collected from opposing limbs of a parasitic fold, out of context, this information may misinform the large scale model). Inverting structural data it is possible to identify both the larger scale geometry and the parasitic fold geometry as demonstrated in Figure 4.3. This means that models can be created that extrapolate the geometry of parasitic folds even where structural observations have not been recorded. An alternative approach would be to remove the parasitic folds from the model by identifying which structural observations are associated with the short limb and hinges of parasitic folds. Both of these approaches incorporate the information provided by the parasitic folds into the resulting model description.

A focus for geological modeling research has been in accounting for uncertainties in geological models (e.g. Cherpeau et al., 2010a, 2012; de la Varga and Wellmann, 2016; Jessell et al., 2010; Lindsay et al., 2012, 2013b; Suzuki et al., 2008; Thiele et al., 2016b; Wellmann and Regenauer-Lieb, 2012; Wellmann et al., 2010). In these studies, multiple realisations of the geological model is generated by perturbing the original structural data set or existing model geometry. These studies have had two main caveats: (1) the difficulty for structural interpolation methods to generate realistic geological models from an input dataset particularly in polydeformed terranes (Jessell et al., 2014), and (2) the uncertainty has only been considered associated with the structural observations rather than being associated with the interpolation method (Aug et al., 2005). To overcome the first caveat the geologist has been forced to constrain areas of the models using interpretive constraints (Caumon et al., 2009) that can be subjective and can introduce additional human bias (Bond et al., 2007a). In previous methods, most of the simulated structural uncertainty has been associated with fault geometries (e.g. de la Varga and Wellmann, 2016; Lindsay et al., 2012; Wellmann and Regenauer-Lieb, 2012; Wellmann et al., 2010). Folds have typically been difficult to model using implicit approaches because the interpolation algorithms generally fit the smoothest surface to the resulting model and folds generally create regular patterns of localised curvature variation. For this reason when the structural observations are perturbed (de la Varga and Wellmann, 2016; Lindsay et al., 2012; Wellmann and Regenauer-Lieb, 2012; Wellmann et al., 2010) the interpolation algorithm will in most cases smooth the

introduced perturbations and the resulting model variability will not reflect the uncertainty in the geological structures. We have presented a method for simulating structural uncertainty where no assumptions about the representivity of the data is needed. The misfit between the model and the observations is incorporated into the probabilistic framework using the uninformative prior distribution. This results in the variability between inversion realisations being closely related to the geometry of the structures (e.g. Figure 4.7). In contrast, if uncertainty is simulated by perturbing the structural data and the same interpolation is used the resulting models will have increased uncertainty only in the locations where the model is constrained.

4.6 Conclusion

In this contribution, a new method for inverting geological data for fold geometries is presented. Folds are represented using the Fourier series description of fold geometry introduced in Grose et al. (2017a) and the fold modeling framework of Laurent et al. (2016). The probabilistic representation of the fold geometry offers improvements in finding the best fit fold geometry for a structural dataset, a new approach to simulating structural uncertainty without perturbing structural observations and can help target locations for additional data collection. Variability in the interpolated models is compared using information entropy on the resulting scalar field as well as a new metric to classify the geometrical variability between models. The combination of a local quantification of model uncertainty and the posterior distributions for the fold geometry parameters can be used to reduce overall model variability. In a synthetic case study, the model variability is reduced by up to 60% after adding data characterising a single parasitic fold hinge. These methods could be incorporated into geological exploration where the highest variability locations can be used as target locations for further data collection (e.g. field mapping and/or drilling).

Acknowledgments

This research was partially funded by Australian Research Council Linkage grant LP140100267, and partly supported by the “Investissements d’avenir” Labex RESSOURCES21 (ANR-10-LABX-21-01). The authors are grateful to the industrial and academic sponsors of the Gocad Research Consortium managed by ASGA (Association Scientifique pour la Géologie et ses Applications, <http://ring.georessources.univ-lorraine.fr/>) for their support. We thank Paradigm for providing the GOCAD-SKUA software and API. The final case study in this publication was generated with the StructuralFactory plugin for Gocad, based on RING’s StructuralLab plugin. Last but not least, the authors would like to thank Guillaume Caumon and Paul Cupillard for their feedback and discussions. Supplementary data including the code for figure 2 and 3, the data for the final case study and the nobby history file can be accessed from: <https://figshare.com/s/03cdb58d7727aad73daf>.

Chapter 5

Inversion of geological data and knowledge

L. GROSE ¹ , L. AILLERES ¹ , G. LAURENT ² , R. ARMIT ¹

¹School of Earth, Atmosphere and Environment, Monash University PO Box 28E, Victoria, Australia

²GeoRessources (UMR 7359), Université de Lorraine-ENSG, CNRS,CREGU
Campus Brabois, TSA 70605, 54518 Vandoeuvre-lès-Nancy Cedex, France

Abstract

The process of building three dimensional (3D) geological models can be framed as an inverse problem where a model describing the 3D distribution of rock units is non-uniquely derived from geological observations. The inverse problem theory provides a powerful framework for inferring these parameters from all geological observations, in a similar way to how a geologist can iteratively update their structural interpretation while mapping. A priori geological knowledge is usually indirectly incorporated into 3D models using the geologist's non-unique interpretation as form lines, cross sections and level maps. These approaches treat constraints derived from geological knowledge in the same way as direct observations, diluting and confusing both information provided by geological knowledge and hard data resulting in significant subjectivity. We present a geological inversion using Bayesian inference where geological knowledge can be incorporated directly into the interpolation scheme with likelihood functions and informative prior distributions. The combined inversion of geological data and geological knowledge significantly reduces the uncertainty in the interpolated geometries. We demonstrate these approaches on a series of synthetic 1D fold shapes as a proof of concept and a case study from the Proterozoic Davenport Province in the Northern Territory, Australia. The combined inversion of geological data and knowledge significantly reduces the range in possible fold geometries where data is sparse or highly ambiguous. This could be used by geologists while mapping to propagate information about uncertainties throughout the mapping/model building process. It would allow for different structural interpretations to be rapidly tested while mapping for targeted data collection.

5.1 Introduction

Building three dimensional (3D) geological models is a complicated task requiring an assimilation of available datasets, prior geological interpretation, and geological knowledge. Recent developments in 3D modeling algorithms and techniques (Calcagno et al., 2008; Caumon et al., 2013; Cowan et al., 2003; Grose et al., 2017a,b; Hillier et al., 2013, 2014; Laurent et al., 2016; Massiot and Caumon, 2010) have significantly improved how direct observations can be used to constrain surface geometries. The process of creating 3D geological models can be framed as an inverse problem where the aim is to infer parameter values for the interpolation algorithm given geological observations (Grose et al., 2017b). Geological models, and as a result, geological inversions are usually under constrained. However, there are often geological rules and additional geological knowledge that is not directly incorporated into the interpolation schemes (Jessell et al., 2014, 2010).

A priori geological knowledge is usually indirectly incorporated into 3D models using subjective form lines, cross sections and level maps (Jessell et al., 2014, 2010). Usually these interpretive constraints are defined by the geologist summarising available observations and geological knowledge. The geologist's interpretation is highly subjective, and will result in a single non-unique solution to a complex problem (Jones et al., 2004). This is problematic because the interpolation algorithms used for implicit modeling treat these interpretive constraints in the same way as direct observations, which can dilute the information provided by geological knowledge and can be a significant source of subjectivity. The geological knowledge used by the geologist to guide their interpretation needs to be incorporated into the geological inversion schemes, allowing for the range in possible solutions to be explored.

A new framework for modeling folded surfaces has significantly improved the incorporation of struc-

tural geology concepts (Grose et al., 2017a,b; Laurent et al., 2016). Using these developments, structural modeling can be framed as an inverse problem, and structural data can be inverted for fold geometries (Grose et al., 2017b). This approach uses Bayesian inference to sample from the joint posterior distribution of the parameters representing the geometry of the fold axis and the fold shape for structural data.

The description of an inverse problem using Bayesian inference can be easily generalised to incorporate a diverse range of observation types (Malinverno and Parker, 2006). In this contribution, we incorporate geological knowledge into the inversion framework using a combination of informative prior distributions and additional geological likelihood functions. The addition of geological knowledge significantly reduces the variability in interpolated model geometries where the direct observations are sparse or highly ambiguous. We present proof of concept 1D synthetic examples to demonstrate the application of these new likelihood functions to known examples, and a 3D case study from the Davenport Province in the Northern Territory, Australia.

5.2 Geological knowledge and interpretation

Geologists use visual features in an outcrop to define geological observations (Frodeman, 1995; Rudwick, 1976). These characteristics and patterns in the rocks by themselves do not provide any geological information, and it is only by correlating between outcrops and applying geological rules that they can be related to geological features such as fault planes, tectonic cleavages, or stratigraphic horizons. Frodeman (1995) argues that the process of geological reasoning defines geosciences as an interpretive and historical science, highlighting the role of interpretation, synthesis, and broader knowledge when constructing and testing hypotheses, and the iterative nature of this process. Most geological observations are made in the context of the outcrop or the regional structure and these observations are then used to update understanding of the outcrop, deformational history, and/or regional structures. An example of this is seen when making a geological map the geologist usually builds their interpretation while mapping and uses this knowledge to guide further interpretations. This can be subjective and is a significant source of uncertainty as it is difficult to separate observations from interpretation (Jones et al., 2004). It also means that when creating a map, geologist's generally only record their favoured interpretation and not the range of possible interpretation. The geologist's interpretation is usually guided by geological knowledge to interpolate between direct observations. Geological knowledge includes observations that describe the geometry of a surface but do not locally constrain the geometry of that surface. They may not necessarily have an associated location and could be a combination of guesswork, intuition and 'gut feeling' (Jones et al., 2004). Geological knowledge is updated by combining observations and geological rules, for example, using observations of one structure to infer the geometry of another or by visualising the geometries that could be physically possible. Folds are often described using: hinge geometry, tightness, wavelength, amplitude, symmetry, and structural vergence. These descriptive terms are difficult to turn into a systematic criterion for modeling.

In summary, the interpretation process is highly subjective and will result in a single non unique solution to a complex problem (Jones et al., 2004). It has been suggested (Jones et al., 2004), that an interpolation algorithm capable of incorporating indirect geological observations would provide a way of propagating not only the uncertainty associated with each observation but also the uncertainties associated with the interpretation.

5.3 Structural modeling of folds as an inverse problem

Recent developments in implicit modeling techniques and statistical methods for characterising fold geometries have significantly improved the use of geological observations for modeling folded surfaces (Grose et al., 2017a,b; Laurent et al., 2016). These methods have incorporated the fundamental concepts from structural geology into implicit modeling schemes. A curvilinear coordinate system is defined to characterise the structural elements of the fold with three coordinates represented by 3D scalar fields x , y and z . Three direction vectors (e_x , e_y and e_z) are defined by the normalised gradient of the scalar fields representing the fold frame coordinates (Laurent et al., 2016). The z coordinate is interpolated so that e_z is orthogonal to the axial foliation and the isosurfaces of z are parallel with the axial surface of the fold. The y coordinate is interpolated so that y measures the distance along the axial surface of the fold and e_y represents the trend of the fold axis. For similar folds, the geometry of the fold is the same for conformable layers and x does not need to be interpolated. The orientation of the folded surface is defined by rotating the direction of the y coordinate (e_y) by the fold axis rotation angle (α_P) around e_z . The resulting direction will be the local orientation of the fold axis. The orientation of the folded surface is defined by rotating the fold frame around the fold axis by the fold limb rotation angle (α_L).

Using this scheme, fold geometries can be represented by two 1D curves that respectively capture the geometry of the fold axis in the axial surface and the fold shape looking along the fold axis. Grose et al. (2017a) calculate the fold rotation angles directly from structural observations and use the fold frame coordinates to extract the different elements of the fold geometry. The S-Plot, is a cross plot of either fold rotation angle and the associated fold frame coordinate, *e.g.* α_P is plotted against y and α_L against z . A sample semi-variogram (S-Variogram) also calculated on either fold rotation angle using the associated fold frame coordinate can be used to automatically identify the wavelength of folding (Grose et al., 2017a). The geometry of the fold can then be represented using two 1D Fourier series one representing α_P for the y coordinate values and another representing α_L for z values. Grose et al. (2017b) use these 1D functions as the forward model for a geological inversion where the fold rotation angles calculated from observations are used to falsify possible fold geometries. The unknown parameters relate to the Fourier series coefficients, fold wavelengths and a misfit parameter for each rotation angle.

There are two different approaches to solving inverse problems: The Frequentist approach uses observations to directly infer the model parameters, and the Bayesian approach uses observations to modify existing understanding of the model parameters (Tarantola, 2006). As described in Grose et al. (2017b), Bayesian inference is used to sample from the joint posterior distribution of the fold parameters representing the fold axis and fold shape. The probability of possible parameters representing the fold geometry can be updated using a likelihood function that evaluates the probability of the observations (D) given the current parameter values (θ). This can be determined using Bayes' theorem where the joint posterior distribution of the parameters $P(\theta | D)$ can be updated using the likelihood $P(D | \theta)$ of the data given the parameters, the prior probability of the parameters $P(\theta)$ and the probability of the data $P(D)$:

$$P(\theta | D) = \frac{P(D | \theta) \cdot P(\theta)}{P(D)} \quad (5.1)$$

$P(D)$ is constant for all parameter values and means the joint posterior is proportional to the likelihood multiplied by the prior distributions. The joint posterior distribution can be sampled from using numer-

ical techniques; in this contribution, we use a Markov Chain Monte Carlo (MCMC) sampler using the Metropolis-Hastings algorithm implemented in PyMC2 (Patil et al., 2010).

The prior distribution of the parameters $P(\theta)$ represent prior knowledge of parameter values. Grose et al. (2017b) use weakly informative priors that allow for the range of physically possible fold geometries to be modeled. The calculated fold limb rotation angle for structural data depends on the current orientation of the fold axis (Grose et al., 2017a). This means that the likelihood function $P(D | \theta)$ has two parts, one to represent the probability of the observed fold axis rotation angle values given the parameter values and another part represents the probability of the observed fold limb rotation angle values given the parameter values for both Fourier series. Within this framework, the uncertainty in the observations can be incorporated into the description of the fold geometry representing the misfit between the model and the observations using an uninformative prior distribution, Jeffrey’s prior (Sivia, 1996). This means that no assumptions about the inherent uncertainty of the data are required, and a range of possible interpretations can be created from available structural data.

This approach (Grose et al., 2017b) primarily considers direct structural observations and does not provide a framework for incorporating geological knowledge into the inversion. In the following section, we extend the method using additional likelihood functions and informative prior distributions that allow geological knowledge to be incorporated into the geological inversion.

5.4 Adding geological knowledge to the geological inversion

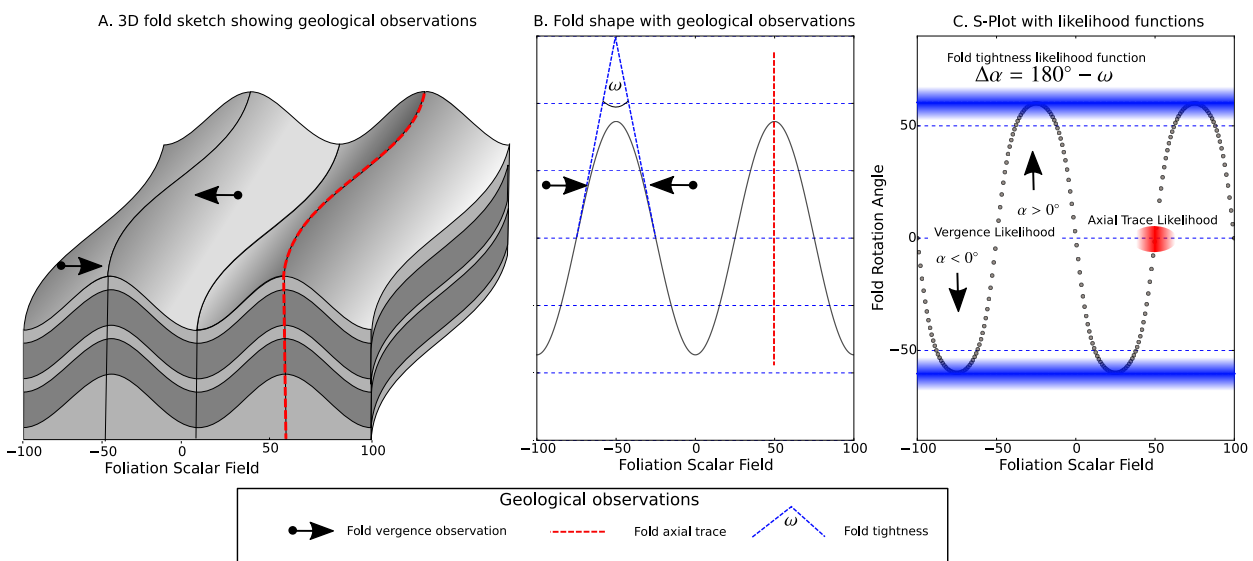


Figure 5.1: 3D fold sketch showing knowledge likelihood. A: 3D fold sketch with two vergence constraints and an axial trace likelihood. B: Fold shape for the fold in (A) showing fold tightness, vergence constraints and axial trace location. C: S-Plot showing the vergence constraints enforcing the sign of the rotation angle, tightness constraints, enforcing the range in rotation angle and axial trace location. The colour shading for the tightness and axial trace indicates the fuzzy nature of these constraints.

The inversion of geological observations can be easily generalised using Bayesian inference to incorporate a diverse range of observations for solving the inverse problem (Malinverno and Parker, 2006). For example, fault offset, and stratigraphic unit thickness can be incorporated into geological modeling using standard implicit schemes (de la Varga and Wellmann, 2016; Wellmann et al., 2017). This approach uses geological data as the parameters for the inverse problem and uses geological knowledge to falsify the

Table 5.1: Fold tightness descriptive terms and interlimb angle

Descriptive terms	Interlimb angle	Likelihood $N(\mu, \sigma)$
gentle	$180^\circ - 120^\circ$	$30^\circ, 30^\circ$
open	$120^\circ - 70^\circ$	$85^\circ, 25^\circ$
close	$70^\circ - 30^\circ$	$130^\circ, 20^\circ$
tight	$30^\circ - 0^\circ$	$165^\circ, 15^\circ$
isoclinal	0°	$180^\circ, 10^\circ$

resulting models. We propose using geological likelihood functions describing geological knowledge of folded surfaces into the fold modeling framework (Grose et al., 2017a,b; Laurent et al., 2016).

5.4.1 Fold tightness

Fold tightness can be quantified by measuring the interlimb angle for folds (*e.g.* ω in Fig. 5.1B). Generally, instead of measuring the fold interlimb angle the fold tightness is described using the terms recommended by Fleuty (1964). These terms each cover a small range of interlimb angles and are common nomenclature used by structural geologists when describing the shape of the fold looking down plunge. A similar measure termed hinge angle (Bastida et al., 2005; Williams and Chapman, 1979) can be used perpendicular to the fold axial surface to describe the degree of variation of the fold axis. The expected range of fold rotation angle can be calculated for the interlimb/hinge angle (ω) as $\Delta\alpha_{L,P} = 180 - \omega$.

Table 5.1 contains the different descriptive terms recommended by Fleuty (1964) and the associated range in fold tightness. These descriptive terms can be incorporated into the fold modeling framework using normal likelihood functions. The likelihood function parameters are listed in Table 5.1 and are defined so that the range of possible fold rotation angle for the descriptive term is within one standard deviation of the mean. The likelihood function can either be implemented for defined domains within the model or can be implemented as a global value. In the first case, the median value of the fold rotation angle is calculated for the fold frame coordinates defining the domain. In the second example, the median value is calculated for a complete wavelength of the largest fold which will be representative of the whole model area. The calculated median value is then used in the normal likelihood function given the associated parameters in Table 5.1.

5.4.2 Fold vergence

Structural vergence can be obtained by finding the acute angle between two consecutive foliations. Vergence is the direction to rotate the younger foliation towards the older foliation and indicates the direction towards the nearest antiform (Bell, 1981). Vergence provides the structural geologist with information related to the location of fold closures that may not be visible due to outcrop limitations. Vergence can also be calculated from the asymmetry of parasitic folds where the long limb of the fold indicates the vergence direction. A similar concept can be applied to the fold axis to determine the fold plunge. This has been named fold hinge-line vergence and is defined by asymmetric variations of the intersection lineation in the foliation plane (Alsop and Holdsworth, 1999). Although this is not commonly observed or recorded the geologist often has some additional knowledge about the plunge of the fold axis that could be used to infer the hinge-line vergence.

Structural vergence and fold hinge-line vergence can be used to determine the relative sign of the fold

rotation angles. Fig. 5.1A and B show two vergence observations on a schematic 3D fold (A) and the fold shape in the fold frame coordinates (B). When plotted on the S-Plot (Fig. 5.1C) the vergence constraints indicate that the sign of the rotation angle should be negative at $z = -75$ and positive at $z = -25$. This can be included in the inversion scheme using a likelihood function that assesses the sign of the rotation angle. We use a discrete probability density function where the probability of a consistent vergence constraint ($v = [-1, 1]$) is given by:

$$P(\text{Sign}(\alpha_{L,P}) = v) = p \tag{5.2}$$

where p is the probability of the current combination of parameters being consistent with the vergence observations. We suggest that $p < 1$, because if $p = 1$ the probability of a conflicting constraint is 0 and therefore it is not possible for these constraints to not be honoured by the sampler.

5.4.3 Fold symmetry/asymmetry

When mapping, geologists will often be able to observe whether folds are symmetrical or asymmetrical. Fig. 5.2A shows a symmetrical fold shape and (B) an asymmetrical fold shape. In Fig. 5.2C the fold rotation angle curve for the folds in (A) and (B) are plotted. The symmetrical fold (blue curve) has a median value of 0° represented by the horizontal blue line. The asymmetrical fold (green curve) has been vertically shifted on the S-Plot and has a median fold rotation value of 40° shown by the horizontal green line. Fold asymmetry and tightness both describe the fold shape and are not independent (Hudleston, 1973). The median value of the fold rotation angle depends on the tightness of the fold and the degree of asymmetry. A gentle fold that is highly asymmetrical would have a similar median value to a tight fold that is only gently asymmetrical. The tightness and asymmetry can be separated by finding the ratio between the absolute value of the median and range of the fold rotation angle for the current model parameters. This is shown in Fig. 5.2 where the asymmetry is shown as the absolute value of the median fold rotation angle value divided by the range of the fold rotation angle values for the curve (e.g. blue and green vertical lines in Fig. 5.2C).

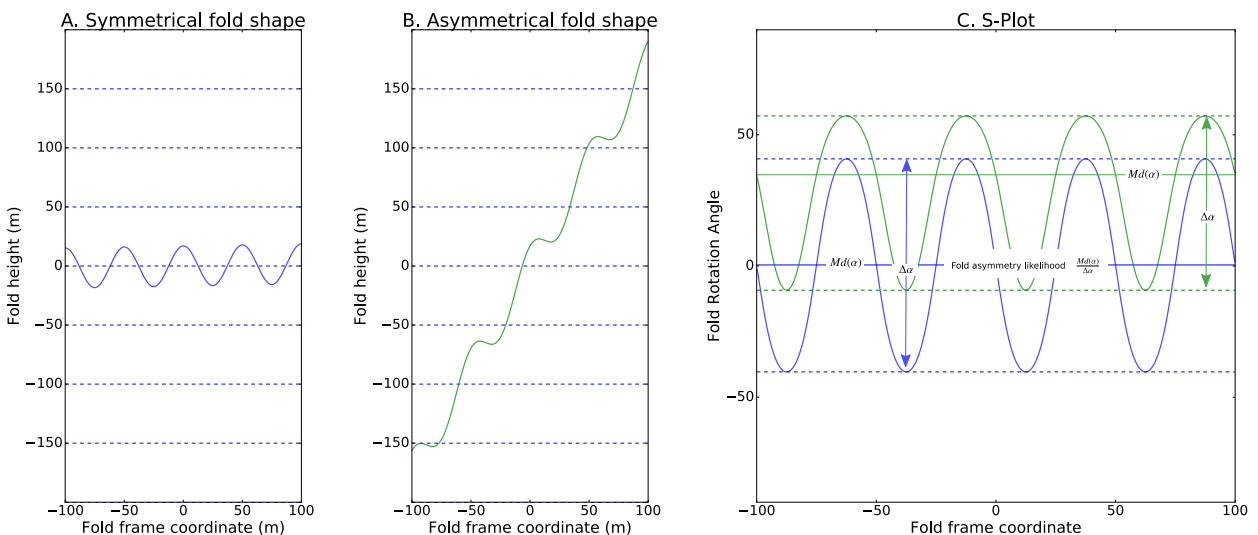


Figure 5.2: Fold asymmetry likelihood. A: Symmetrical fold shape B: Asymmetrical fold shape C: S-Plot showing fold rotation angle for the fold in (A) and (B). $\Delta\alpha$ and $Md(\alpha)$ is shown for both fold rotation angle curves.

This measure of asymmetry can then be incorporated using a normal distribution as the likelihood function assessing this ratio. When mapping, the degree of asymmetry is usually not recorded and generally

folds are described as either symmetrical or asymmetrical. For this reason, we propose having a likelihood function for symmetrical folds using a normal distribution with a mean of 0 and a standard deviation of 0.1. For asymmetrical folds, a normal distribution with a mean of 0.5 and standard deviation of 0.2 covers the range of expected fold shapes. However, these parameters can be changed or other likelihoods functions used if the geologist has more specific knowledge about the fold asymmetry. In theory, the asymmetry ratio could be calculated from outcrop observations of smaller scale asymmetrical folds however this would need to be validated on natural folds.

5.4.4 Fold wavelength

In some cases, the data may not capture the full wavelength of the main fold geometry. For example, outcrops may only constrain the geometry of a single limb of the fold or only sample a single hinge without crossing the point of inflections. In these cases, the geologist could incorporate additional information into the geological inversion, where the wavelength could be constrained by wavelength values from surrounding areas or the wavelength could be constrained from other data such as interpretation of magnetic or gravity potential field datasets. The prior distribution can either be defined by a standard PDF where the distribution parameters are specified by the geomodeler (*e.g.* for a Gaussian distribution: mean and standard deviation), or by estimating the PDF from samples (*e.g.* wavelength of folds from outside of the model area associated with the same deformation event) using Kernel Density Estimation (KDE).

5.4.5 Interpretations: form lines and axial traces

Form lines represent the trace of a foliation on the map surface and can either represent a direct observation of a geological feature or a combination of observation, interpretation and geological experience. Generally, there is no explicit 3D information recorded with the form lines, but it is possible to calculate the fold limb rotation angle for form lines using the geometrical relationship between the fold axis and the folded foliation. The orientation of the folded geological surface is orthogonal to both the tangent of the form line and the fold axis and can be calculated by finding the vector product between the two normalised vectors representing fold axis and the tangent to form line. The fold rotation angle can then be calculated for orientation measurements as detailed in Grose et al. (2017a). This knowledge can be incorporated into the geological inversion in the same way as orientation observations using a Gaussian likelihood function with an uninformative hyperparameter (Jeffrey's prior) representing the misfit between the observation and the model (Grose et al., 2017b).

Fold axial traces represent the location of fold hinges and could be incorporated as additional data points constraining the fold rotation angle to be 0° at that location. However, this approach does not capture the uncertainty associated with what these observations represent. A fold hinge has a fold limb rotation of 0° and the uncertainty is associated with location of the fold hinge. The true meaning of these observations can be incorporated in the geological inversion using a separate likelihood function assessing the location of the closest fold hinge associated with the fold parameters. The likelihood is calculated using a Gaussian distribution where the mean is the axial trace fold frame coordinate value and the standard deviation is represented by Jeffrey's prior. If two fold hinges are within half of the wavelength of the axial trace constraint this is geologically unlikely and returns a minimum probability.

5.4.6 Data polarity and younging

Structural observations generally represent the unsigned orientation of the structural feature. For example, bedding observations represent the surface trend of lithological contacts, and foliation observations represent the orientation of the axial foliation at a location, however, the surface normal (younging direction) can also be recorded. There is no equivalent to younging directions for foliations and the normal to the surface cannot be related back to any observable structural information. The polarity of the observations can be adjusted by the geologist to give the most reasonable fold geometry, in most cases, this is adequate however it does introduce some additional subjectivity into the model building process. It is possible to incorporate this into the geological inversion by modifying the Fourier series model.

The fold rotation angles ($\hat{\alpha}$) can be corrected using a factor j_i that follows a discrete uniform distribution with possible values of $[-1, 1]$:

$$\hat{\alpha}^* = \hat{\alpha} \cdot j_i \quad (5.3)$$

This approach allows for data to be corrected using an objective function integrated into the geological inversion, reducing the potential for uncertainty and bias to be introduced into the modeling during data correction and outlier identification.

5.5 Results

5.5.1 1D proof of concept examples

In Fig. 5.3 the reference fold is a parasitic fold train that is only sampled in a single limb of the main fold. In this example, there is only a quarter wavelength of the main fold that is captured in the data and the main fold wavelength cannot be identified using the S-Variogram (Fig. 5.3C). The geological inversion captures the main high-frequency features in the S-Plot associated with the parasitic folds but does not capture the main fold wavelength (Fig. 5.3E). The interpolated fold geometry using the fold constraints with only a single wavelength prior (Fig. 5.3D) is unsatisfactory and only captures the smaller parasitic folds. While the resulting 3D model may fit the structural observations, it would not fit the geologist's interpretation (which may be based on geological knowledge). Additional prior knowledge of the main fold wavelength can be incorporated using an informed prior distribution. For example, in Fig. 5.3G, H geological knowledge is incorporated using a prior distribution for an additional wavelength with a mean of $180m$ (an overestimation of the true fold wavelength) and standard deviation of $60m$. The posterior distribution of the main fold wavelength is slightly overestimated and the variability increases away from the structural observations. This could be reduced by using a more informative (smaller standard deviation) prior distribution. The inversion results also show an asymmetry in the main fold that is not seen in the reference model. The asymmetry of the large fold could be corrected using a fold symmetry likelihood function if geological knowledge suggests that the folding is symmetrical.

Fig. 5.4 contains 1D examples using the different geological likelihood functions. The reference fold is a sinusoidal curve with a wavelength of $150m$ and two data points are used. In all examples, the S-Plot curve for the reference fold is shown by the solid blue line in the plots on the left, with the data points (black circles) and the geological knowledge likelihood functions. The fold wavelength is constrained by an informed prior distribution with a mean of $150m$ and standard deviation of $50m$. In the first example (Fig. 5.4A1), geological knowledge is used to constrain the location of the fold hinges. The axial trace

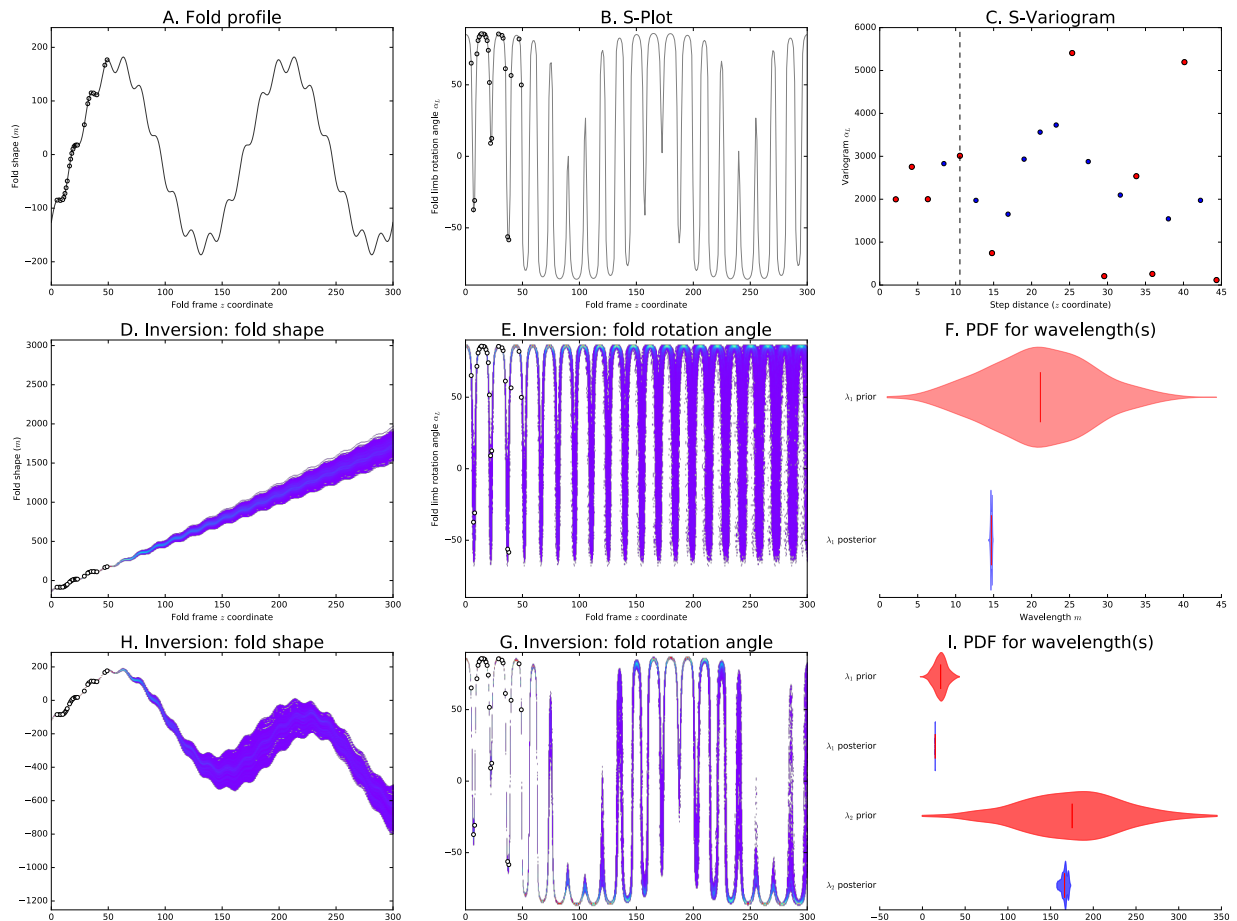


Figure 5.3: 1D parasitic fold shape with observations from a single fold limb: A: Reference parasitic fold shape sampled from only one fold limb. B: S-Plot showing reference fold rotation angle and sample locations. C: S-Variogram where only one fold wavelength is identified. D: Interpolated fold shape using only the single identified wavelength. E: Interpolated fold rotation angle. F: Violin plot showing wavelength prior and posterior distributions for (D) and (E). G: Interpolated fold shape using prior knowledge about larger wavelength folding. H: Interpolated fold rotation angle using prior knowledge about larger wavelength folding. I: Violin plot showing the prior and posterior distributions for the two fold wavelengths. Prior distribution for λ_2 represents additional geological knowledge.

locations (red dots) have been intentionally offset from the true fold hinge location to simulate possible uncertainties. Fig. 5.4A2 shows the resulting fold rotation angle curves when only knowledge about the axial trace location and the fold symmetry are included in the inversion. There is a large range in the sampled fold geometries with significant variability in the tightness of the folds (seen in the range of the fold rotation angle for the inversion). This can be addressed by including additional knowledge about the fold tightness in the inversion and results in a more concentrated posterior distribution (Fig. 5.4A3). In both of these examples, there is enough information in the two orientation observations to constrain the type of observed fold hinge (*i.e.* the slope of the S-Plot curve determines if the fold hinge is synformal or antiformal). However, if these points were closer together, the folding less tight or no observations available the interpolated geometry should have an equal probability for synformal or antiformal hinges. In most practical cases, axial trace data usually contains some information about whether the fold hinge is synformal or antiformal and this could be included using vergence constraints.

In Fig. 5.4B1 structural vergence is known in five locations within the model area, shown by the arrows indicating the sign of the fold rotation angle. The inversion in Fig. 5.4B2 only uses structural vergence and fold symmetry knowledge. The resulting fold shapes have a similar wavelength as the reference model

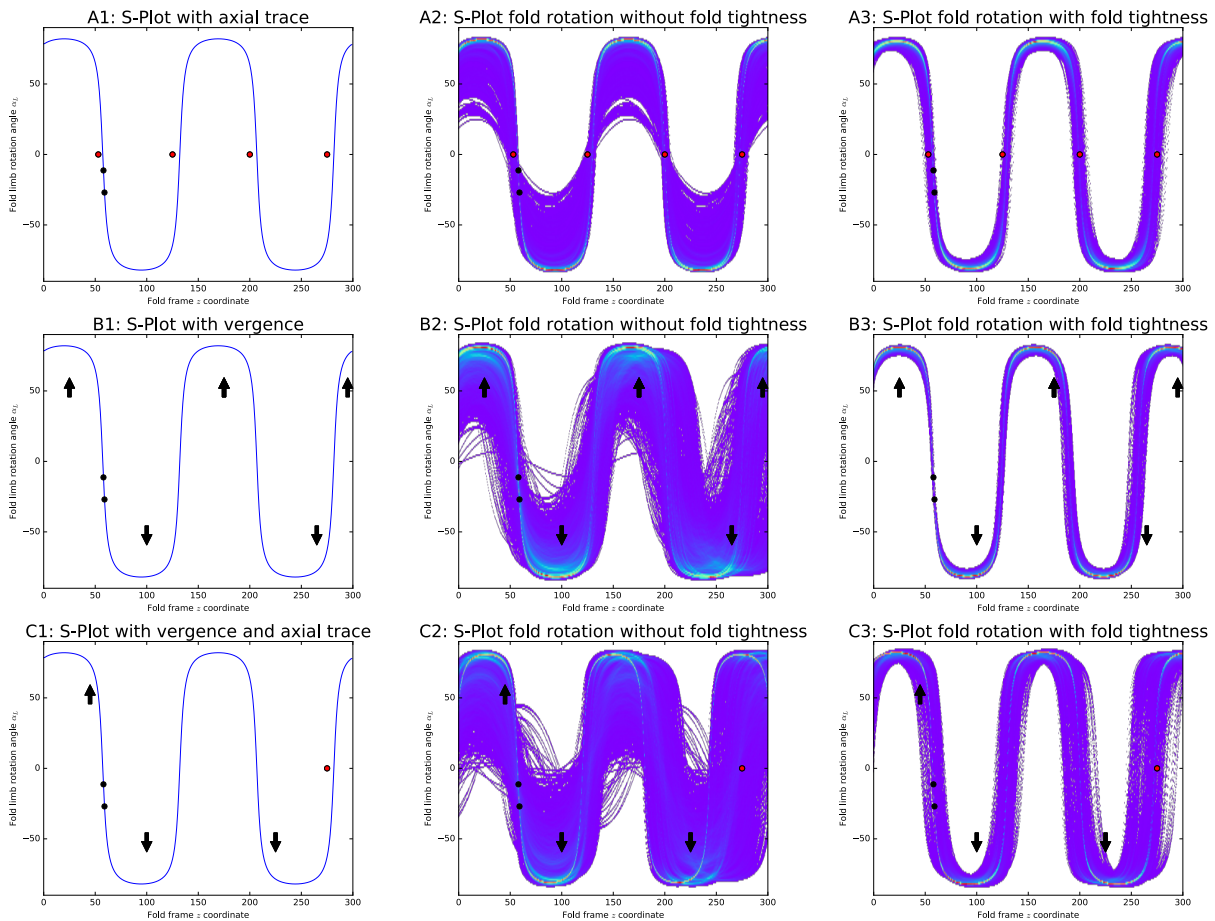


Figure 5.4: Synthetic 1D examples demonstrating different geological knowledge likelihood functions. A1: Reference S-Plot showing axial trace locations (red dots) and two surface orientation constraints (black dots). A2: Simulated fold rotation angles using data, axial trace, and asymmetry likelihoods. A3: Using the same constraints as (A2) and interlimb angle likelihood. B1: Reference S-Plot showing vergence observation location (black arrows) and two surface orientation constraints (black dots). B2: Simulated fold rotation angles using data, vergence and asymmetry likelihoods. B3: Using the same constraints as (B2) and interlimb angle likelihood. C1: Reference S-Plot showing axial trace location (red dots), vergence constraints black arrows and two surface orientation constraints (black dots). C2: Simulated fold rotation angles using data, axial trace, vergence and asymmetry likelihoods. C3: Using the same constraints as (C2) and interlimb angle likelihood.

with some variability in the hinge locations particularly away from the data locations (*e.g.* $z > 200$). There is a wide range of fold tightness with folds ranging from close to isoclinal. When additional knowledge is used to constrain the fold tightness, the variability in the hinge locations is reduced (Fig. 5.4B3). The inversion results show a wavelength that is underestimated in comparison to the reference model, however, the inversion results are consistent with the geological knowledge. Additional knowledge constraining the wavelength of the folds or the location of fold hinges could be included to reduce this variability.

In Fig. 5.4C1 there are two vergence observations near the data points and an axial trace observation near the fold hinge where $z > 250m$. There are three fold hinges that are not captured by the geological knowledge or observations. Fig. 5.4C2 shows the resulting inversion where no knowledge about fold tightness is included. The inversion results show that the fold geometry is not well constrained using only this geological knowledge. The fold tightness contributes significantly to the variability with fold geometries ranging from open to close. In Fig. 5.4C3 the additional knowledge of the fold tightness significantly reduces the variability in the fold geometries. The fold tightness constraint not only reduces the range of the interpolated fold tightness but also makes the resulting fold wavelength more consistent to the reference

model. This indicates that knowledge related to the fold tightness is very important in constraining the resulting geometries.

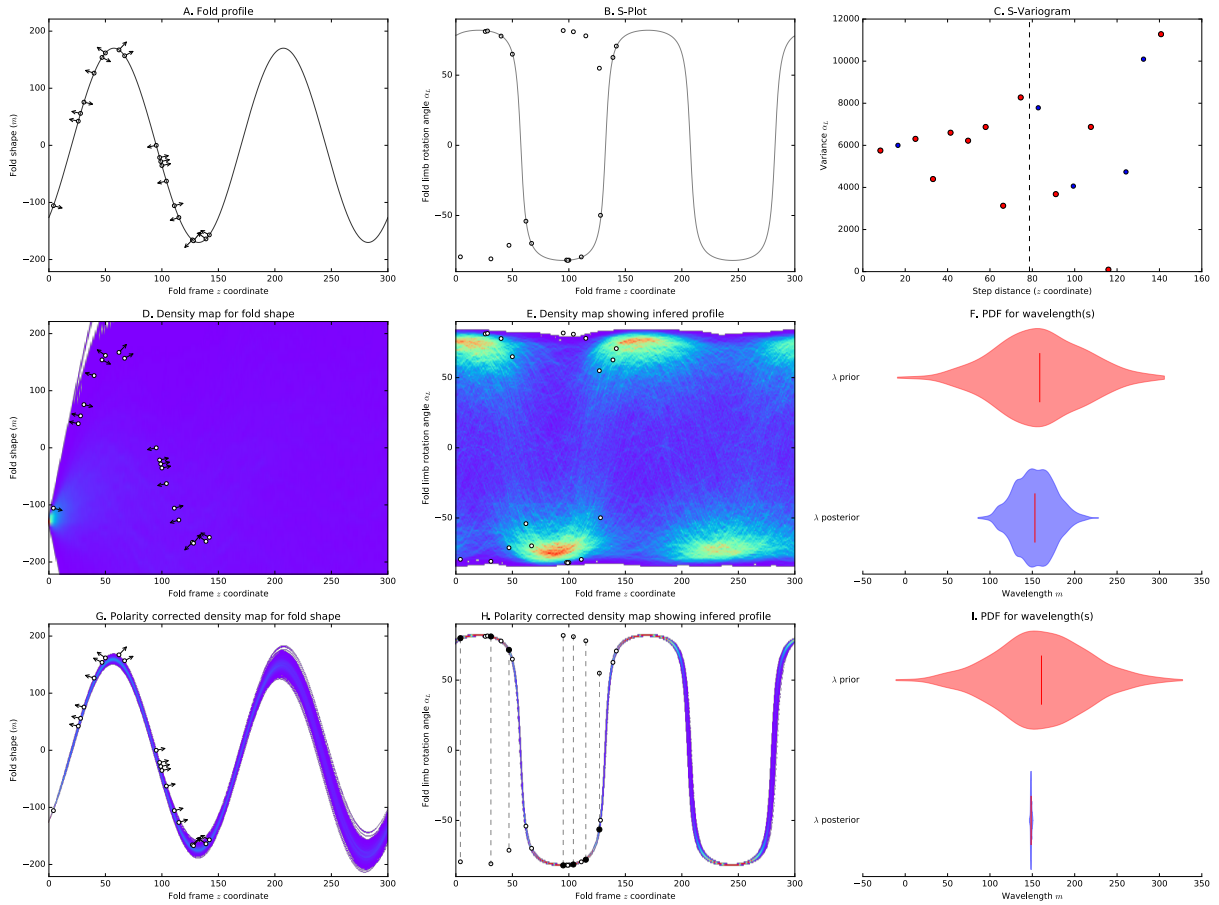


Figure 5.5: A: Reference fold shape of a sinusoidal fold with inconsistent polarity shown by the direction of the arrows located at the observations. B: Fold rotation angle reference curve and the calculated rotation angle showing the effect of polarity on the sign of the calculated rotation angle. C: S-Variogram showing a high nugget effect due to the incorrect polarity for 7 observations. The dashed line indicates the estimated fold wavelength. D: Interpolated fold shape without polarity correction. E: Interpolated fold rotation curve without polarity correction. F: Violin plot showing wavelength prior and posterior for (D) and (E). G: Interpolated fold shape showing corrected polarity using Eq. (5.3), observation polarity has been corrected. H: Interpolated fold rotation curve using Eq. (5.3), dashed lines show the data points that have been corrected and the black dots indicate the corrected fold rotation values. I: Violin plot showing the wavelength prior and posterior distributions for (G) and (H).

In all of the previous examples, the polarity of the orientation data has been consistent, in Fig. 5.5 the polarity of 35% of the data has been reversed. This is indicated by the direction of the arrows in Fig. 5.5A. The observations with reversed polarity do not fall on the reference curve for the fold rotation angle (Fig. 5.5B). The wavelength of the fold is usually estimated by finding the local maximum of the S-Variogram (Grose et al., 2017a,b). In this example, the S-Variogram has a large nugget effect which suggests that there is low correlation between close data points Fig. 5.5C). This is because the sign of the calculated fold rotation angle changes with the polarity meaning that the correlation between two data points with inconsistent polarity would be low. In this case, the wavelength was able to be estimated to be $\sim 160m$, in some cases, for example where too many data points have inconsistent polarity it may not be possible to use the S-Variogram to estimate the wavelength. In these cases, the wavelength could either be defined using geological knowledge using an informative prior or the S-Variogram could be calculated using the absolute value of the fold rotation angle. When the absolute value of the fold rotation angle is used, the local

maximum would correlate with the quarter wavelength of the fold. Fig. 5.5D and E show the interpolated fold shape and fold rotation angles where the polarity is assumed to be correct. The posterior distribution of the wavelength is consistent with the reference geometry (150m). However, there is significant variability associated with the fold geometry. When the polarity is incorporated into the inversion using Eq. (5.3) all of the observations with incorrect polarity are identified and the interpolated fold shape and fold profile (Fig. 5.5G, H) match the reference model.

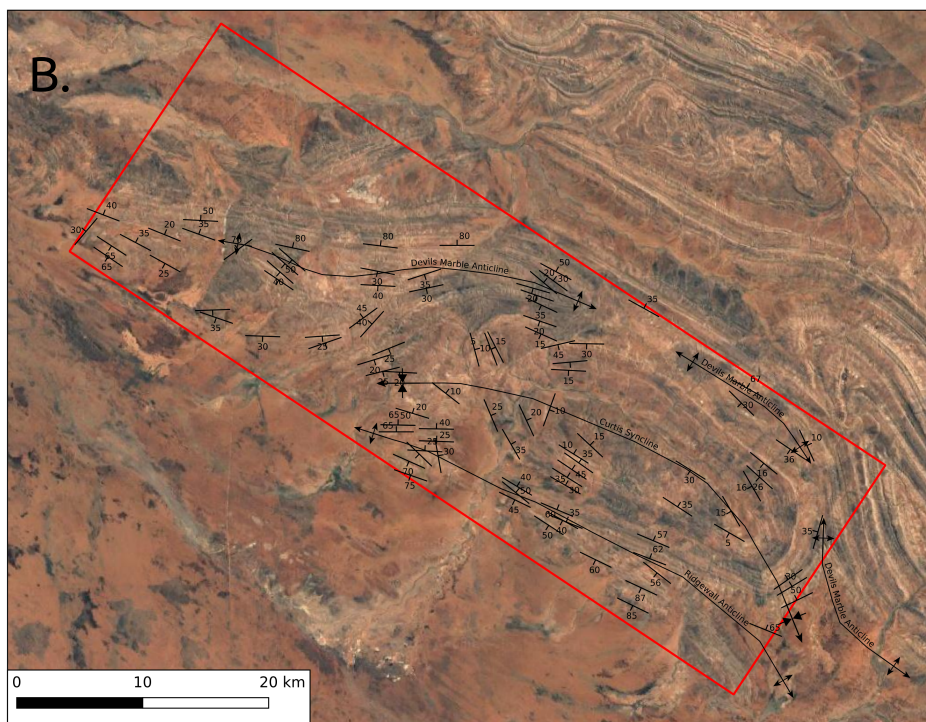
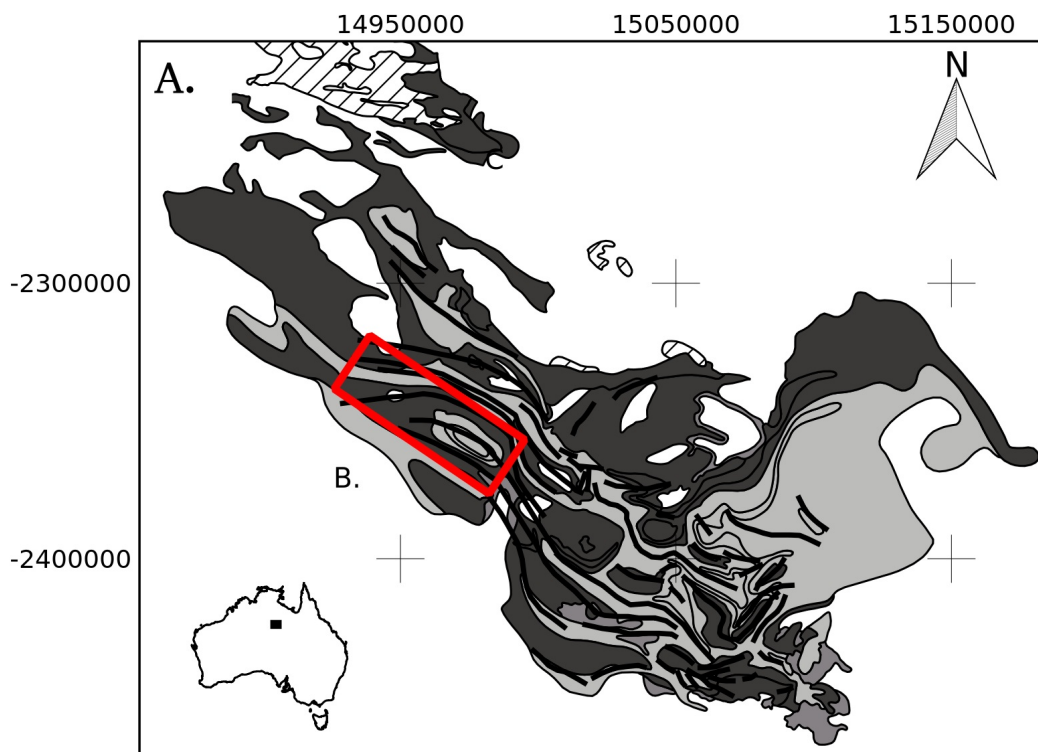
5.5.2 Case study: Davenport Province

In the final example, we demonstrate an inversion of geological observations and knowledge using a case study from the Davenport Province, a poly-deformed fold belt in the Northern Territory, Australia. It is a well exposed Proterozoic terrain where mainly sedimentary packages have been folded to form a Type 1 interference pattern during the Barramundi Orogeny (Blake and Page, 1988). Fig. 5.6A shows the location of the Davenport Province, in Northern Australia and a simplified geological map showing the main fold axial traces and stratigraphic units.

The model area (Fig. 5.6B) contains three major north west- south east trending doubly plunging folds: the Devils Marbles anticline (north), Curtis syncline and the Ridgewall anticline (south). The structural observations have been digitized from the publicly available Bonney Well map sheet. The folds have a half wavelength of approximately 7km and can be clearly seen in the aerial imagery (Fig. 5.6B). Only the orientation of bedding has been recorded and there are no direct observations of the fold axis or axial foliations. The associated cross section suggests that the folding is upright and we use this interpretation to constrain the geometry of the axial foliation with the interpreted axial trace locations.

The orientation of the axial foliation has not been recorded, this means that an appropriate assumption is to describe the observed fold geometry as a Type 1 interference pattern as suggested by Blake and Page (1988). Type 1 fold interference patterns can be represented with a single fold frame where the z coordinate is aligned at best with the axial traces of the north west-south east folds and the y coordinate is interpolated to align with the axial trace of the north east-south west folds. If two fold frames were to be used, the z and y coordinates for the two folding events would be close to parallel. This does make the assumption that the axial surface of the older fold is not folded by the younger folding event. The interpolated scalar fields for the fold frame y and z coordinates are shown in Fig. 5.7. We use the assumption that the folding is similar class meaning that the x coordinate does not need to be interpolated. To constrain the orientation of the fold axis Grose et al. (2017a) use the intersection of the z coordinate isosurfaces and orientation of the folded foliation. However, because the fold frame has not been constrained with field observations this technique results in the calculated fold axis rotation angle being very inconsistent (Fig. 5.8A). For example, the calculated fold axis rotation angle for $y = -30,000$ is between -40° and 10° .

Using the aerial imagery and the interpolated fold frame it is possible to infer the fold hinge line vergence and use this to constrain the fold axis rotation angle. The orientation of bedding in the fold hinge can be used to determine the geometry of the fold axis. For example, the Devils marble antiform plunges shallowly east and e_y is oriented to the east suggesting the fold axis rotation angle should be negative in this area. Most of the observations in the hinge of the fold suggest a shallowly plunging fold where the dip of bedding is about 30° . The dip seems to be consistent on each fold hinge which suggests that the fold axis is symmetrically folded and would have an equivalent fold axis rotation angle range to a gentle fold shape (Table 5.1). These observations can be included in the fold geometry inversion using fold symmetry and



- | | | | |
|---|--|------|------------------------|
| — | Fold axial trace | — | Orientation of bedding |
| ■ | Arumbera Sandstone | ↕↕↕↕ | Antiform axial trace |
| ■ | Lower Hatches Creek Group and Flynn Subgroup | ↔↔↔↔ | Synform axial trace |
| ■ | Upper Hatches Creek Group | ▭ | Model area |
| ▨ | Warramunga Formation | | |

Figure 5.6: A. Simplified geological map showing the Proterozoic rocks from the Davenport Province. B. Structural map for study area

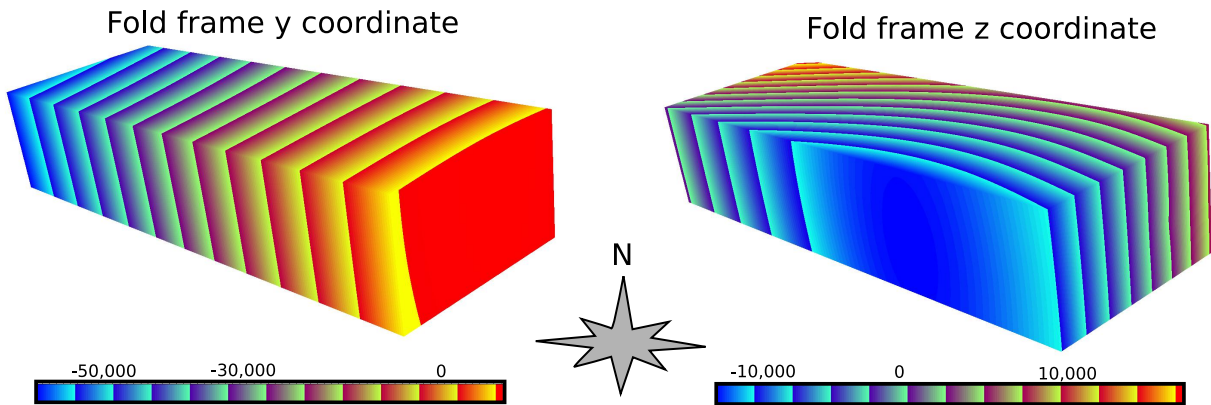


Figure 5.7: Interpolated volumes showing the y and z fold frame coordinates

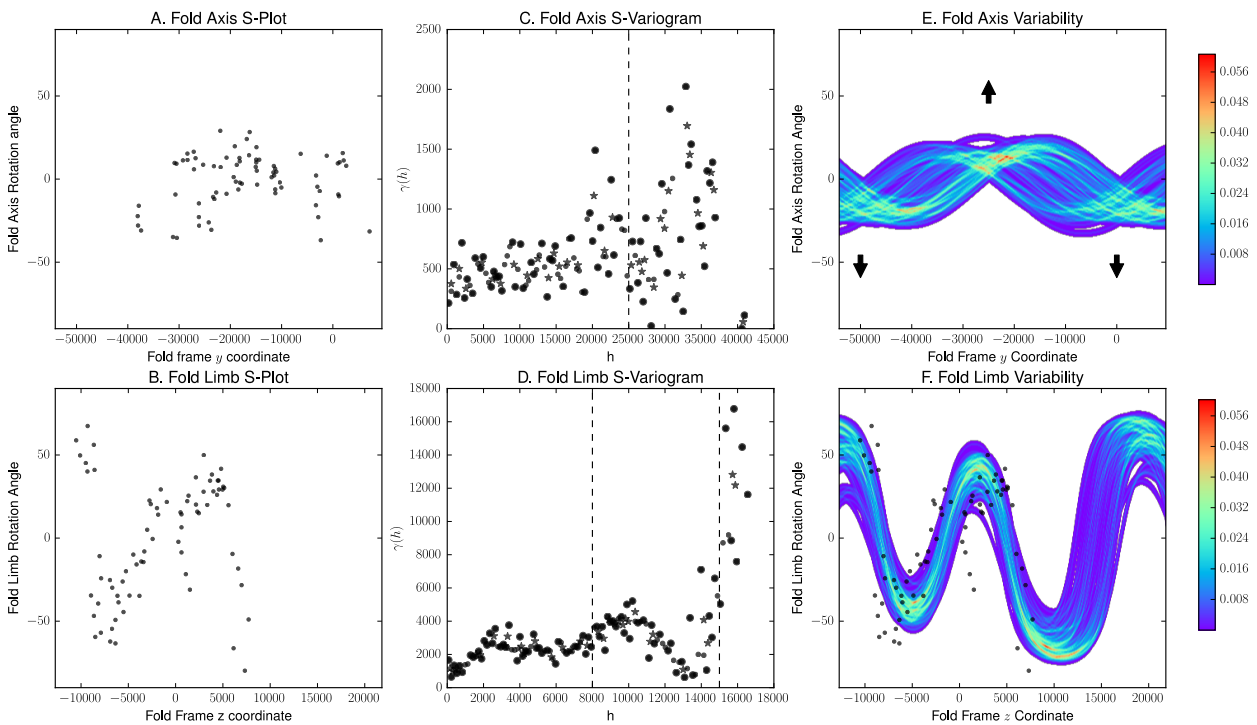
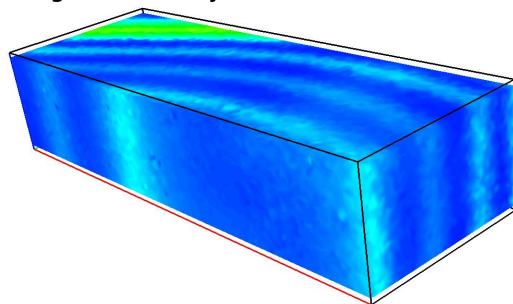


Figure 5.8: A. S-Plot of fold axis rotation angle. B. Fold axis S-Variogram. C. Interpolated fold axis rotation angle. D. Fold limb rotation angle S-plot. E. Fold limb rotation angle S-Variogram. F. Interpolated fold limb rotation angle.

fold hinge angle likelihood function. The fold limb rotation angle is well constrained by the observations of bedding. This is incorporated into the inversion using the geological knowledge likelihood functions to constrain the fold axis geometry to be symmetrical with a range in the fold axis rotation angle of 60° and three hinge-line vergence constraints inferred from the analysis of the aerial photography and structural observations. The half wavelength of the fold axis is constrained by measuring the average distance between plunging fold hinges, of approximately 50km. The joint posterior distribution for the fold axis rotation angle and fold limb rotation angle is shown in Fig. 5.8E and F. The variability between the profiles increases away from the data for the fold limb rotation angle, suggesting high uncertainty, where the z coordinate is greater than 5,000m.

A. Angle variability model volume



B. Angle variability model slices

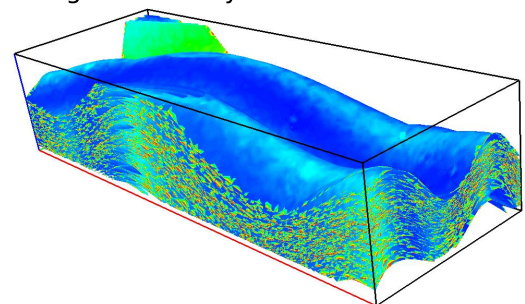


Figure 5.9: A. Geometrical variability between 100 interpolated models. B. Surface from 100 models painted with angle variability indicating the consistency of the modeling to the observed structural features.

Fig. 5.9A shows the geometrical variability in the inversion results with the highest variability being associated with the north west- south east folding. There is also variability associated with the interpolated fold axis that can be seen by the change in angle variability along the interpolated fold hinge locations. The interpolated surfaces all capture the main geometries of the observed map pattern. The highest location of variability is associated with the fold north of the Devils Marble anticline. The interpolated surfaces are all very steeply dipping approaching vertical. This is in agreement with the recorded orientation of bedding which is consistently dipping 80° . The geological interpretation in the cross section suggests a more open fold geometry with less steeply dipping limbs.

In Fig. 5.10B the frequency of form lines corresponding to a single isosurface for all 200 inversion realisations are shown by a scaled colour map. The areas with higher frequency correspond with the locations where the geometry is more consistent between inversion realisations. The axial traces of the major folds highlights that the main structural features observed in the aerial photography are captured by the geological inversion (Fig. 5.10A). For example, the basin associated with the Curtis syncline is highlighted by the absence of any form lines. Areas of high variability between the interpolated form lines, such as the location of the syncline to the north of the Devils Marble anticline present targets for additional data collection.

5.6 Discussion

3D geological models are constructed using available geological observations that directly constrain the surfaces being modeled. Geological knowledge has usually been incorporated into the modeling process by

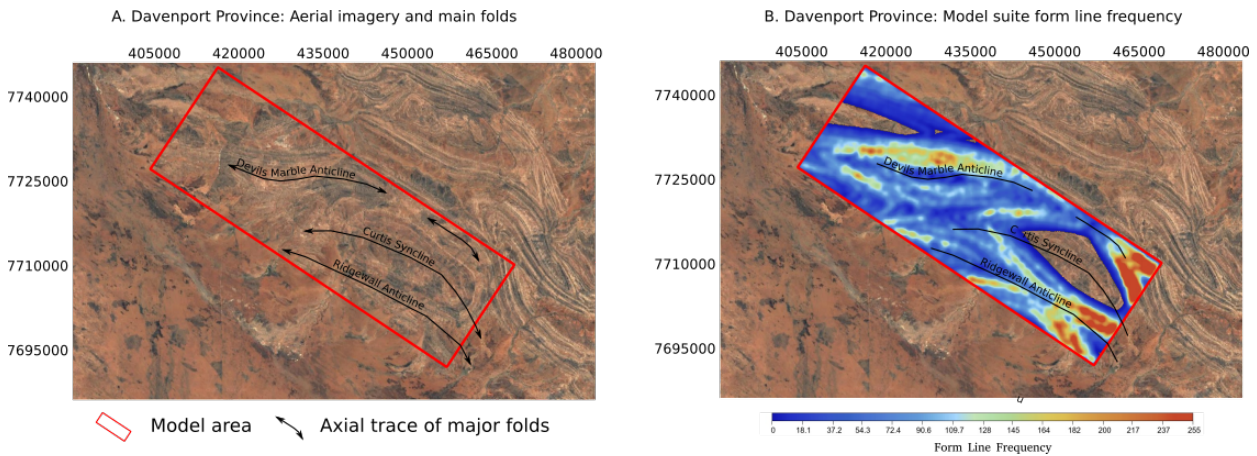


Figure 5.10: Resulting geological for single isosurface from inversion results showing fold geometries overlain on aerial imagery.

the geologist first interpreting the resulting geometry and adding in interpretive constraints (Jessell et al., 2014, 2010; Maxelon et al., 2009). In this contribution, we have used the flexibility of Bayesian inference to combine both geological data and knowledge into a geological inversion scheme (Grose et al., 2017b). The addition of these constraints can significantly reduce the range of fold geometries specifically where geological data is sparse or ambiguous (*e.g.* Fig. 5.4). In all of the examples, the fold tightness constraint significantly reduces the variability between the inversion realisations. This is an expected result as the majority of the observed variability between fold geometries was in the inferred tightness. This constraint could be applied by upscaling tightness observed at an outcrop scale to the geometry of the folds being modeled.

The fold axis geometry is an important part of the fold modeling workflow and often only limited observations are recorded on geological maps. It is important that the fold axis is consistent with the structural observations and the geologist's knowledge because the fold limb rotation angle is calculated in the plane normal to the fold axis (Grose et al., 2017a,b). Where the geometry becomes more complicated and there is more uncertainty in structural observations, calculating the intersection between the interpolated z coordinate and folded foliation does not provide a good constraint for the geometry of the fold axis (*e.g.* Fig. 5.8A). This will result in fold geometries that are much more extreme than the observed folding. In Fig. 5.8E and F the joint posterior distribution was sampled using only the geological knowledge likelihood functions for the fold axis and the data points for the fold limb rotation angle. It is possible that the best fitting model for both observations and knowledge would not be produced without directly using geological knowledge within the inversion scheme. This becomes even more important if form lines are used to calculate the fold limb rotation angle because there is no 3D information in the form line the best solution for the fold axis minimises the range in fold limb rotation angle.

There have been a number of studies investigating uncertainties in geological interpretations (*e.g.* Bond et al., 2007a, 2011, 2015; Torvela and Bond, 2011). These studies have been primarily focused on the interpretation of seismic datasets and have provided interesting insight into the role of experience and expertise in geological interpretation. Bond et al. (2007a) identified factors associated with geological interpretation that are applicable across other fields of geosciences. In their study, Bond et al. (2007a) used a cohort of geologist with skill levels ranging from experienced geologists with 15+ years experience to students 0-5 years experiences. All participants were given a synthetic seismic section and given no regional context, meaning that the tectonic setting had to be derived from observations in the seismic data. The experienced

geologists were as likely to interpret the incorrect tectonic setting as the students. They also recorded the type of tectonic setting(s) that each participant felt they were an expert in. All of the cohorts were shown to exhibit availability bias where they were more likely to interpret the tectonic setting they had the most experience with. This observation is consistent with Frodeman (1995)'s interpretation of geology as a historical science, where analogies are an important part of geological reasoning. For seismic interpretation, the geologist may use the structural style they are familiar with as an analogy for the interpretation area. Anchoring bias also affected the interpretations across the cohort where the interpreters expected to see a particular structure for a given setting. Similarly, the interpreters were seeking confirmation for their interpretations by asking the geographical location, to infer the broad tectonic setting of the study area. These observations by Bond et al. (2007a) suggest that the interpretive aspect of geology plays a significant role throughout the interpretation of geological datasets. In a structural mapping context, these results suggest that while mapping, the geologist's current interpretation plays a significant role guiding both outcrop interpretation and often in identifying the next location to map.

Jones et al. (2004) argue that advances in digital field mapping could allow for the separation of interpretation from raw field data. This could use geological uncertainties associated with individual data and/or interpretations as the input to produce an overall estimate of the uncertainty associated with a given model. This would allow for alternative interpretations to be modeled simultaneously, during mapping and ultimately would guide the geologist in the collection of data. Fig. 5.10B shows how the inversion framework presented in this paper could be used for real-time geological mapping. In this example, a single contact has been interpolated and the outcrop pattern used as a proxy for model variability. Areas of high variability are associated with the fold geometries and can be used to help target additional data for reducing the geological variability. Additionally, producing a 3D realisation of geological structures during field mapping would allow for more structured data collection by targeting areas with higher variability or structures conflicting with the geologist's hypothesis. In the Davenport Province model, there is more uncertainty associated with the fold hinges in the north-western area of the model. This suggested that more data could be collected to either better constrain the orientation of the folded surface or to better constrain the orientation of the axial foliation. Building 3D models while collecting data would be advantageous because the geologist's knowledge would be used to falsify possible models, effectively being an additional likelihood function for the model. This means that the geologist's expertise can be applied to assessing how well the interpretation fits the observations rather than producing a single best fit model (Jessell et al., 2010; Wijns et al., 2003). While it will never be possible to completely remove the subjectivity from geological studies, moving towards a quantitative interpretation approach should reduce the impact of bias on geological reasoning as multiple possible interpretations are presented to the geologist rather than the geologist generally trying to falsify a single interpretation. The application to Davenport Province has demonstrated that the method can be successfully applied to a polydeformed structure. In this case study, there was insufficient data constraining the geometry of the axial foliation. Additional observations would allow for multiple fold events to be inverted and would result in a much better representation of the geological structures. Applying our inversion framework during geological mapping would allow for geologists to test how different interpretations fit the observations rather than trying to identify the best interpretation.

A common approach for trying to reduce geological ambiguity/uncertainty is the use of geophysical inversions to help understand the geometry and distribution of subsurface geology (e.g. Armit et al., 2014; Blaikie et al., 2014; Fullagar et al., 2004; Guillen et al., 2008; McLean et al., 2008). Prior geological

knowledge (*e.g.* an existing 3D model) can be used to perform a constrained inversion. The geometry, density and/or magnetic susceptibility of the rock units are then stochastically varied in order to reduce the misfit between the inversion and observed geophysics. However, these inversion approaches typically do not maintain any geological meaning when producing the inversion (Jessell et al., 2010). Lindsay et al. (2013a,b) and Giraud et al. (2017) use the resulting model suite from uncertainty simulations to constrain the geophysical inversion. This approach considers the geologically possible models prior to trying to use the geophysical observations. Giraud et al. (2017) create a probabilistic representation of the stratigraphy and use this as a priori information for the constrained geophysical inversion. A true joint geological and geophysical inversion would combine the sampling of the posterior distribution to sample using both geological likelihood functions and geophysical likelihood functions (Jessell et al., 2010). It would be expected that the posterior distribution of possible models considering geophysical and geological observations will be different to the posterior distribution of either property independently. In much the same way as adding in additional knowledge reduces the variability in the interpolated fold shapes, adding geophysical data provides a means of falsifying models that cannot fit the geophysical observations. This approach has not been previously feasible because 3D modeling schemes have been unable to predict the full range of geological observations. However, using the recent developments in fold modeling (Grose et al., 2017a,b; Laurent et al., 2016) and this paper, as well as methods for simulating fault networks (Cherpeau and Caumon, 2015; Cherpeau et al., 2012) and incorporate knowledge related to fault geometries (de la Varga and Wellmann, 2016; Laurent et al., 2013) a joint geological and geophysical inversion becomes more feasible.

5.7 Conclusion

New geological likelihood functions are proposed for integrating additional geological data and knowledge into an inversion scheme for fold geometries. Geological knowledge is incorporated directly into the interpolation scheme using Bayesian inference. This allows for poorly constrained features such as the fold axes to be modeled with minimal hard data and still produce results consistent with the geological interpretation. The incorporation of geological knowledge directly into the interpolation scheme could form the basis of a real-time geological inversion that could be used to help to address the ambiguity in geological interpretations. This would allow for information about geological uncertainties to propagate while mapping and allow for different structural interpretations to be rapidly tested for targeted data collection.

Our geological inversion scheme is unique because it uses the geological observations to falsify possible structural models built from a parameterised description of the fold geometry using prior geological knowledge. Instead of using observations to infer a single best model or a suite of models based on observation uncertainties. We believe that this is not only a more rigorous way of sampling the geologically possible models but also allows for a true joint geological and geophysical inversion.

Acknowledgements

This research was partially funded by Australian Research Council Linkage grant LP140100267, and partly supported by the “Investissements d’avenir” Labex RESSOURCES21 (ANR-10-LABX-21-01). The authors are grateful to the industrial and academic sponsors of the Gocad Research Consortium managed by ASGA (Association Scientifique pour la Géologie et ses Applications, <http://ring.georesources.univ->

lorraine.fr/) for their support. We thank Paradigm for providing the GOCAD-SKUA software and API. The final case study in this publication was generated with the StructuralFactory plugin for Gocad, based on RING's StructuralLab plugin.

Chapter 6

Discussion and conclusion

6.1 Introduction and thesis summary

The aim of this study was to define a new method for characterising the geometry and uncertainty of folded surfaces in three dimensions from sparse field observations and geological knowledge. This was achieved by introducing a framework for incorporating folds into implicit modeling schemes allowing for multiple fold events to be characterised. This approach uses the overprinting relationships between observed foliations associated with folding to determine the relative timing of folding events. Each folding event is modeled backwards in time starting with the most recent. A fold frame is built for each folding event to capture the geometry of the structural elements of the fold: fold axis, axial surface and vergence. Two rotation angles are defined: the fold axis rotation angle defines the local geometry of the fold axis and the fold limb rotation angle defines the fold shape. The rotation angles are combined with the fold frame determine the local orientation of the folded surface throughout the model.

The fold frame coordinates are aligned so that one coordinate measures the distance from a reference fold hinge in the direction orthogonal to the axial surface and another coordinate measures the distance along the axial surface. The fold rotation angles can be calculated from observations of the folded foliation/surface or fold axis/intersection lineation. A cross plot of the fold frame coordinate, and the associated fold rotation angle defines the geometry of the fold axis along the axial surface and another cross plot defines the geometry of the fold shape looking along the fold axis. The wavelength of folding can be identified using a sample semi-variogram in the fold frame coordinates, and, where multiple folds are captured, the regularity of the wavelength between adjacent fold hinges can be tested. Two interpolation methods are presented to produce a forward model of the fold geometry: (1) Radial Basis Function interpolation is used where the folding is identified as having irregular wavelength between fold hinges, and; (2) a Fourier series where the fold wavelength is regular. The Fourier series produces favourable results where data is sparse or extrapolation is required because it captures the style of folding shown in the data and uses this to interpolate between outcrops or extrapolate away from outcrops.

This forward model is used as a basis for a geological inversion: rather than using the observations as the parameters for a geological interpolation/interpretation, I use the observations to falsify possible models of fold geometries and update the structural parameters that best explain the observations. Both the fold axis and fold shape are inverted at the same time. We demonstrate that this approach can be used to target locations where additional structural data can reduce model uncertainty. The geological inversion uses Bayesian inference to determine the range in parameters and is easily extended to incorporate various types of geological observation and geological knowledge into the inversion. Incorporating geological knowledge directly into the inversion scheme rather than using synthetic data representing the geologist's non-unique interpretation is preferable because the interpretation is subjective. This approach effectively quantifies the interpretation process of the geologist within the geological inversion scheme.

In each of the chapters of this thesis there is a focused discussion for each of the contributions. This chapter aims to discuss issues outside of the scope of these chapters and will address broader discussion topics highlighting the possible applications, limitations and further research direction. The topics for further discussion are:

- Accounting for irregular fold wavelength in the geological inversion
- Incorporating different fold classes
- Geometrical complications of the fold frame coordinates for polydeformation
- Joint geophysical and geological inversions

- Incorporating faults in the modeling framework
- Geological inversion of polydeformed terranes

6.2 Research implications and future research recommendations

6.2.1 Irregular fold wavelength in the geological inversion

In most examples in this study I have suggested that the best description of the fold geometry is to use a periodic function. In chapter 2 I use a modified sinusoidal curve and in chapters 3, 4 and 5 a Fourier series. In chapter 3 an alternative method uses Radial Basis Function (RBF) interpolation where the fold geostatistics determine that enough data exists to characterise the fold geometry and that the folding appears to have irregular wavelengths. This approach is functional for producing a single best fit model, however it does not fit into the geological inversion framework because only a single realisation of the fold rotation angles is produced.

Stochastic simulations for properties values are well covered in geostatistical literature (e.g. Arpat and Caers, 2007; Chilès and Delfiner, 1999; Honarkhah and Caers, 2010; Strebelle, 2002), instead of estimating the mean of the property value, the stochastic simulation will produce multiple equally likely realisations for the observations. These methods generally suffer from the same drawbacks as standard interpolation methods where they are only appropriate if there are no locations being interpolated that are further than a half wavelength of the fold from data points (e.g. Fig. 3.7). However, where sufficient data exists this approach could replace the Fourier series for either the fold axis or fold limb rotation angle. In these cases, it is unlikely that the geological knowledge likelihood functions would be necessary for constraining the fold geometry.

An alternative would be to use a non periodic parametric model for representing the fold rotation angles. For example, the Fourier series could be replaced with a Wavelet transform based approach. Although the use of a Wavelet transform on irregularly spaced points would require interpolation prior/during the Wavelet transform using an iterative approach. This is likely to remove any of the inherent variability in the dataset and is not desirable for model fitting. Wavelet transform is somewhat similar to a Fourier transform in that the aim is to capture the information inside a signal using a linear combination of basis functions. Different wavelets can be chosen usually to capture the shape of the features observed in the signals (Torrence and Compo, 1998). The main difference between the wavelet transform and the Fourier transform is that the Fourier transform is only localised in Frequency and the Wavelet transform is localised in both frequency and time (space) (Torrence and Compo, 1998). This means that periodicity of folding is implicitly assumed when working in the Fourier domain and in the wavelet domain this is not the case. This would result in similar issues to the standard interpolation when extrapolating or interpolating further than the half wavelength of the fold from data points would result in fold geometries that are not consistent with the geologist's interpretation.

However, the Bayesian framework used for the geological inversion in chapter 4 and 5 can easily be adapted for any model representing the fold geometry. The periodic assumption of the Fourier series is probably the most consistent model with the geologist's expectations, where there is not enough data to apply other more localised methods (e.g. Kriging/RBF). It may be beneficial to use an additional polynomial function (similar to that used in RBF interpolation and Kriging for the drift) to remove any global trend from

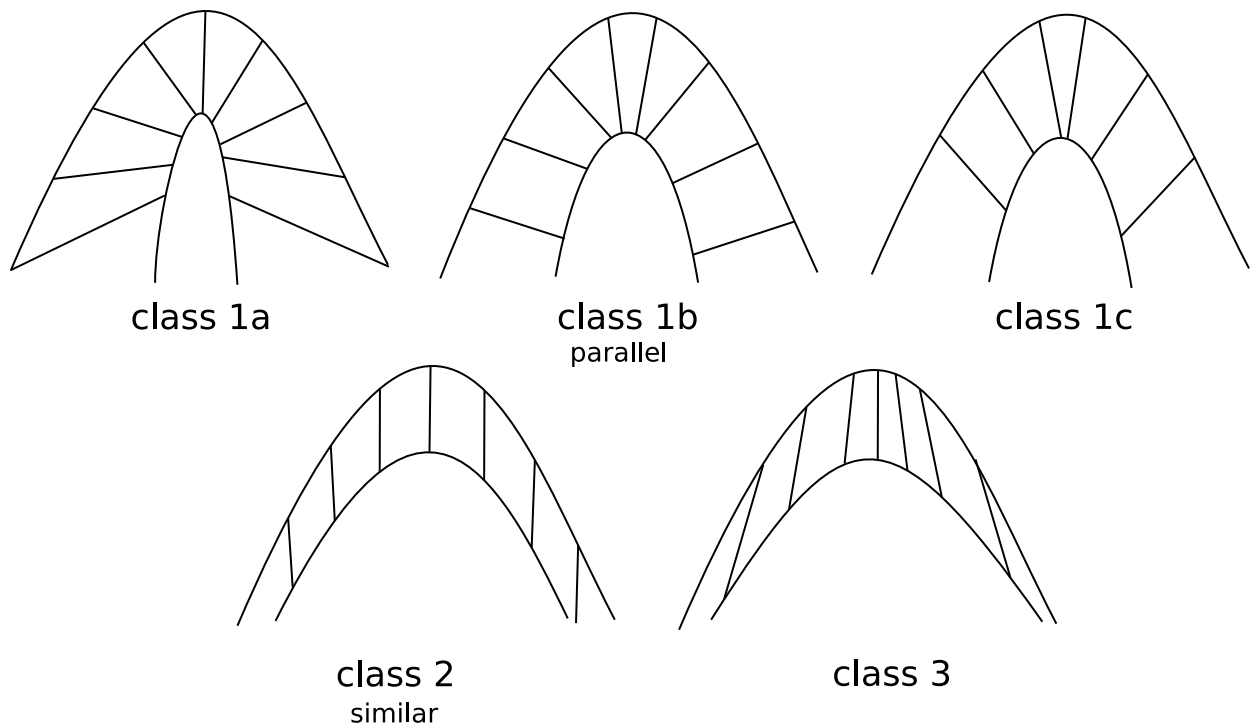


Figure 6.1: Fold classes defined by dip isogons highlighting similar and parallel folds adapted from (Ramsay and Huber, 1987)

the data, although this can also be achieved using a larger wavelength term in the Fourier series (for example the large wavelength in the Davenport Province model, Fig. 5.8).

6.2.2 Fold class

One of the challenges in characterising and analysing the geometry of folds is determining how the geometry of two surfaces that enclose a layer are related (Ramsay and Huber, 1987). The variations in thickness relative to the dip of the surface looking in profile view is used to classify the fold geometry. Dip isogons can be used to characterise the different geometrical relationships between these surfaces. Three main classes of folds can be defined using dip isogons (Ramsay and Huber, 1987, chapter 17) and are shown in Fig. 6.1: Class 1: where the isogons are convergent, Class 2: isogons are parallel, and Class 3: where the isogons are divergent.

Throughout this study I have used the assumption that the best representation of the fold geometry is to assume similar folding. The advantage in assuming similar fold geometry means that the fold shape can be described using only the z and y coordinates of the fold frame. While, observing pure similar or parallel folds is rare in deformed rocks (Ramsay, 1962b), I believe approximating the fold shape with a similar geometry is a good estimation in sparse data examples. It is a similar problem to assuming regular wavelength between fold hinges. These variations can be the result of pre-folding geology, such as rheological differences or layer thickness that are unknown when building the model (Jessell et al., 2014).

In some cases, there may be enough data to constrain the geometry of individual layers. An example of this is seen in the Cape Conran outcrop (Fig. 3.12) where structural data constrains the geometry of multiple contact surfaces. The fold limb rotation angle could be interpolated for both x and z coordinates. This is equivalent to interpolating the fold shape for a profile view of the fold looking along the fold axis. The fold rotation angle would need to be interpolated with an anisotropy aligned with e_x . This approach would,

where sufficient data exists, provide a good method for interpolating the fold limb rotation angle for folds without making an assumption about the fold style.

6.2.3 Building the fold frame

The fold frame has three coordinates (x, y, z) and associated direction vectors (e_x, e_y, e_z) that are used to constrain the geometry of the folded foliation. In this study only y and z have been interpolated because the direction e_x can be calculated from the vector product of e_y and e_z and for similar folds x is not required as the fold geometry is the same for conformable layers. In chapters 3, 4 and 5 only a single fold frame was needed meaning that both y and z have reasonably smooth geometries and were interpolated using standard implicit methods. In chapter 2 a cylindrical fold axis is used and only the z coordinate was interpolated for each folding event. For multiple deformational events, the geometrical requirements of the y coordinate and the associated direction vector e_y cannot be captured using a single scalar field.

Fig. 6.2 shows a series of fold frames for two folding events. The fold frame for the most recent fold (F_2) is built first (Fig. 6.2A,B) and both z and y have been interpolated using standard implicit techniques. The next fold frame for F_1 is built using the fold constraints and the z coordinate is parallel to the axial foliation of the F_1 folds (S_1) shown in Fig. 6.2C. To interpolate the y coordinate I have previously suggested that using the constraint $e_y \cdot e_z = 0$ will build a scalar field that measures the distance along the axial surface of the fold and has a gradient that is aligned with the direction of the fold axis. Fig. 6.2D shows the y coordinate interpolated using this assumption. In Fig. 6.2E there are iso-surfaces from the F_1 y coordinate (vertical surfaces) and the F_1 x coordinate (folded surface). All of the surfaces have been coloured with the distance along the folded surface. For the interpolated y coordinate to be valid, the vertical isosurfaces would have the same distance (colour) for the whole surface, which is not the case.

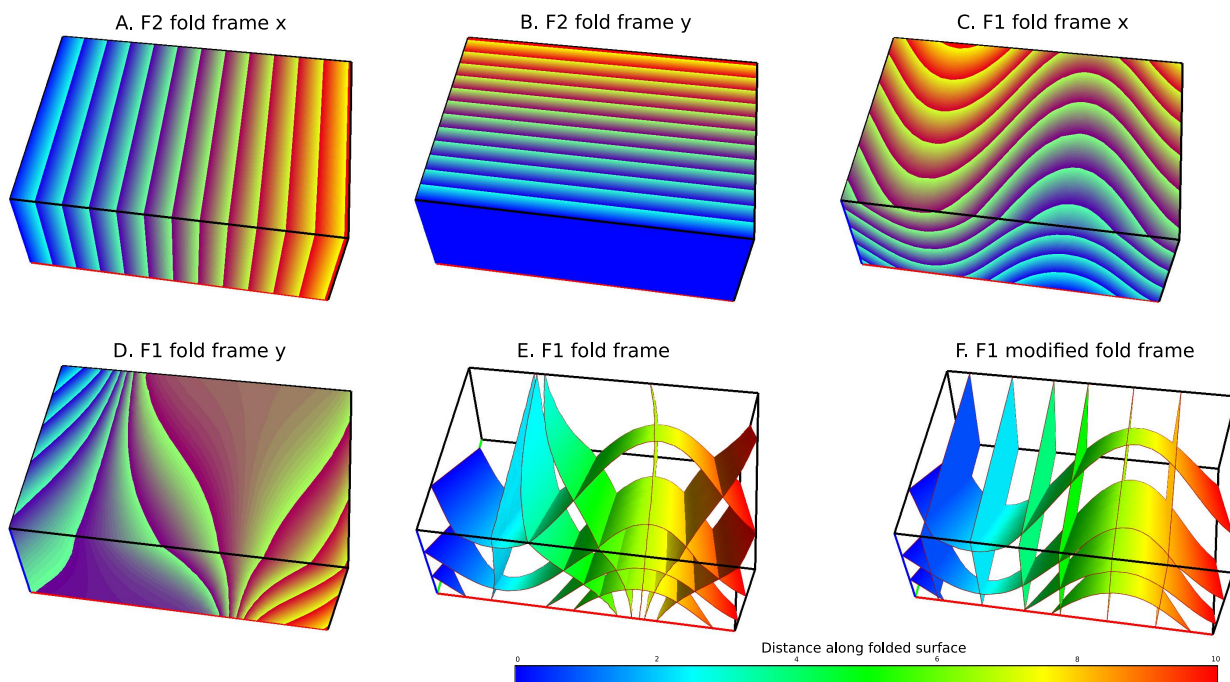


Figure 6.2: Scalar fields representing two consecutive fold frames. A: z coordinate for D2. B: y coordinate for D2. C: z coordinate for D1 interpolated using fold interpolator. D: y coordinate for D1 interpolated so that $e_z \cdot e_y = 0$. E: Isosurfaces of interpolated y coordinate and x coordinate coloured with the distance along the folded surface. F: y coordinate represented using z coordinate for D2.

This problem can be addressed by considering the dip isogons for similar folds. The dip isogons represent the location of two folded surfaces with the same dip, which is equivalent to measuring the same distance along the surface prior to folding. For similar folds, the dip isogons are parallel and correspond to lines of equal α_L values (Laurent et al., 2016, chapter 2). This means that for similar folds, the z coordinate of the younger fold frame (e.g. F_2) can be used for the y coordinate of the F_1 fold frame. This can be seen in Fig. 6.2F where the isosurfaces of F_2 z coordinate are used instead of the interpolated y coordinate. However, the direction of the gradient of y , e_y , is not orthogonal to e_z . The direction of e_y can be determined using the geometrical relationship between the fold axis of the younger folding event L_2 and the normal to the folded foliation S_1 . The fold axis direction, e_y can be calculated by finding the vector product of L_2 and e_z where e_z is the direction of the current fold frame z coordinate. This approach is more geometrically robust than the method presented in Laurent et al. (2016, chapter 2) and also reduces the number of scalar fields that are needed to be interpolated for each model iteration.

6.2.4 Towards joint geological and geophysical inversions

Building multiple realisations of geological models has been a common approach for integrating geological uncertainty and ambiguity into inverse problems and has been addressed by multiple authors (e.g. Cherpeau et al., 2012; de la Varga and Wellmann, 2016; Guillen et al., 2008; Jessell et al., 2014, 2010; Lindsay et al., 2014; Wellmann and Regenauer-Lieb, 2012; Wellmann et al., 2010). Inverse methods are used to reduce uncertainty using potential field observations (magnetics and gravity) or reservoir production data (e.g. Cherpeau and Caumon, 2015; Cherpeau et al., 2012; Guillen et al., 2008; Irving et al., 2014; Jessell et al., 2014, 2010; Lindsay et al., 2014; Suzuki et al., 2008; Wellmann and Regenauer-Lieb, 2012; Wellmann et al., 2010). In general, these approaches have generated model suits of geologically possible models by perturbing the geological observations and then generating a series of geological models from each perturbed dataset (Jessell et al., 2010; Lindsay et al., 2012; Wellmann and Regenauer-Lieb, 2012; Wellmann et al., 2010), or by perturbing a description of the geological features that are being modeled for example Cherpeau et al. (2012) uses a stochastic description of faults to model fault networks.

These approaches have either defined the parameters of the inverse problems as the input data for the geological models or from a finite sample of already calculated models. The model/parameter space is then sampled and can be optimised for the observed potential field or reservoir inversions. While this approach has proven to be functional, it is not a true inversion of geology. The geological observations should be combined with the geophysical observations using both geological and geophysical misfit functions as suggested by Jessell et al. (2010). Geological observations as with any observation in inverse problems should not be used to generate models but should be used to falsify them (Tarantola, 2005, 2006). We have presented a way where geological observations and geological knowledge can be incorporated directly into the geological inversion scheme. This will mean that a joint inversion between potential fields and geology could be performed allowing for the geophysical and geological model space to be better sampled. In a large dimensional space, it may result in fairly significant differences in the inversion results, especially when the geological data is ambiguous. In theory, the addition of more information to the geological inversion scheme will have a similar result as incorporating geological knowledge into the geological inversion (Grose et al., 2018, chapter 5). Where geological knowledge is included in the geological inversion the posterior model space is more constrained and closer to the reference model.

6.2.5 Incorporating faults

The next challenge is to incorporate faults into the modeling and inversion process. There already exists a number of methods for incorporating faults into implicit schemes. Calcagno et al. (2008) provide a coherent method for incorporating faults into the implicit schemes where the main variables considered when modeling faults are: (1) fault geometry, (2) fault border and; (3) fault influence.

Their approach uses the same workflow for modeling all geological surfaces where the geometry of the fault surface is interpolated using a combination of orientation and location information. The topological relationship between faults can be incorporated into the model and determines the interaction between faults and stratigraphic contacts. The model area is subdivided into fault blocks and the interpolation of stratigraphic horizons is performed within these fault blocks. The faults effectively introduce local discontinuities into the interpolation of the stratigraphic horizons allowing for sharp changes in the scalar field inline with the geometry of the fault.

The offset of the fault is not explicitly taken into account when interpolating the fault geometries and is defined implicitly by the locations of the stratigraphic horizons near the fault. The offset of faults can be incorporated into the modeling process using geologically motivated likelihood functions if the location of contacts is stochastically perturbed (de la Varga and Wellmann, 2016). Laurent et al. (2013) also introduced curvilinear coordinate system for defining geometrical attributes of the fault geometry. The fault frame has three coordinates g_0 , g_1 and g_2 that define the geometry of the fault, displacement direction and the lateral evolution of the displacement.

The existing methods for characterising fault geometries are widely applicable to brittle deformation. It would be possible to incorporate these within the modeling scheme I have proposed by first building a fault network and then running the fold inversion. This also could be incorporated with a stochastic fault network as proposed by Cherpeau and Caumon (2015). Another approach for stochastically building a fault network uses a prior conceptual structural model to condition the simulation (Aydin and Caers, 2017). These approaches could be incorporated into the fold modeling and inversion presented in this study where the faulting post dates the folding.

However, most of these approaches are all limited by the fundamental assumption that all faults that are to be modeled are observed. In reality, this is similar to the problem of modeling folds where the existing methodologies were applicable when the fold geometry was well described by the data. It would make sense to use a similar statistical/geostatistical analysis of structural observations in order to better characterise the geometry of the faults. This could for example be using the fault frame coordinates (Laurent et al., 2013) in a similar way to how the fold frame has been used in this study. It is also important that the profiles describing the fault geometry can be derived from structural observations.

Another limitation of these methods is how faults interact with the surrounding stratigraphic horizons. Laurent et al. (2013) incorporated some information about the fault displacement by incorporating more of the kinematic observations/knowledge into the structural modeling. A similar approach is needed to be able to characterise the geometry of shear zones. Ideally, a similar parameterised description of faults can be derived where the structural geology observations of faults including movement direction and fault displacement can be then used to invert structural observations associated with faults.

The interaction between faults and folds will also need to be investigated as the order of deformation can have a significant impact on the topological relationship between stratigraphic units and geological structures (Thiele et al., 2016a,b). Faults are often associated with folding either forming coevally or over-

printing existing folds. Each of these scenarios presents a unique challenge both in deriving a method for properly accounting for these geometries in implicit schemes but also in deriving an appropriate geostatistical measure for identifying and characterising them. Preliminary work has shown a promising application of the S-Plot in identifying faulting overprinting existing folds.

6.2.6 Inversion of polydeformed terranes

The fold modeling framework presented is applicable to multiple generations of folding (Laurent et al., 2016, chapter 2). In both Grose et al. (2017b, chapter 4) and Grose et al. (2018, chapter 5) we have only presented an approach that uses a single fold frame and only inverts the fold axis and fold limb rotation angle for a single event. We have shown that the joint inversion of these two geometrical properties is needed to characterise the fold geometry as the calculated fold limb rotation angle depends on the orientation of the fold axis. Similarly, for multiple generations of folding the geometry of the younger folds will impact the calculated fold rotation angle for the older folding events, because orientation of the fold frame direction vectors will change for each realisation. Theoretically, the full geological inversion of multiple phases of deformation can be easily incorporated into the inversion scheme by adding additional likelihood functions for each additional folding event. However, the reason I have not presented any examples is that there are a number of technical challenges that need to be addressed prior to performing a complete geological inversion.

When the fold frame is not constant, the scalar fields representing the z and y coordinates needs to be interpolated for each iteration of the MCMC sampler. This not only significantly increases the likelihood computation time but also adds a major challenge in storing/accessing the computed scalar fields efficiently. An additional problem is that for each additional folding event the number of parameters to sample will increase. This will generally mean that more iterations of the sampling algorithm are needed for the sampler to converge on a representative sample of the posterior distribution. This combined with the increased time to calculated the likelihood functions will significantly increase the computational requirements.

There are a number of possible areas for improving the time taken to perform the sampling: the first involves the computation of the scalar field which scales with the number of elements in the mesh. Optimizing the number of elements needed in the mesh, as well as the shape and size of elements could be a suitable direction for reducing the computational requirements. The orientation of the tetrahedron elements can significantly impact the resulting interpolation quality (Laurent, 2016). If the orientation of the mesh can be refined prior to interpolation it is possible this could reduce the computational time due to reducing the number of iterations or the number of tetrahedron needed. Improving meshing techniques (*e.g.* for Finite Element Analysis and other numerical simulations) is an ongoing field of research. However, in these cases the complexities are often associated with geometrical and topological issues associated with the object that is being meshed. The problem for implicit structural modeling, will be somewhat easier to define as the object being meshed (the model volume) is geometrically simple and the mesh does not need to exactly represent the geometries. The main challenges are in determining the areas where the interpolated surface will be most complex and predicting the approximate orientation of the interpolated surface.

The fold constraints provide a good approximation of the orientation of the folded surface prior to interpolation. Rebuilding the mesh for each interpolation will most likely not provide any speed improvements as this is also a computationally intensive task. However, it may be possible to incorporate some mesh refinements into the iterative process of the interpolation algorithm. Another approach would be to

use a polynomial trend interpolation approach such as radial basis function or co-kriging. Polynomial approaches have the potential for significant speed increases due to the performance of parallel computing to solve dense matrix algebra. However, these approaches typically scale poorly with the number of constraints. This would mean that the fold constraints could not be used throughout the model volume (as is possible with DSI) and would need to be applied only in the locations where they are necessary.

Another approach for speeding up the inversion scheme is to improve the efficiency of the sampling algorithm. In this study, the Metropolis-Hastings (MH) algorithm was used to sample from the posterior distribution. The Metropolis-Hastings algorithm approximates the posterior distribution iteratively using a random walk (Hoffman and Gelman, 2014). More sophisticated sampling methods may provide a potential for reducing the number of likelihood functions that need to be calculated. There are more efficient samplers based on the Hamiltonian Monte Carlo (HMC) algorithm. These samplers reduce the number of iterations required by using first-order gradient information for the posterior. Unfortunately, as the posterior distribution becomes more complex it may not be possible to provide gradient information of the posterior. The posterior distribution for the inversion involving the interpolation of multiple fold frame coordinates is unlikely to have an analytical solution to the gradient. It is possible to use these improved sampling methods for the inversion parameters that gradient information can be defined. However, both MH and HMC based algorithms are performed iteratively and cannot be run in parallel. Another approach for sampling is to use an ensemble of samplers with affine invariance, this approach provides improvements to the standard Metropolis Hastings algorithm (Goodman and Weare, 2010). It is possible to run an ensemble sampler in parallel meaning that the likelihood function could be calculated for different parameter values at the same time, reducing the overall computational time. A parallel ensemble sampler *emcee*¹ (Foreman-Mackey et al., 2013) exists that means that the time consuming calculation of the likelihood function (involving computing scalar fields) can be computed in parallel for the number of walkers that are used. Preliminary work testing this sampler for the examples in Grose et al. (2017b, 2018, chapters 4 and 5) show promising potential for improving performance.

A combination of improving the interpolation of the scalar fields using either improved meshing or a meshless approach and a more sophisticated sampler provide interesting avenues for improving the performance of these methods. These changes to the sampling will require a purpose built interpolation algorithm that is not restricted by licensing and using standard data formats will be necessary.

¹emcee <http://dfm.io/emcee/current/>

6.3 Conclusion

Understanding and characterising the distribution of rock packages and geological features subsurface and in 3D is one of the greatest challenges facing geological research and resource exploration. There has previously been a significant difference between the data and knowledge on a geological map and the input to 3D models. This study has used the concepts from structural geology to help constrain the geometry of folded surface for implicit modeling. This reduces the need for additional interpretive constraints to be included by the geologist to be able to model geologically reasonable geometries. The main contributions of this study are:

- **Structural modeling:** A theoretical and numerical framework for modeling superimposed folding events. A series of constraints for discrete implicit modeling schemes dedicated to fold geometry modeling.
- **Statistical analysis of structural data:** Fold geostatistics (S-Plot and S-Variogram) are new tools for characterising the geometry of folds from field structural observations. Fold geometry can be represented by two 1D plots where a data driven approach for characterising fold geometry using a Fourier series to provide geologically reasonable extrapolation for sparse data.
- **Geological inversion:** A framework for geological inversion using Bayesian inference where geological observations are used to falsify models. Analysis of inversion variability and posterior distribution for model parameters can be used to provide target locations for structural data. Model variability from geological inversion is associated with structural complexity and can be used to target where additional structural data is required.
- **Geological knowledge:** A quantitative approach for incorporating geological knowledge into the geological inversion scheme. The incorporation of geological knowledge into the geological inversion significantly reduces the overall model variability and provides a very useful application of methods to real case studies.

This study has shown that significant improvements can be made to 3D modeling methods by incorporating the methods and approaches used in structural geology. Improvements in structural modeling (Grose et al., 2017a,b; Hillier et al., 2014; Laurent et al., 2016), geophysical inversions (Giraud et al., 2017) and geostatistical analysis of structural datasets (Grose et al., 2017a; Hillier et al., 2013) will form a toolkit for a new age of structural geology.

Bibliography

- G. I. Alsop and R. E. Holdsworth. Vergence and facing patterns in large-scale sheath folds. *Journal of Structural Geology*, 21(10): 1335–1349, 1999. ISSN 01918141. doi: 10.1016/S0191-8141(99)00099-1.
- R. J. Armit, P. G. Betts, B. F. Schaefer, and L. Ailleres. Constraints on long-lived Mesoproterozoic and Palaeozoic deformational events and crustal architecture in the northern Mount Painter Province, Australia. *Gondwana Research*, 22(1): 207–226, 2012. ISSN 1342937X. doi: 10.1016/j.gr.2011.11.003.
- R. J. Armit, L. Ailleres, P. G. Betts, B. F. Schaefer, and T. N. Blaikie. High-heat geodynamic setting during the Palaeozoic evolution of the Mount Painter Province, SA, Australia: Evidence from combined field structural geology and potential-field inversions. *Geophysical Journal International*, 199(1): 253–275, 2014. ISSN 1365246X. doi: 10.1093/gji/ggu263.
- G. B. Arpat and J. Caers. Conditional simulation with patterns. *Mathematical Geology*, 39(2): 177–203, 2007. ISSN 08828121. doi: 10.1007/s11004-006-9075-3.
- C. Aug, J.-P. Chilès, G. Courrioux, and C. Lajaunie. 3D Geological Modelling and Uncertainty: The Potential-field Method. In *Geostatistics Banff 2004*, vol. 31, p. 145–154. Springer Netherlands, 2005. ISBN 978-1-4020-3515-9. doi: 10.1007/978-1-4020-3610-1_15.
- O. Aydin and J. K. Caers. Quantifying structural uncertainty on fault networks using a marked point process within a Bayesian framework. *Tectonophysics*, 712-713: 101–124, 2017. ISSN 00401951. doi: 10.1016/j.tecto.2017.04.027.
- G. Bárdossy and J. Fodor. Traditional and new ways to handle uncertainty in geology. *Natural Resources Research*, 10(3), 2001.
- I. Basson, P. Creus, C. Anthonissen, B. Stoch, and J. Ekkerd. Structural analysis and implicit 3D modelling of high-grade host rocks to the Venetia kimberlite diatremes, Central Zone, Limpopo Belt, South Africa. *Journal of Structural Geology*, 86: 47–61, 2016. ISSN 01918141. doi: 10.1016/j.jsg.2016.03.002.
- F. Bastida, J. Aller, N. C. Bobillo-Ares, and N. C. Toimil. Fold geometry: A basis for their kinematical analysis. *Earth-Science Reviews*, 70: 129–164, 2005. ISSN 00128252. doi: 10.1016/j.earscirev.2004.11.006.
- A. Bell. Vergence: an evaluation. *Journal of Structural Geology*, 3(3): 197–202, 1981. ISSN 01918141. doi: 10.1016/0191-8141(81)90015-8.
- S. Bigi, A. Conti, P. Casero, L. Ruggiero, R. Recanati, and L. Lipparini. Geological model of the central Periadriatic basin (Apennines, Italy). *Marine and Petroleum Geology*, 42: 107–121, 2013. ISSN 02648172. doi: 10.1016/j.marpetgeo.2012.07.005.

BIBLIOGRAPHY

- T. Blaikie, L. Ailleres, P. G. Betts, and R. A. Cas. Interpreting subsurface volcanic structures using geologically constrained 3-D gravity inversions: Examples of maar-diatremes, Newer Volcanics Province, southeastern Australia. *Journal of Geophysical Research: Solid Earth*, 119(4): 3857–3878, 2014. doi: 10.1002/2013JB010751.
- D. Blake and R. Page. The Proterozoic Davenport province, central Australia: regional geology and geochronology. *Precambrian Research*, 40-41: 329–340, 1988. ISSN 03019268. doi: 10.1016/0301-9268(88)90074-5.
- T. Bodin, M. Sambridge, N. Rawlinson, and P. Arroucau. Transdimensional tomography with unknown data noise. *Geophysical Journal International*, 189(3): 1536–1556, 2012a. ISSN 0956540X. doi: 10.1111/j.1365-246X.2012.05414.x.
- T. Bodin, M. Sambridge, H. Tkalčić, P. Arroucau, K. Gallagher, and N. Rawlinson. Transdimensional inversion of receiver functions and surface wave dispersion. *Journal of Geophysical Research: Solid Earth*, 117(2): 1–25, 2012b. ISSN 21699356. doi: 10.1029/2011JB008560.
- C. E. Bond. Uncertainty in structural interpretation: Lessons to be learnt. *Journal of Structural Geology*, 74: 185–200, 2015. ISSN 01918141. doi: 10.1016/j.jsg.2015.03.003.
- C. E. Bond, A. D. Gibbs, Z. K. Shipton, and S. Jones. What do you think this is? "Conceptual uncertainty" In geoscience interpretation. *GSA Today*, 17(11): 4–10, 2007a. ISSN 10525173. doi: 10.1130/GSAT01711A.1.
- C. E. Bond, Z. K. Shipton, R. R. Jones, R. W. H. Butler, and A. D. Gibbs. Knowledge transfer in a digital world: Field data acquisition, uncertainty, Visualization, and data management. *Geosphere*, 3: 568–576, 2007b. ISSN 1553-040 (ISSN).
- C. E. Bond, C. Philo, and Z. K. Shipton. When there isn't a right answer: Interpretation and reasoning, key skills for twenty-first century geoscience. *International Journal of Science Education*, 33(5): 629–652, 2011. ISSN 09500693. doi: 10.1080/09500691003660364.
- C. E. Bond, G. Johnson, and J. F. Ellis. Structural model creation: the impact of data type and creative space on geological reasoning and interpretation. *Geological Society, London, Special Publications*, 421 (1): 83–97, 2015. ISSN 0305-8719. doi: 10.1144/SP421.4.
- M. D. Buhmann and J. Levesley. Radial Basis Functions: Theory and Implementations. *Mathematics of Computation*, 73(247): 1578–1581, 2004. ISSN 1941-6016. doi: 10.1017/CBO9780511543241.
- J. Burg and C. J. L. Wilson. A kinematic analysis of the southernmost part of the Bega Batholith. *Australian Journal of Earth Sciences*, 35(1): 1–13, 1988. ISSN 0812-0099. doi: 10.1080/08120098808729435.
- P. Calcagno, J. Chilès, G. Courrioux, and A. Guillen. Geological modelling from field data and geological knowledge. *Physics of the Earth and Planetary Interiors*, 171(1-4): 147–157, 2008. ISSN 00319201. doi: 10.1016/j.pepi.2008.06.013.
- T. Carmichael and L. Ailleres. Method and analysis for the upscaling of structural data. *Journal of Structural Geology*, 83: 121–133, 2016. ISSN 01918141. doi: 10.1016/j.jsg.2015.09.002.

- A. Cauchy. Méthode générale pour la résolution des systemes d'équations simultanées. *Comp. Rend. Sci. Paris*, (2): 2–4, 1847.
- G. Caumon. Towards Stochastic Time-Varying Geological Modeling. *Mathematical Geosciences*, 42(5): 555–569, 2010. ISSN 1874-8961. doi: 10.1007/s11004-010-9280-y.
- G. Caumon, C. H. Sword Jr., and J.-L. Mallet. Constrained modifications of non-manifold B-reps. In *Proceedings of the Symposium on Solid Modeling and Applications*, p. 310–315, 2003.
- G. Caumon, P. Collon-Drouaillet, C. Le Carlier de Veslud, S. Viseur, and J. Sausse. Surface-Based 3D Modeling of Geological Structures. *Mathematical Geosciences*, 41(8): 927–945, 2009. ISSN 1874-8961. doi: 10.1007/s11004-009-9244-2.
- G. Caumon, G. Gray, C. Antoine, and M.-O. Titeux. Three-Dimensional Implicit Stratigraphic Model Building From Remote Sensing Data on Tetrahedral Meshes: Theory and Application to a Regional Model of La Popa Basin, NE Mexico. *IEEE Transactions on Geoscience and Remote Sensing*, 51(3): 1613–1621, 2013. ISSN 0196-2892. doi: 10.1109/TGRS.2012.2207727.
- N. Cherpeau and G. Caumon. Stochastic structural modelling in sparse data situations. *Petroleum Geoscience*, 21(4): 233–247, 2015. ISSN 1354-0793. doi: 10.1144/petgeo2013-030.
- N. Cherpeau, G. Caumon, and B. Lévy. Stochastic simulations of fault networks in 3D structural modeling. *Comptes Rendus Geoscience*, 342(9): 687–694, 2010a. ISSN 16310713. doi: 10.1016/j.crte.2010.04.008.
- N. Cherpeau, G. Caumon, and B. Lévy. Stochastic simulation of fault networks from 2D seismic lines. In *SEG Technical Program Expanded Abstracts 2010*, p. 2366–2370, 2010b. doi: 10.1190/1.3513325.
- N. Cherpeau, G. Caumon, J. Caers, and B. Lévy. Method for Stochastic Inverse Modeling of Fault Geometry and Connectivity Using Flow Data. *Mathematical Geosciences*, 44(2): 147–168, 2012. ISSN 1874-8961. doi: 10.1007/s11004-012-9389-2.
- J. P. Chilès and P. Delfiner. *Geostatistics: Modeling Spatial Uncertainty*. 1999.
- J.-P. Chilès and P. Delfiner. Conditional Simulations. *Geostatistics*, p. 449–592, 2008. doi: 10.1002/9780470316993.ch7.
- J. P. Chilès, C. Aug, A. Guillen, T. Lees, J. P. Chiles, C. Aug, A. Guillen, and T. Lees. Modelling the Geometry of Geological Units and its Uncertainty in 3D From Structural Data : The Potential-Field Method. *Spectrum Series - Australasian Institute of Mining and Metallurgy*, 14(November): 22–24, 2004. ISSN 1-920806-41-5.
- P. Collon, W. Steckiewicz-Laurent, J. Pellerin, G. Laurent, G. Caumon, G. Reichart, and L. Vaute. 3D geomodelling combining implicit surfaces and Voronoi-based remeshing: A case study in the Lorraine Coal Basin (France). *Computers and Geosciences*, 77: 29–43, 2015. ISSN 00983004. doi: 10.1016/j.cageo.2015.01.009.
- P. Collon, A. Pichat, C. Kergaravat, A. Botella, G. Caumon, J.-C. Ringenbach, and J.-P. Callot. 3D modeling from outcrop data in a salt tectonic context: Example from the Inceyol minibasin, Sivas Basin, Turkey. *Interpretation*, 4(3): SM17–SM31, 2016. ISSN 2324-8858. doi: 10.1190/INT-2015-0178.1.

BIBLIOGRAPHY

- E. Cowan, R. Beatson, H. Ross, W. Fright, T. McLennan, T. Evans, J. Carr, R. Lane, D. Bright, A. Gillman, P. Oshust, and M. Titley. Practical implicit geological modelling. *5th International Mining Geology Conference*, (8): 89–99, 2003. ISSN 01489062.
- L. A. Cox. Artfactual Uncertainty in Risk Analysis. *Risk Analysis*, 2: 121–135, 1982. ISSN 1539-6924.
- S. Cox, V. Wall, M. Etheridge, and T. Potter. Deformational and metamorphic processes in the formation of mesothermal vein-hosted gold deposits — examples from the Lachlan Fold Belt in central Victoria, Australia. *Ore Geology Reviews*, 6(5): 391–423, 1991. ISSN 01691368. doi: 10.1016/0169-1368(91)90038-9.
- E. A. de Kemp. Visualization of complex geological structures using 3-D Bézier construction tools. *Computers & Geosciences*, 25(5): 581–597, 1999. ISSN 00983004. doi: 10.1016/S0098-3004(98)00159-9.
- E. a. de Kemp. 3-D visualization of structural field data: examples from the Archean Caopatina Formation, Abitibi greenstone belt, Québec, Canada. *Computers & Geosciences*, 26(5): 509–530, 2000. ISSN 00983004. doi: 10.1016/S0098-3004(99)00142-9.
- M. de la Varga and J. F. Wellmann. Structural geologic modeling as an inference problem: A Bayesian perspective. *Interpretation*, 4(3): 1–16, 2016. ISSN 2324-8858. doi: 10.1190/INT-2015-0188.1.
- B. Efron and R. Tibshirani. *An introduction to the bootstrap*. New York : Chapman & Hall, 1993. ISBN 0412042312.
- O. Fernandez, S. Jones, N. Armstrong, G. Johnson, A. Ravaglia, and J. A. Muñoz. Automated tools within workflows for 3D structural construction from surface and subsurface data. *GeoInformatica*, 13(3): 291–304, 2009. ISSN 1384-6175. doi: 10.1007/s10707-008-0059-y.
- M. Fleuty. The description of folds. *Proceedings of the Geologists' Association*, 75(4): 461–492, 1964. ISSN 00167878. doi: 10.1016/S0016-7878(64)80023-7.
- C. Forbes, P. Betts, and G. Lister. Synchronous development of Type 2 and Type 3 fold interference patterns: evidence for recumbent sheath folds in the Allendale Area, Broken Hill, NSW, Australia. *Journal of Structural Geology*, 26(1): 113–126, 2004. ISSN 01918141. doi: 10.1016/S0191-8141(03)00074-9.
- C. J. Forbes and P. G. Betts. Development of Type 2 fold interference patterns in the Broken Hill Block: implications for strain partitioning across a detachment during the Olarian Orogeny. *Australian Journal of Earth Sciences*, 51(2): 173–188, 2004. ISSN 0812-0099. doi: 10.1111/j.1440-0952.2004.01051.x.
- D. Foreman-Mackey, D. W. Hogg, D. Lang, and J. Goodman. emcee: The MCMC Hammer. *Publications of the Astronomical Society of the Pacific*, 125(925): 306, 2013.
- T. Frank, A.-L. Tertois, and J.-L. Mallet. 3D-reconstruction of complex geological interfaces from irregularly distributed and noisy point data. *Computers & Geosciences*, 33(7): 932–943, 2007. ISSN 00983004. doi: 10.1016/j.cageo.2006.11.014.
- R. Frodeman. Geological reasoning: Geology as an interpretive and historical science. *Geological Society of America Bulletin*, 107(8): 960–0968, 1995. ISSN 00167606. doi: 10.1130/0016-7606(1995)107<0960:GRGAAI>2.3.CO;2.

- P. Fullagar, G. Pears, D. Hutton, and A. Thompson. 3D gravity and aeromagnetic inversion for MVT lead-zinc exploration at Pillara, Western Australia. *Exploration Geophysics*, 35(2): 142, 2004. ISSN 0812-3985. doi: 10.1071/EG04142.
- J. Giraud, E. Pakyuz-Charrier, M. Jessell, M. Lindsay, R. Martin, and V. Ogarko. Uncertainty reduction through geologically conditioned petrophysical constraints in joint inversion. *Geophysics*, 82(6): ID19–ID34, 2017. ISSN 0016-8033. doi: 10.1190/geo2016-0615.1.
- J. Goodman and J. Weare. Ensemble samplers with affine invariance. *Comm. app math and comp sci*, 5(2), 2010.
- B. Grasemann, G. Wiesmayr, E. Draganits, and F. Fuisseis. Classification of Refold Structures. *The Journal of Geology*, 112(1): 119–125, 2004. ISSN 0022-1376. doi: 10.1086/379696.
- L. Grose, G. Laurent, L. Aillères, R. Armit, M. Jessell, and G. Caumon. Structural data constraints for implicit modeling of folds. *Journal of Structural Geology*, 104: 80–92, 2017a. ISSN 01918141. doi: 10.1016/j.jsg.2017.09.013.
- L. Grose, G. Laurent, L. Aillères, R. Armit, M. Jessell, and T. Cousin-Dechenaud. Inversion of structural geology data for fold geometry. *submitted to Journal of Geophysical Research: Solid Earth*, p. 1–19, 2017b.
- L. Grose, L. Aillères, G. Laurent, and R. Armit. Inversion of geological data and knowledge. *in prep.*, 2018.
- A. Guillen, P. Calcagno, G. Courrioux, A. Joly, and P. Ledru. Geological modelling from field data and geological knowledge. *Physics of the Earth and Planetary Interiors*, 171(1-4): 158–169, 2008. ISSN 00319201. doi: 10.1016/j.pepi.2008.06.014.
- F. Guillocheau, D. Rouby, C. Robin, C. Helm, N. Rolland, C. Le Carlier de Veslud, and J. Braun. Quantification and causes of the terrigenous sediment budget at the scale of a continental margin: a new method applied to the Namibia-South Africa margin. *Basin Research*, 24(1): 3–30, 2012. ISSN 0950091X. doi: 10.1111/j.1365-2117.2011.00511.x.
- C. Gumiaux, D. Gapais, and J. Brun. Geostatistics applied to best-fit interpolation of orientation data. *Tectonophysics*, 376(3-4): 241–259, 2003. ISSN 00401951. doi: 10.1016/j.tecto.2003.08.008.
- C. Hilgers. Christoph Hilgers Scotland Schottland field trip page, 2006.
- M. Hillier, E. de Kemp, and E. Schetselaar. 3D form line construction by structural field interpolation (SFI) of geologic strike and dip observations. *Journal of Structural Geology*, 51: 167–179, 2013. ISSN 01918141. doi: 10.1016/j.jsg.2013.01.012.
- M. J. Hillier, E. M. Schetselaar, E. A. de Kemp, and G. Perron. Three-Dimensional Modelling of Geological Surfaces Using Generalized Interpolation with Radial Basis Functions. *Mathematical Geosciences*, 46 (8): 931–953, 2014. ISSN 1874-8961. doi: 10.1007/s11004-014-9540-3.
- Ø. Hjelle, S. a. Petersen, and A. M. Bruaset. A Numerical Framework for Modeling Folds in Structural Geology. *Mathematical Geosciences*, 45(3): 255–276, 2013. ISSN 1874-8961. doi: 10.1007/s11004-013-9452-7.

BIBLIOGRAPHY

- M. Hoffman and A. Gelman. The No-U-Turn Sampler: Adaptively Setting Path Lengths in Hamiltonian Monte Carlo. *Journal of Machine Learning Research*, 15: 30, 2014. ISSN 15337928.
- M. Honarkhah and J. Caers. Stochastic Simulation of Patterns Using Distance-Based Pattern Modeling. *Mathematical Geosciences*, 42(5): 487–517, 2010. ISSN 1874-8961. doi: 10.1007/s11004-010-9276-7.
- P. Hudleston. Fold morphology and some geometrical implications of theories of fold development. *Tectonophysics*, 16(1-2): 1–46, 1973. ISSN 00401951. doi: 10.1016/0040-1951(73)90129-7.
- P. J. Hudleston and S. H. Treagus. Information from folds: A review. *Journal of Structural Geology*, 32(12): 2042–2071, 2010. ISSN 01918141. doi: 10.1016/j.jsg.2010.08.011.
- A. D. Irving, D. Kuznetsov, E. Robert, T. Manzocchi, and C. Childs. Optimization of Uncertain Structural Parameters With Production and Observation Well Data. *SPE Reservoir Evaluation & Engineering*, 17(04): 547–558, 2014. ISSN 1094-6470. doi: 10.2118/171558-PA.
- M. Jessell, L. Aillères, E. D. Kemp, M. Lindsay, F. Wellmann, M. Hillier, G. Laurent, T. Carmichael, and R. Martin. Next generation 3D geological modelling and inversion. In *Society of Economic Geologists Special Publication 18*, chapter 13, p. 261–272. 2014.
- M. W. Jessell. Noddy: an interactive map creation package. *Unpublished MSc Thesis, University of London*, 1981.
- M. W. Jessell and R. K. Valenta. Structural geophysics: Integrated structural and geophysical modelling. *Computer Methods in the Geosciences*, 15: 303–324, 1996. doi: 10.1016/S1874-561X(96)80027-7.
- M. W. Jessell, L. Ailleres, and E. A. de Kemp. Towards an integrated inversion of geoscientific data: What price of geology? *Tectonophysics*, 490(3-4): 294–306, 2010. ISSN 00401951. doi: 10.1016/j.tecto.2010.05.020.
- R. R. Jones, K. J. W. McCaffrey, R. W. Wilson, and R. E. Holdsworth. Digital field data acquisition: towards increased quantification of uncertainty during geological mapping. *Geological Society, London, Special Publications*, 239(1): 43–56, 2004. ISSN 0305-8719. doi: 10.1144/GSL.SP.2004.239.01.04.
- J. M. Kolb and V. Lekić. Receiver function deconvolution using transdimensional hierarchical bayesian inference. *Geophysical Journal International*, 197(3): 1719–1735, 2014. ISSN 1365246X. doi: 10.1093/gji/ggu079.
- C. Lajaunie, G. Courrioux, and L. Manuel. Foliation fields and 3D cartography in geology: Principles of a method based on potential interpolation. *Mathematical Geology*, 29(4): 571–584, 1997. ISSN 0882-8121. doi: 10.1007/BF02775087.
- G. Laurent. Iterative Thickness Regularization of Stratigraphic Layers in Discrete Implicit Modeling. *Mathematical Geosciences*, 48(7): 811–833, 2016. ISSN 18748953. doi: 10.1007/s11004-016-9637-y.
- G. Laurent, G. Caumon, A. Bouziat, and M. Jessell. A parametric method to model 3D displacements around faults with volumetric vector fields. *Tectonophysics*, 590: 83–93, 2013. ISSN 00401951. doi: 10.1016/j.tecto.2013.01.015.

- G. Laurent, L. Ailleres, L. Grose, G. Caumon, M. Jessell, and R. Armit. Implicit modeling of folds and overprinting deformation. *Earth and Planetary Science Letters*, 456: 26–38, 2016. ISSN 0012821X. doi: 10.1016/j.epsl.2016.09.040.
- L. Li, A. Boucher, and J. Caers. SGEMS-UQ: An uncertainty quantification toolkit for SGEMS. *Computers & Geosciences*, 62: 12–24, 2014. ISSN 00983004. doi: 10.1016/j.cageo.2013.09.009.
- M. Lindsay, M. Jessell, L. Ailleres, S. Perrouty, E. de Kemp, and P. Betts. Geodiversity: Exploration of 3D geological model space. *Tectonophysics*, 594: 27–37, 2013a. ISSN 00401951. doi: 10.1016/j.tecto.2013.03.013.
- M. D. Lindsay, L. Aillères, M. W. Jessell, E. A. de Kemp, and P. G. Betts. Locating and quantifying geological uncertainty in three-dimensional models: Analysis of the Gippsland Basin, southeastern Australia. *Tectonophysics*, 546-547: 10–27, 2012. ISSN 00401951. doi: 10.1016/j.tecto.2012.04.007.
- M. D. Lindsay, S. Perrouty, M. W. Jessell, and L. Ailleres. Making the link between geological and geophysical uncertainty: geodiversity in the Ashanti Greenstone Belt. *Geophysical Journal International*, 195(2): 903–922, 2013b. ISSN 0956-540X. doi: 10.1093/gji/ggt311.
- M. D. Lindsay, P. G. Betts, and L. Ailleres. Data fusion and porphyry copper prospectivity models, southeastern Arizona. *Ore Geology Reviews*, 61: 120–140, 2014. ISSN 01691368. doi: 10.1016/j.oregeorev.2014.02.001.
- R. J. Lisle. Uniformly Dipping Beds. In *Geological Structures and Maps*, p. 2–28. Elsevier, 2003. ISBN 978-0-7506-5780-8. doi: 10.1016/B978-075065780-8/50003-3.
- R. J. Lisle and N. C. Toimil. Defining folds on three-dimensional surfaces. *Geology*, 35(6): 519–522, 2007. ISSN 00917613. doi: 10.1130/G23207A.1.
- A. Malinverno and R. L. Parker. Two ways to quantify uncertainty in geophysical inverse problems. *Geophysics*, 71(3): W15–W27, 2006. ISSN 0016-8033. doi: 10.1190/1.2194516.
- J.-L. Mallet. Discrete smooth interpolation in geometric modelling. *Computer-Aided Design*, 24(4): 178–191, 1992. ISSN 00104485. doi: 10.1016/0010-4485(92)90054-E.
- J.-l. Mallet. *Geomodeling*. Oxford University Press, New York, NY, USA, 2002. ISBN 0195144600.
- J. L. Mallet. Space-time mathematical framework for sedimentary geology. *Mathematical Geology*, 36(1): 1–32, 2004. ISSN 08828121. doi: 10.1023/B:MATG.0000016228.75495.7c.
- J.-L. Mallet. Elements of Mathematical Sedimentary Geology: the GeoChron Model. p. 1–4, 2014. doi: 10.3997/9789073834811.
- J. C. Mann. Uncertainty in Geology. In *Computers in geology– 25 years of progress*, p. 241–254. Oxford University Press, New York, NY, USA, 1993.
- C. Massiot and G. Caumon. Accounting for axial directions, cleavages and folding style during 3D structural modeling. In *30th Gocad Meeting Proceedings*, 2010.

BIBLIOGRAPHY

- M. Maxelon, P. Renard, G. Courrioux, M. Brändli, and N. Mancktelow. A workflow to facilitate three-dimensional geometrical modelling of complex poly-deformed geological units. *Computers & Geosciences*, 35(3): 644–658, 2009. ISSN 00983004. doi: 10.1016/j.cageo.2008.06.005.
- M. A. McLean, T. J. Rawling, P. G. Betts, G. Phillips, and C. J. Wilson. Three-dimensional inversion modelling of a Neoproterozoic basin in the southern Prince Charles Mountains, East Antarctica. *Tectonophysics*, 456(3-4): 180–193, 2008. ISSN 00401951. doi: 10.1016/j.tecto.2008.04.023.
- I. Moretti. Working in complex areas: New restoration workflow based on quality control, 2D and 3D restorations. *Marine and Petroleum Geology*, 25(3): 205–218, 2008. ISSN 02648172. doi: 10.1016/j.marpetgeo.2007.07.001.
- K. Mosegaard and A. Tarantola. Monte Carlo sampling of solutions to inverse problems. *Journal of Geophysical Research*, 100(B7): 12431–12447, 1995. ISSN 0148-0227. doi: 10.1029/94JB03097.
- R. Moyen, J.-L. Mallet, T. Frank, B. Leflon, and J.-J. Royer. 3D-Parameterization of the 3D geological space - The GeoChron model. *Proc. European Conference on the Mathematics of Oil Recovery (ECMOR IX)*, (September): 8, 2004.
- A. G. Mueller, L. B. Harris, and A. Lungan. Structural control of greenstone-hosted Gold mineralization by transcurrent shearing: A new interpretation of the Kalgoorlie mining district, Western Australia. *Ore Geology Reviews*, 3(4): 359–387, 1988. ISSN 01691368. doi: 10.1016/0169-1368(88)90027-3.
- J. Muir and H. Tkalčić. A method of spherical harmonic analysis in the geosciences via hierarchical Bayesian inference. *Geophysical Journal International*, 203(2): 1164–1171, 2015. ISSN 0956-540X. doi: 10.1093/gji/ggv361.
- I. Mynatt, S. Bergbauer, and D. D. Pollard. Using differential geometry to describe 3-D folds. *Journal of Structural Geology*, 29(7): 1256–1266, 2007. ISSN 01918141. doi: 10.1016/j.jsg.2007.02.006.
- M. G. O’dea, P. G. Betts, T. MacCready, and L. Aillères. Sequential development of a mid-crustal fold-thrust complex: evidence from the Mitakoodi Culmination in the eastern Mt Isa Inlier, Australia. *Australian Journal of Earth Sciences*, 53(March 2015): 69–90, 2006. ISSN 0812-0099. doi: 10.1080/08120090500432447.
- D. S. Oliver and Y. Chen. Recent progress on reservoir history matching: A review. *Computational Geosciences*, 15(1): 185–221, 2011. ISSN 14200597. doi: 10.1007/s10596-010-9194-2.
- A. Patil, D. Huard, and C. J. Fonnesbeck. PyMC: Bayesian Stochastic Modelling in Python. *Journal of statistical software*, 35(4): 1–81, 2010. ISSN 1548-7660. doi: 10.18637/jss.v035.i04.
- M. Perrin, P. H. Oltra, and S. Coquillart. Progress in the study and modelling of similar fold interferences. *Journal of Structural Geology*, 10(6): 593–605, 1988. ISSN 01918141. doi: 10.1016/0191-8141(88)90026-0.
- M. Putz, K. Stüwe, M. Jessell, and P. Calcagno. Three-dimensional model and late stage warping of the Plattengneis Shear Zone in the Eastern Alps. *Tectonophysics*, 412(1-2): 87–103, 2006. ISSN 00401951. doi: 10.1016/j.tecto.2005.10.003.

- J. G. Ramsay. Interference Patterns Produced by the Superposition of Folds of Similar Type. *The Journal of Geology*, 70(4): 466–481, 1962a. ISSN 0022-1376. doi: 10.1086/626837.
- J. G. Ramsay. The Geometry and Mechanics of Formation of “Similar” Type Folds. *The Journal of Geology*, 70(3): 309–327, 1962b.
- J. G. Ramsay and M. I. Huber. *The techniques of modern structural geology, Volume 2: Folds and fractures*. London ; New York: Academic Press, 1987. ISBN 0125769229.
- J. C. Refsgaard, J. P. van der Sluijs, J. Brown, and P. van der Keur. A framework for dealing with uncertainty due to model structure error. *Advances in Water Resources*, 29(11): 1586–1597, 2006. ISSN 03091708. doi: 10.1016/j.advwatres.2005.11.013.
- N. M. S. N. M. S. Rock and N. M. S. Rock. *Numerical geology : a source guide, glossary, and selective bibliography to geological uses of computers and statistics*. Lecture notes in earth sciences ; 18. Springer-Verlag, Berlin ; New York, 1988. ISBN 0387500707.
- P. Røe, F. Georgsen, and P. Abrahamsen. An Uncertainty Model for Fault Shape and Location. *Mathematical Geosciences*, 46(8): 957–969, 2014. ISSN 18748953. doi: 10.1007/s11004-014-9536-z.
- M. J. S. Rudwick. The Emergence of a Visual Language for Geological Science 1760—1840. *History of Science*, 14(3): 149–195, 1976. doi: 10.1177/007327537601400301.
- J. H. Shaw, A. Plesch, C. Tape, M. P. Suess, T. H. Jordan, G. Ely, E. Hauksson, J. Tromp, T. Tanimoto, R. Graves, K. Olsen, C. Nicholson, P. J. Maechling, C. Rivero, P. Lovely, C. M. Brankman, and J. Munster. Unified Structural Representation of the southern California crust and upper mantle. *Earth and Planetary Science Letters*, 415: 1–15, 2015. ISSN 0012821X. doi: 10.1016/j.epsl.2015.01.016.
- D. S. Sivia. *Data analysis : a Bayesian tutorial*. Oxford : Clarendon Press, Oxford : New York, 1996. ISBN 0198518897.
- C. L. Stabler. Simplified Fourier analysis of fold shapes. *Tectonophysics*, 6(4): 343–350, 1968. ISSN 00401951. doi: 10.1016/0040-1951(68)90049-8.
- C. W. Stowe. Application of Fourier analysis for computer representation of fold profiles. *Tectonophysics*, 156(3-4): 303–311, 1988. ISSN 00401951. doi: 10.1016/0040-1951(88)90067-4.
- S. Strebelle. Conditional Simulation of Complex Geological Structures Using Multiple-Point Statistics. *Mathematical Geology*, 34(1): 1–21, 2002. ISSN 0882-8121, 1573-8868. doi: 10.1023/A:1014009426274.
- S. Suzuki, G. Caumon, and J. Caers. Dynamic data integration for structural modeling: model screening approach using a distance-based model parameterization. *Computational Geosciences*, 12(1): 105–119, 2008. ISSN 1420-0597. doi: 10.1007/s10596-007-9063-9.
- L. Tacher, I. Pomian-Srzednicki, and A. Parriaux. Geological uncertainties associated with 3-D subsurface models. *Computers & Geosciences*, 32(2): 212–221, 2006. ISSN 00983004. doi: 10.1016/j.cageo.2005.06.010.

BIBLIOGRAPHY

- A. Tarantola. *Inverse Problem Theory and Methods for Model Parameter Estimation*, vol. 120. 2005. ISBN 978-0-89871-572-9. doi: 10.1137/1.9780898717921.
- A. Tarantola. Popper, Bayes and the inverse problem. *Nature Physics*, 2(8): 492–494, 2006. ISSN 1745-2473. doi: 10.1038/nphys375.
- B. Thibert, J. P. Gratier, and J. M. Morvan. A direct method for modeling and unfolding developable surfaces and its application to the Ventura Basin (California). *Journal of Structural Geology*, 27(2): 303–316, 2005. ISSN 01918141. doi: 10.1016/j.jsg.2004.08.011.
- S. T. Thiele, M. W. Jessell, M. Lindsay, V. Ogarko, J. F. Wellmann, and E. Pakyuz-Charrier. The topology of geology 1: Topological analysis. *Journal of Structural Geology*, 91: 27–38, 2016a. ISSN 01918141. doi: 10.1016/j.jsg.2016.08.009.
- S. T. Thiele, M. W. Jessell, M. Lindsay, J. F. Wellmann, and E. Pakyuz-Charrier. The topology of geology 2: Topological uncertainty. *Journal of Structural Geology*, 91: 74–87, 2016b. ISSN 01918141. doi: 10.1016/j.jsg.2016.08.010.
- R. L. Thiessen and W. D. Means. Classification of fold interference patterns: a reexamination. *Journal of Structural Geology*, 2(3): 311–316, 1980. ISSN 01918141. doi: 10.1016/0191-8141(80)90019-X.
- P. Thore, A. Shtuka, M. Lecour, T. Ait-Ettajer, and R. Cognot. Structural uncertainties: Determination, management, and applications. *Geophysics*, 67(3): 840–852, 2002. ISSN 0016-8033. doi: 10.1190/1.1484528.
- Z. Tian, J. Sun, B. F. Windley, Z. Zhang, Z. Gong, X. Lin, and W. Xiao. Cenozoic detachment folding in the southern Tianshan foreland, NW China: Shortening distances and rates. *Journal of Structural Geology*, 84: 142–161, 2016. ISSN 01918141. doi: 10.1016/j.jsg.2016.01.007.
- C. Torrence and G. P. Compo. A Practical Guide to Wavelet Analysis. *Bulletin of the American Meteorological Society*, 79(1): 61–78, 1998. ISSN 00030007. doi: 10.1175/1520-0477(1998)079<0061:APGTWA>2.0.CO;2.
- T. Torvela and C. E. Bond. Do experts use idealised structural models? Insights from a deepwater fold-thrust belt. *Journal of Structural Geology*, 33(1): 51–58, 2011. ISSN 0191-8141. doi: 10.1016/j.jsg.2010.10.002.
- S. H. Treagus. A theory of finite strain variation through contrasting layers, and its bearing on cleavage refraction. *Journal of Structural Geology*, 5(3-4): 351–368, 1983. ISSN 01918141. doi: 10.1016/0191-8141(83)90023-8.
- J. VanderPlas. Frequentism and Bayesianism: A Python-driven Primer. *ArXiv e-prints*, 2014.
- S. A. Vollgger, A. R. Cruden, L. Ailleres, and E. J. Cowan. Regional dome evolution and its control on ore-grade distribution: Insights from 3D implicit modelling of the Navachab gold deposit, Namibia. *Ore Geology Reviews*, 69: 268–284, 2015. ISSN 01691368. doi: 10.1016/j.oregeorev.2015.02.020.
- J. F. Wellmann and K. Regenauer-Lieb. Uncertainties have a meaning: Information entropy as a quality measure for 3-D geological models. *Tectonophysics*, 526-529: 207–216, 2012. ISSN 00401951. doi: 10.1016/j.tecto.2011.05.001.

- J. F. Wellmann, F. G. Horowitz, E. Schill, and K. Regenauer-Lieb. Towards incorporating uncertainty of structural data in 3D geological inversion. *Tectonophysics*, 490(3-4): 141–151, 2010. ISSN 00401951. doi: 10.1016/j.tecto.2010.04.022.
- J. F. Wellmann, S. T. Thiele, M. D. Lindsay, M. W. Jessell, and J. Abc. pynoddy 1.0 : an experimental platform for automated 3-D kinematic and potential field modelling. *Geoscientific Model Development*, p. 1019–1035, 2016. doi: 10.5194/gmd-9-1019-2016.
- J. F. Wellmann, M. D. E. L. A. Varga, R. E. Murdie, K. Gessner, M. Jessell, M. de la Varga, R. E. Murdie, K. Gessner, and M. Jessell. Uncertainty estimation for a geological model of the Sandstone greenstone belt, Western Australia {\textendash} insights from integrated geological and geophysical inversion in a Bayesian inference framework. *Geological Society, London, Special Publications*, 453, 2017. ISSN 0305-8719. doi: 10.1144/SP453.12.
- C. Wijns, F. Boschetti, and L. Moresi. Inverse modelling in geology by interactive evolutionary computation. *Journal of Structural Geology*, 25(10): 1615–1621, 2003. ISSN 0191-8141. doi: [https://doi.org/10.1016/S0191-8141\(03\)00010-5](https://doi.org/10.1016/S0191-8141(03)00010-5).
- G. D. Williams and T. J. Chapman. The geometrical classification of noncylindrical folds. *Journal of Structural Geology*, 1(3): 181–185, 1979. ISSN 01918141. doi: 10.1016/0191-8141(79)90038-5.
- D. a. Zimmerman, G. de Marsily, C. a. Gotway, M. G. Marietta, C. L. Axness, R. L. Beauheim, R. L. Bras, J. Carrera, G. Dagan, P. B. Davies, D. P. Gallegos, a. Galli, J. Gómez-Hernández, P. Grindrod, a. L. Gutjahr, P. K. Kitanidis, a. M. Lavenue, D. McLaughlin, S. P. Neuman, B. S. RamaRao, C. Ravenne, and Y. Rubin. A comparison of seven geostatistically based inverse approaches to estimate transmissivities for modeling advective transport by groundwater flow. *Water Resources Research*, 34(6): 1373–1413, 1998. ISSN 0043-1397. doi: 10.1029/98WR00003.

Appendix A

Discrete linear tetrahedral support

The proposed modeling is implemented in the framework of discrete implicit modeling (Frank et al., 2007), where an interpolated scalar field φ is mathematically represented by a piece-wise linear field based on a tetrahedron mesh. In this mesh, φ is linearly interpolated from the four nodal values of each tetrahedral element.

We considering a tetrahedron, whose corners are indexed from 0 to 3, with corner positions denoted $(\bar{x}_i, \bar{y}_i, \bar{z}_i)$ and nodal values are stored in the φ_c vector. The scalar field is expressed as a linear function of \bar{x}, \bar{y} , and \bar{z} :

$$\varphi(\bar{x}, \bar{y}, \bar{z}) = [1, \bar{x}, \bar{y}, \bar{z}] \cdot [a_0, a_1, a_2, a_3]^t \quad (\text{A.1})$$

After Frank et al. (2007), the coefficient a_i are solution of the following equation:

$$\begin{bmatrix} 1 & \bar{x}_0 & \bar{y}_0 & \bar{z}_0 \\ 1 & \bar{x}_1 & \bar{y}_1 & \bar{z}_1 \\ 1 & \bar{x}_2 & \bar{y}_2 & \bar{z}_2 \\ 1 & \bar{x}_3 & \bar{y}_3 & \bar{z}_3 \end{bmatrix} \cdot \begin{bmatrix} a_0 \\ a_1 \\ a_2 \\ a_3 \end{bmatrix} = \begin{bmatrix} \varphi_{c0} \\ \varphi_{c1} \\ \varphi_{c2} \\ \varphi_{c3} \end{bmatrix} \quad (\text{A.2})$$

This system can be solved for non-degenerated tetrahedron by inverting the left matrix, which defines the \mathbf{M} matrix for Section 2.4.1 and the linear interpolation:

$$\mathbf{M} = \begin{bmatrix} 1 & \bar{x}_0 & \bar{y}_0 & \bar{z}_0 \\ 1 & \bar{x}_1 & \bar{y}_1 & \bar{z}_1 \\ 1 & \bar{x}_2 & \bar{y}_2 & \bar{z}_2 \\ 1 & \bar{x}_3 & \bar{y}_3 & \bar{z}_3 \end{bmatrix}^{-1} \quad (\text{A.3})$$

$$\varphi(\bar{x}, \bar{y}, \bar{z}) = [1, \bar{x}, \bar{y}, \bar{z}] \cdot \mathbf{M} \cdot \varphi_c \quad (\text{A.4})$$

Based on Frank et al. (2007), a linear relation can also be written to define the constant gradient of a scalar field inside a given tetrahedron. This matrix referred to as \mathbf{T} in this paper is defined as:

$$\mathbf{T} = \begin{bmatrix} (\bar{x}_1 - \bar{x}_0) & (\bar{y}_1 - \bar{y}_0) & (\bar{z}_1 - \bar{z}_0) \\ (\bar{x}_2 - \bar{x}_0) & (\bar{y}_2 - \bar{y}_0) & (\bar{z}_2 - \bar{z}_0) \\ (\bar{x}_3 - \bar{x}_0) & (\bar{y}_3 - \bar{y}_0) & (\bar{z}_3 - \bar{z}_0) \end{bmatrix}^{-1} \cdot \begin{bmatrix} -1 & 1 & 0 & 0 \\ -1 & 0 & 1 & 0 \\ -1 & 0 & 0 & 1 \end{bmatrix} \quad (\text{A.5})$$

Appendix B

Digital Appendix

The digital appendix for this thesis has subfolders containing the following items.

B.1 3D model supplementary data

Case studies from all chapters are included in the digital appendix as gocad 2009 files. The associated python scripts for running the geological inversions have been included.

B.2 1D synthetic examples

iPython notebooks containing the 1D inversion code are also included with the relevant python files.

B.3 StructuralFactory gocad plugin

The StructuralFactory plugin has been written for Gocad 2009.3 running on 64 bit Linux. It depends on SolidExplorer, IsoSurf, Gopy and StructuralLab plugins from the Research in Intergrated Numerical Geology (RING) team that can be downloaded for members of the RING-GOCAD consortium.

B.4 PyFactory python interface to StructuralFactory

Python library for interfacing StructuralFactory making use of the Gocad python interface provided by RING's gopy plugin. Dependencies:

- numpy
- matplotlib
- scipy
- pymc
- emcee

This library can be installed as a standard python library. It requires 64bit python which can be compiled using the GoPy source code.